THE UNIVERSITY OF HULL

Structure and Interactions of Colloidal Particles at Fluid Interfaces

being a Thesis submitted for the degree of *Doctor of Philosophy* in
the University of Hull

by

Adam Daniel Law, B.Sc.(Hons.)
Department of Physics

April 2011

Declaration

Except where explicitly stated, this thesis is the result of my own work. No part of my thesis has already been or is being concurrently submitted for any degree, diploma or qualification at any other university. This work presented in this thesis has produced the following papers:

1. A. D. Law and D. M. A. Buzza, *'Determination of Interaction Potentials of Colloidal Monolayers from the Inversion of Pair Correlation Ffunctions: A Two-Dimensional Predictor-Corrector Method.'*, Journal of Chemical Physics, **131**, 094704 (2009); doi:10.1063/1.3216568

2. A. D. Law and D. M. A. Buzza, *'Obtaining Effective Pair Potentials in Colloidal Monolayers Using a Thermodynamically Consistent Inversion Scheme.'*, Langmuir, **26**, 7107 (2010), doi:10.1021/la9037233

3. A. D. Law, D. M. A. Buzza and T. S. Horozov, *'Two-Dimension Colloidal Alloys.'*, Physical Review Letters, **106**, 128302 (2011), doi:10.1103/PhysRevLett.106.128302

4. A. D. Law, D. M. A. Buzza and T. S. Horozov, *'The Structure and Melting Transition of Two-Dimensional Colloidal Alloys.'*, Soft Matter, (2011), *submitted.*

In addition to the publications listed above, the work of this thesis has also been the source for the following conference presentations, both oral and posters:

Invited talks:

1. Max-Planck-Institut für Intelligente Systeme, Stuttgart, Germany, January 2011.
2. CCP5 ‘Particle Adsorption on Soft Interfaces’, Warwick University, Warwick, UK, July 2010.

Contributed talks:

3. ‘Macro 2010’ 43rd IUPAC World Polymer Congress, Scottish Exhibition and Conference Centre, Glasgow, UK, July 2010.
4. 13th IACIS International Conference on Surface & Colloid Science, Columbia University, New York, USA, June 2009.

Poster presentations:

5. Gordon Research Conference on Polyelectrolyte, Macromolecular and Colloidal Solutions, Ventura, California, USA, February 2010
6. UK Polymer Colloids Forum, The University of Hull, Kingston Upon Hull, UK, September 2009.
7. ‘Physics by the Lake’ Theoretical Physics Summer School, Ambleside, UK, July 2009.
8. IOP ‘Biological & Soft Matter’, Warwick University, Warwick, UK, April 2009.
9. ‘Surfaces & Interfaces’ CCP5 Annual Meeting, London School of Economics, London, UK, September 2008.

This thesis contains approximately 32526 words, 45 figures and 4 tables.

Adam D. Law
12^{th} April 2011

Acknowledgements

Foremost, I would like to express my gratitude to Dr. Martin Buzza for his excellent supervision and encouragement throughout.

Additionally, I am thankful to the Department of Physics and the *Surfactant and Colloid Group* at the University of Hull. I am also grateful for the guidance and help from the following people: Dr. Tommy Horozov, Professor Bernard Binks, Professor Paul Fletcher, Dr. Pietro Cicuta (Cambridge University) and Dr. Stefan Bon (Warwick University).

Finally I would like to thank my friends and family, in particular my Dad, Mum and brother Tom for their support.

Adam D. Law
12th April 2011

‘Science is a way of trying not to fool yourself. The first principle is that you must not fool yourself, and you are the easiest person to fool.’

Richard P. Feynman

Abstract

The structure and stability of colloidal monolayers depends crucially on the effective pair interaction potential between colloidal particles. In the first part of the thesis, we present two novel methods for extracting the pair potential from the two-dimensional radial distribution function of dense colloidal monolayers. The first is a so-called Predictor-Corrector routine that replaces the conventionally unknown Bridge function, with an iteratively obtained hard-disk bridge function. The second method is based on the Ornstein-Zernike relation and the HMSA closure that contains a single fitting parameter which is determined by requiring thermodynamic consistency between the virial and compressibility equations of state. The accuracy of these schemes are tested against Monte Carlo simulation data from monolayers interacting via a wide range of commonly encountered pair potentials. We also test the stability of these methods with respect to noise levels and truncation of the source data to mimic experimentally obtained structural data. Finally we apply these inversion schemes to experimental pair correlation function data obtained for charged polystyrene particles adsorbed at an oil/water interface. We find that the pair interaction potential is purely repulsive at low densities, but an attractive component develops at higher densities. The origin of this attractive component at higher densities is at present unknown.

In the second part of this thesis, we study how the colloid interactions studied above influence the structure of the colloidal monolayer. Specifically inspired by recent experimental results on mixed monolayers of large and small very hydrophobic silica particles at an octane/water interface, we study theoretically the structure of two-dimensional binary mixtures of colloidal particles interacting via a dipole-dipole potential. We find that at zero temperature, a rich variety of binary crystal structures are obtained whose structure depends on the dipole moment ratio and the number fraction of small particles. At experimentally relevant finite temperatures, we find that the AB_2 and AB_6 binary super-lattice structures are thermodynamically stable while other binary structures *e.g.* AB_5, which are stable at zero temperature, are thermodynamically unstable at finite temperature. Specifically, the melting temperature of the AB_5 system is found to be three orders of magnitude lower than that of the AB_2 and AB_6 systems and at experimentally relevant temperatures, melts into a semi-disordered phase with local AB_6 order.

Contents

Chapter 1

Colloids at fluid interfaces

1.1 Introduction

The designation *'colloid'* is used for particles that can be soft or solid and are of some small dimension, ranging from nanometres to tens of micrometres and are dispersed in a liquid or gas [1, 2]. The last three decades has witnessed a gradual increase in interest into the investigation of colloids because they are abundant in everyday experience. From mayonnaise to blood and from ink to smoke, these particle dispersions are labelled under the banner of *'soft matter'*, a term that encompasses physical states that are easily deformed by thermal stresses or fluctuations and occur at an energy scale comparable with room temperature thermal energy.

The focus of this Thesis is on colloids at an interfacial boundary between two fluids where colloids exhibit a number of interesting features not found in the bulk. For example, at the interface between two immiscible liquids, colloids appear to accumulate. This can be explained by considering the free energy required to

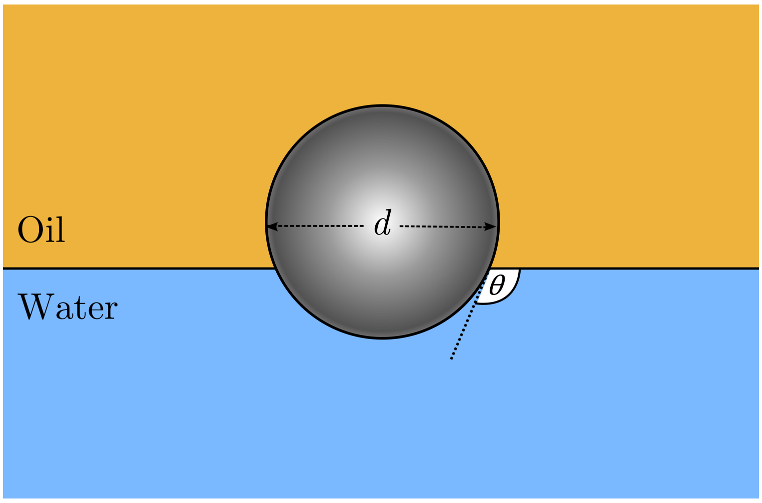

Figure 1.1: Schematic of a single colloid particle of diameter d, adsorbed to an oil/water interface with a contact angle θ measured through the aqueous sub-phase.

detach a colloidal particle from the interface in the absence of line tension effects, which reads as [1, 3]

$$\Delta G_d = \pi \frac{d^2}{4} \gamma_I (1 - |\cos\theta|)^2, \tag{1.1}$$

where d is the particle diameter, γ_I is the surface tension of the interface and θ is the particle contact angle. Here θ is the angle formed between the tangents to the solid surface and the liquid-liquid interface measured through one of the liquids at each point of the three phase contact line where the solid and the liquid-liquid interface meet [1]; this geometry is shown clearly in figure 1.1 with the contact angle θ being measured through the water. We can see from eqn.(1.1) that the energy required to detach a spherical particle from the interface rapidly increases with particle size and that for most contact angles, the detachment energies are much greater than the available thermal energy k_BT (where k_B is Boltzmann's constant and T is the absolute temperature), approaching a maximum at $\theta = 90°$

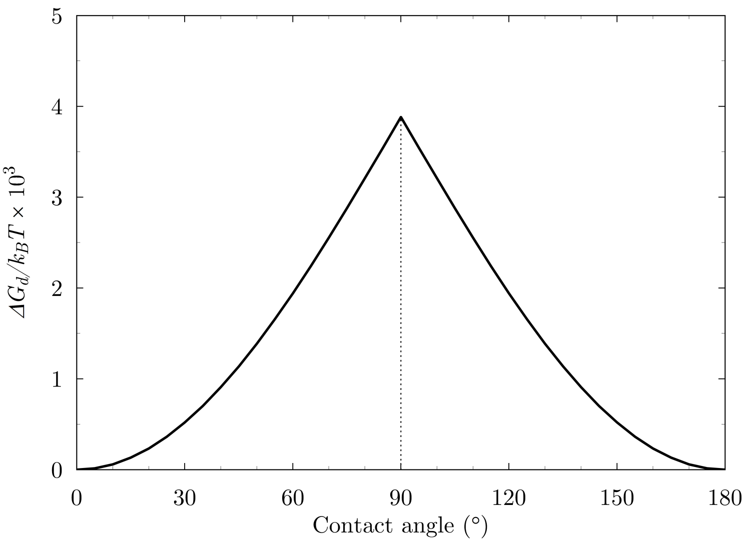

Figure 1.2: Free energy of detachment of a spherical particle from an oil/water interface, calculated using eqn.(1.1) with $d = 20\text{nm}$ and $\gamma_I = 50\text{mN}\cdot\text{m}^{-1}$ as a function of particle contact angle.

(see figure 1.2), *i.e.* when the particle is equally immersed in both phases at the interface. The energy of particle attachment to the interface, defined through the relationship $\Delta G_a = -\Delta G_d$ is therefore negative for *all* contact values, hence making particle attachment thermodynamically favourable so that the particle is consequently deemed as being *surface active* [1]. This fact was realised through experimentation by the founding pioneers of colloid science Ramsden [4] and Pickering [5], at the beginning of the 20^{th} century. It can be seen that the high stability of particles at the interface has proven to be very important industrially. Specifically, a major focus for the application of colloids at interfaces are particle stabilised emulsions and foams. The use of solid particles alone to stabilise mixtures of oil and water in the form of emulsions is credited to Pickering [5], and the phrase *'Pickering emulsions'* has been used for many years because of this. Applications of this type of emulsion range from food and cosmetics to the petroleum and agrochemical industries.

From the scientific point of view, the irreversible trapping of particles at fluid interfaces effectively creates a *two-dimensional* system and because the structural properties of condensed matter heavily rely of the spatial dimensions of the system, one can expect these model systems to exhibit new phenomena that do not generally occur in bulk systems. In this context, colloidal systems have considerable experimental advantages in comparison to their atomic counterparts. In atomic systems, the interactions between the particles are determined by their electronic structure and therefore cannot be influenced externally. As we will see in later chapters, the situation for colloidal systems is different: A change in the quality of the solvent, in the temperature, in the salt concentration or in the chemistry of the particle surface can bring about dramatic changes in the effective interactions between the particles. In addition to these, the size of the micrometre sized colloidal particles, which are of the same order of magnitude as the wavelength of visible light, opens up the possibility of performing light scattering experiments to probe the static and dynamical behaviour of colloidal systems, a technique which is much cheaper to perform than the traditional neutron scattering approaches. For example, phase transitions in colloidal suspensions can be studied in real time using optical techniques, and are analogous to phase transitions in liquids [6]. These attractive features render colloidal particles at interfaces as ideal model systems to study soft matter physics in two-dimensions.

1.2 Aim of this thesis

When considering particles trapped at a fluid interface, one encounters the obvious step change in dielectric constants between the two media and interfacial effects that will qualitatively change the standard interaction seen for bulk systems. For example, the Deraguin-Landau-Verwey-Overbeek (DLVO) theory which successfully describes particle interactions between charged colloids in the bulk cannot suitably describe the particle interactions at interfaces. In spite of these complications, significant theoretical advancements have been made in the interaction potentials between colloids at interfaces (this is reviewed in chapter 2). However, these theories need to be verified through experiments and consequently, the forces between the particles adsorbed at interfaces need to be measured accurately. If one can measure these forces accurately, theories can be proved or disproved, and the processes that underpin structural ordering in these systems can be used in an attempt to develop new materials. To this end, the aims of this thesis are firstly, to construct accurate theoretical methods for extracting the interactions that occur between particles at fluid interfaces from experimentally measured structural information such as the pair correlation function of the monolayer and secondly, to investigate theoretically the influence of these interactions on the structure of colloidal monolayers.

1.3 Outline of Thesis

The rest of this Thesis is structured as follows: In **chapter 2** we review previous theoretical and experimental studies of the effective interactions of colloids at interfaces. Specifically we consider the different mechanisms that contribute to the interaction forces in these systems, and the relevant experimental and theoretical methods used to extract information regarding these interactions. In particular, we will introduce the idea of determining interactions through the use of the so-called *Integral Equation Theory*.

Chapter 3 will explain in detail how one can use Integral Equation Theory to extract pair interaction data for colloidal monolayers. Specifically, we will explain how one characterises an isotropic fluid and how the structure is closely linked to the interactions between colloids. Therefore, we will use classical fluid theory to introduce a range of *pair correlation functions* that will heavily feature in various *inversion methods*, *i.e.* methods that utilise the pair correlation function describing the structure to extract the interaction potential between colloids. Conventional inversion methods, including one-step inversion methods and thermodynamically consistent inversion methods will be introduced in this section. Finally in this chapter we will describe the Monte Carlo simulation technique which is heavily used in this Thesis.

Chapter 4 will focus on two thermodynamically consistent inversion schemes for two-dimensional systems that we have developed, namely a *Hard-Disk Predictor-Corrector* (HDPC) method and a Hypernetted-Chain and soft-core Mean Spherical Approximation *HMSA closure* inversion scheme. The aim of developing these schemes is to improve the accuracy of determining the interaction between the colloids compared to the conventional one-step inversion schemes.

In **chapter** 5, we test the accuracy of our two inversion schemes against Monte Carlo simulation data for known input potentials and compare this with conventional one-step inversion schemes. Having benchmarked our new inversion schemes, we then apply them in **chapter 6** to experimentally measured pair correlation function data obtained from our collaborators.

Chapter 7 will focus on how the interactions between colloids at interfaces influence the structure of the monolayer: Specifically, we investigate *binary colloidal monolayers* interacting via a dipole-dipole potential. We will show that experimentally observed two-dimensional colloidal super-lattices containing two sizes of colloid can be reproduced through both theory and simulation. We also use computer simulations to show that some of the binary crystal arrangements obtained at zero temperature which should be accessible in the experimental system, are in fact thermodynamically unstable at experimentally relevant, finite temperatures. Finally we investigate, through Monte Carlo simulations, the melting transition of these colloidal alloys and the metastability of these systems during crystallisation. We therefore demonstrate that the phase behaviour of two-dimensional binary colloidal crystals is even richer than hitherto anticipated.

Chapter 2

Interactions between colloids at interfaces

2.1 Interaction potentials between colloids at fluid interfaces

Liquids and dense colloidal fluids are distinguished from dilute gases by the importance of short-range correlations, and from crystalline substances by the distinct lack of long-range order. The most simple liquid systems are monodisperse liquids consisting of spherically shaped particles. The structure of these liquids is strongly controlled by the forces that occur between the particles in the medium in question. Instead of a force, it is often mathematically convenient to describe the interactions by what is known as the *pair interaction potential* between spherical particles, which from now onwards will be denoted by $u(r)$. The relationship between the force, F and the (spherically symmetric) potential function, u for spherical molecules a distance r apart is given by [7]

$$F = -\frac{du}{dr}. \tag{2.1}$$

The potential $u(r)$ can be predominantly attractive or repulsive, or both, depending on the nature of the system and plays an essential role in describing phenomena, such as aggregation processes and structural ordering.

Specialising from here on the colloidal system, interactions between charged colloidal particles in bulk systems are largely explained by what is known as the Derjaguin-Landau-Verwey-Overbeek (DLVO) theory [7]. However when particles are situated at an interface, the pair potentials are much more complicated, primarily due to the step change in the dielectric constant between the different phases and interfacial effects. In spite of this, important theoretical advances have been made in describing the interaction between colloids at interfaces; these will be introduced in the next section.

Although there are a number of studies in the literature on more exotically shaped particles adsorbed at interfaces, such as ellipsoidal and rod-like particles, in this Thesis we will only consider spherical particles of diameter d, irreversibly attached to the interface through adsorption between two bulk media of dielectric constants ε_1 and ε_2 respectively, forming an effectively two-dimensional (2D) system. This geometry is illustrated by figure 2.1 and will form the basis of all models considered in this work. We also note that the systems of interest are generally charged, hence in what follows, our focus will be on the case of charged colloids.

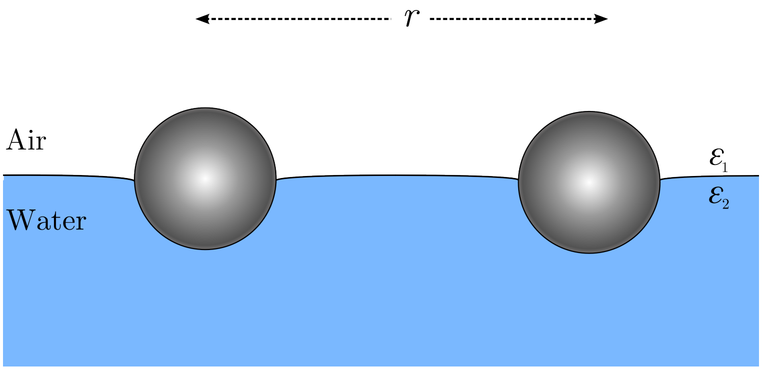

Figure 2.1: Side view of two homogeneous colloidal particles at an air/water interface separated by an interparticle distance r. The particles illustrated here are equally immersed by both phases of dielectric constant ε_1 and ε_2.

2.1.1 Electrostatic interactions

Colloidal suspensions in the bulk are generally stabilised in aqueous solutions by surface charges. These charges are realised by chemically decorating the colloid surface with dissociable groups which can easily release ions upon contact with water. It is the interaction between the surface charges and the counterions in the polar phase that creates the *electrostatic interaction*, which for most bulk systems is accurately described by DLVO theory [2]. The electrostatic interaction provides a repulsive barrier strong enough to sufficiently prevent coagulation in many soft matter systems. The electrostatic interaction is strongly modified by counterions bound to the surface of the particles, creating the so-called *'Stern layer'*. Surrounding this layer is a diffuse region of counterions that are less firmly associated but still largely cancel out the surface charge of the particle. This region is called the *'Gouy-Chapman layer'* and it strongly screens the bare coulombic charge repulsion between the charged colloids, therefore reducing its

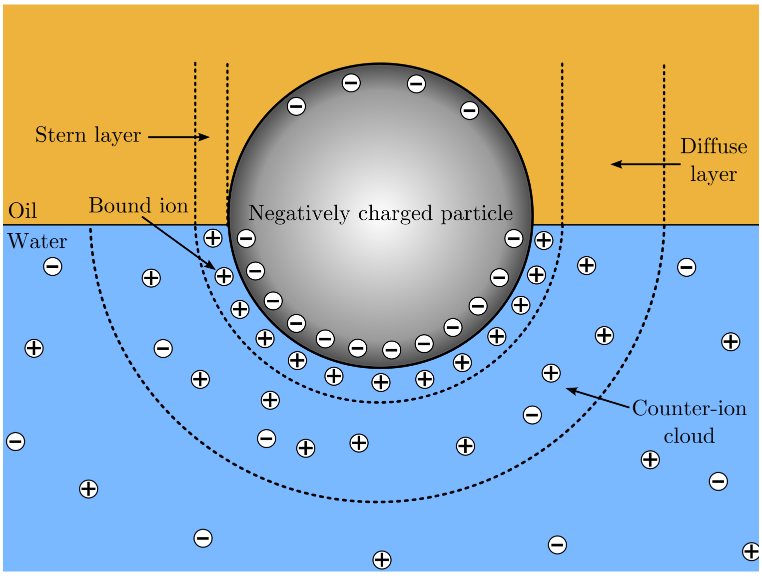

Figure 2.2: Side view of a single colloid trapped at the interface between water and a non-polar medium. The charge on the water side is assumed to be homogeneous and the majority of the counter-ions in the polar phase are trapped in a layer close to the colloid surface, known as the *'Stern layer'*. The outer layer is a diffuse region known as the *'Gouy-Chapman layer'*.

range. This effect as a whole is commonly referred to as *'electric double layers'* [7]. At interfaces between water and a non-polar fluid, the water side of the particle remains highly charged, whereas the colloid surface in contact with the non-polar fluid is energetically favoured to re-neutralise the surface groups, creating an *asymmetric* double layer. Figure 2.2 illustrates the asymmetric double layer effect described here for a homogeneous particle located at the interface between a polar and non-polar medium.

Historically it was Pieranski [8] who conducted the first seminal study of the interaction of colloid particles at fluid interfaces by simply considering charged polystyrene particle assembly at a water/vapour interface. He reported electrostatic repulsions between particles, with a much longer range than electrostatic repulsions seen in the bulk. He suggested that these effects are due to the colloid surface being covered with dissociable groups, which releases ions when brought into contact with the water creating highly charged colloid-water surfaces. The surface charge will generally have a balanced number of counterions. This results in an effective *dipole* between the colloid surface charge and the counterions in the solution, which in turn leads to a long-range dipole-dipole repulsion between the particles.

This qualitative argument has been constructed into a quantitative theory by Stillinger [9] and Hurd [10], where they treated the particles at the interface as point charges using the linearised Poisson-Boltzmann equation (*i.e.*, Debye-Hückel theory). The point charge assumption is applicable when the particles are separated by an interparticle distance much greater than their diameter, *i.e.* $r >> d$. The linearisation assumption essentially states that the electrostatic energy for a mobile ion in the solution is much smaller than its thermal energy. In this regime, Stillinger determined the following expression for the interaction between two particles, represented by two point charges; $q = Ze$ at an electrolyte/air interface [9]

$$u(r) = \frac{Z^2e^2}{4\pi\varepsilon\varepsilon_0}\frac{2}{r}\int_0^\infty dx \frac{xJ_0(x)}{\{x^2 + (\kappa r)^2\}^{1/2} + x/e}, \tag{2.2}$$

where Z, e, ε_0 and ε are the total number of surface charges on the colloidal particle, the elementary charge, the permittivity of free space and the relative permittivity of the solvent, respectively. Additionally, $J_0(x)$ is the zeroth order Bessel function and κ is the inverse *Debye screening length*. The Debye length defines the characteristic distance from the surface over which ion concentrations are perturbed from their bulk values and the range over which electrostatic forces are felt [11] and can be thought as being the thickness of the electric double layer

$$\kappa^{-1} = \left(\frac{\varepsilon\varepsilon_0}{2\beta c_0 e^2} \right), \tag{2.3}$$

where $\beta = 1/k_B T$ and c_0 is the number density of monovalent ions in the bulk. This relationship indicates that κ is inversely proportional to the salt concentration of the polar phase, therefore in the presence of salt the thickness of the ionic atmosphere surrounding an adsorbed charged particle depends primarily on the properties of the bulk liquid and not on the property of the surface.

The expression for the interaction potential given by eqn.(2.2) crosses over from a screened coulomb interaction at small distances to a power law dipole-dipole interaction at large distances [12]. Hurd subsequently showed that this expression could be simplified in order to explicitly show the screened coulombic and dipolar constituents mentioned above

$$u_{el}(r) = \frac{Z^2 e^2}{2\pi\varepsilon\varepsilon_0} \frac{1}{r} \times \begin{cases} \dfrac{\varepsilon^2}{\varepsilon^2 - 1} \exp\left(-\kappa r\right) & (\kappa r \ll 10), \\ \\ \dfrac{1}{\varepsilon \left(\kappa r\right)^2} & (\kappa r > 10). \end{cases} \tag{2.4}$$

Eqn.(2.4) is a simplified potential which agrees with the exact Stillinger potential (eqn.(2.2)) to within 5% across the entire range of r studied [10]. These expressions have been widely used to study particles trapped between a polar and non-polar boundary.

However that work by Aveyard *et al.* [13] and Fletcher *et al.* [14] suggest an additional source of electrostatic interactions, especially for those at an oil/water interface. Aveyard *et al.* using polystyrene spheres, reported that a strong dependence on electrolyte concentration in water occurs at the air/water interface, while at an octane/water interface, particles remain highly ordered even at high electrolyte concentrations, indicating that electrostatic interactions are not being screened even at high salt levels. Clearly this effect cannot be explained by eqn.(2.4). This marked insensitivity to salt concentration has been interpreted as being caused by residual charges at the particle/oil interface and has been the catalyst for further theoretical studies.

Sun and Stirner [15] assumed that on contact with water, hydrophilic sulfate head groups on the particles surfaces dissociate, and surface charge dipoles perpendicular to surface are formed. Since the particles are covered by a thin water film when poured into the experimental setup, dipoles are found on the entire surface of the particle, resulting a maximum dipole-dipole repulsion between particles when $\theta = 90°$. This model however fails to account for the strong repulsion experienced by very hydrophobic particles *i.e.* $\theta > 150°$ [16], since particles of this nature under these assumptions will inevitably cancel out the effect of the dipoles on the surface of the colloid. In contrast Aveyard *et al.* [13] assume that residual charges are trapped on the surface of the colloid particle at the particle/oil interface. It is postulated that an effective dipole moment due to the residual charges and their image charges in the aqueous sub-phase is formed. The interesting point here is that this dipole-dipole interaction is mediated through the non-polar phase and is therefore very strong and long-ranged as it is not screened by the presence of counterions. This picture is also consistent with the fact that the repulsion is essentially unaffected by the pH or salt concentration (up to 1M NaCl) of the aqueous sub-phase [13, 14].

The model of Stillinger and Hurd is based upon the assumption that linear theory is reliable in capturing quantitatively the effects of the charges on the water side. However a high surface charge density σ on the water side of the colloid particle is frequently experienced in many experiments and consequently invalidates the use of linearised Debye-Hückel theory, which is based upon the incorporation of bare charges and relies on low particle surface charge densities that do not induce non-linear screening effects. A recent theory by Frydel *et al.* [17] has incorporated non-linear charge re-normalisation effects into the Pieranski dipole repulsions and found that this also led to a very weak dependence on salt concentration, which would give rise to the suggestion that further scrutiny of the force measurements in experiments may well be justified. However this theory under predicts the experimentally measured colloidal repulsions by at least an order of magnitude. Another important experimental observation was made very recently by Masschaele *et al.* [18], where they found that for particles equally immersed at the interface between a non-polar medium and water, the dipole moment can be quantitatively described by considering charge dissociation on the water side alone, *i.e.* the effect arising from the Stern layer only, with extra complications arising with heterogeneous repulsions being induced due to the type of preparation the particles undergo [19]. This observation goes so far as to predicting the correct order of magnitude for the strength of repulsion seen. However as highlighted above, very strong repulsions are observed for very hydrophobic particles at a octane/water interface where the Stern layer contribution, is likely to be minimal due to the very small particle/water interfacial area. Therefore one would conclude that the presence of residual charges at the particle/oil interface remains the most plausible explanation for the very strong electrostatic repulsions found in the case of very hydrophobic colloidal particles at an oil/water interface.

2.1.2 Van der Waals interaction

Another contribution to $u(r)$ is the *van der Waals* interaction, which can once again be expected to be more complex at the interface due to the presence of two dielectric media [2]. Van der Waals forces arise simply from dipole-dipole interactions between molecules and can be categorised into three different types [11, 20]:

1. ***London* or *dispersion* forces**: These are perhaps the most important of the van der Waals interactions because they are always present for atoms and molecules in the vicinity of one another, even for completely non-polar ones. They can be explained by a formal approach using quantum field theory but they can also be explained from a simpler and more physically intuitive viewpoint which is what we use below.

   For a non-polar atom that possess no permanent dipole, an instantaneous dipole moment of finite amplitude exists due to the motion of the electronic cloud around each molecule. This instantaneous dipole will generate an electric field which will polarise a nearby neutral atom. Polarisability arises from the displacement of its negatively charged electron cloud about the positively charged nucleus. The polarised atom will now feature a dipole moment, which will want to align itself with the former, to give rise to an attraction [7].

2. ***Debye* or *induction* interactions**: These are interactions between a permanent dipole and a fluctuating one. Here the polarisation originates from the permanent dipole of the polar molecule rather than an instantaneous dipole, but the polarisation of the neutral molecule is analogous to that experienced during dispersion interactions and therefore produces a similar interaction to that described above with temporary dipoles.

3. ***Keesom* forces**: These are simply a dipole-dipole interaction occurring between two permanent dipoles. Permanent dipoles have the tendency to align themselves parallel with each other, which gives rise to their alternative name as *orientational* interactions.

All three contributions above are important and can be all collectively considered in the van der Waals interaction between molecules which is of the form [11, 21]

$$u_{\text{vdw}}(r) = -\frac{C}{r^6}, \tag{2.5}$$

where C is the van der Waals parameter containing all the three interaction mechanisms described above. The functional form of the interaction implies a very steep fall off with increasing interparticle separation. This implies that the van der Waals force is a relatively short ranged force.

Van der Waals forces exist not only between individual atoms and molecules but also between larger colloidal particles. The interparticle van der Waals forces can be calculated using the *Hamaker approach*, which assumes complete additivity of forces between the individual atoms. The van der Waals interaction can be found for two macroscopic bodies by integrating eqn.(2.5) over all couples of interacting molecules followed by a subtraction of the interaction energy at infinite separation between the bodies [20].

The alternative approach is the Quantum Field Theoretical approach developed by Liftshitz that is more complex in detail and assumes the macrobodies as continuous media, characterised by macroscopic properties [22]. This was proposed from the argument that the use of additivity was unsatisfactory when applied to closely packed atoms in a condensed body. A full quantitative analysis of this approach is beyond the scope of this Thesis, but in this approach van der Waals forces are due to fluctuating electromagnetic fields in and around the macrobody, resulting in a net attraction [7].

The situation regarding the details of the van der Waals interaction become more complicated when the particles are situated at an interface. Despite this, we can use the following expression due to Gregory and Overbeek for the van der Waals interaction between colloidal particles at close distances (regarded as two infinitely large flat plates) [23]

$$u_{\mathrm{vdw}}(D) = -\frac{A_H}{12\pi D^2}, \tag{2.6}$$

where D is the closest distance between particles and A_H is the Hamaker constant. The Hamaker constant accounts for the material properties of both bulk phases and incorporates the retardation of the van der Waals force at large distances [21]. Specifically the Hamaker constant depends on the fractional volume of the particle immersed in each bulk fluid to account for the scenario of particles being confined to an interface [2]. Eqn.(2.6) utilises what is known as the *Derjaguin* approximation *i.e.,* using the knowledge we have on the interactions between planar surfaces to approximate for the interaction between curved ones, assuming that range of the interaction and the separation between the particles are much less than the radii of the spheres [7]. However the main point to note here is that at lower particle concentrations, the van der Waals interaction described is very small in magnitude when compared to the electrostatic interaction previously mentioned (see Table 2.1) [2], especially at the particle separations that we will be focussing on. Therefore we can assume that these forces do not induce major aggregation effects in the systems we wish to study.

2.1.3 Other interactions

2.1.3.1 Capillary interactions

Forces on the colloids acting perpendicular to the interface (*e.g.* gravity) result in strong lateral forces between the particles due to logarithmic deformations of the interface, creating what are known as *capillary forces* [2, 24]. The capillary interaction has no equivalent for colloids in bulk by definition. Capillary forces arise when curved *menisci* overlap between two bodies at an interface, generating an interaction that can be attractive or repulsive. For particles larger than $10\mu m$ in diameter, *Floatation forces* (created by a particle's weight). The nature of the Flotation forces is dependent on the signs of the meniscus slope angles ψ_1 and ψ_2 at the two contact lines of the particles being considered (see figure 2.3) [20]. For example, the capillary force is attractive when $\sin\psi_1 \sin\psi_2 > 0$ and repulsive when $\sin\psi_1 \sin\psi_2 < 0$. The liquid meniscus deforms in such a way that the gravitational potential energy of the two particles decreases when they approach

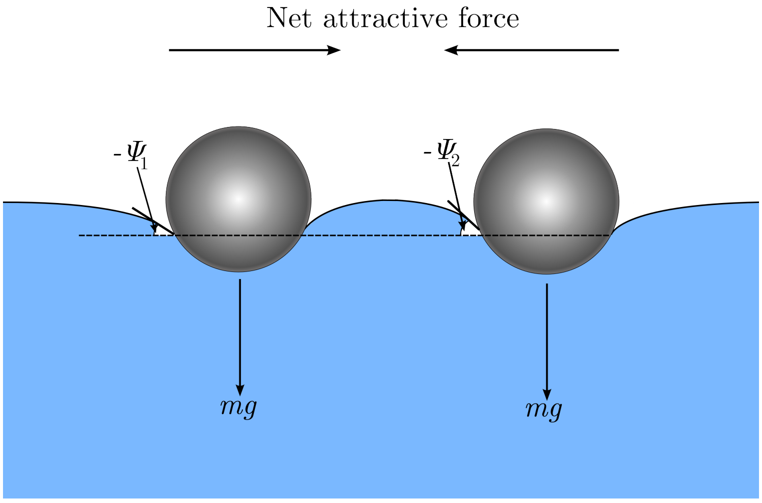

Figure 2.3: Side view schematic of colloidal particles at an interface experiencing a net attraction due to flotation forces. ψ_1 and ψ_2 are the angles subtended by meniscus slope lines of the two particles with the three-phase contact point (dotted line).

each other which is why this effect depends on particle weight. Flotation forces have a strong dependency on particle size and it has been shown that for particles with a radius less than $10\mu m$ these forces are negligible [20, 2]. Deformation of the interface around small spherical particles can exist for reasons not attributed to gravity. For example surface charges on colloids may also induce capillary effects. In this case, the deformation of the interface is the outcome of a combined effect of a vertical force, gravity and an inhomogeneous electromagnetic stress field acting on the interface, resulting in a power-law decay of the interface as opposed to a logarithmic decay as seen by Flotation forces; this is known as the *electro-dipping* effect [25].

In contrast to these, it has been reported recently that immersion forces can arise for floating particles where the particles display an irregular meniscus over their surface as a result of colloidal anisotropies, for instance surface irregularities (*i.e.* surface roughness, imbalance of surface charges), which in turn lead to anisotropic capillary interactions [25]. The three phase contact line in this situation would be undulated and result in a net attraction. This effect was used to explain a somewhat unexpected long-range attractive interaction between colloids spread at an interface [2].

2.1.3.2 Fluctuation forces

The instantaneous location of a fluid interface between two phases in equilibrium is not fixed but is generally affected by thermal fluctuations [2]. The resulting deviations $u(\mathbf{r})$ from a certain mean position of the interface are termed capillary waves which are easily generated, which would completely blur an interface in the absence of damping. However damping on a macroscopic length scale is introduced by either gravity or through a finite interface (*e.g.* on a droplet).

Fluctuations of the capillary waves through boundary conditions at the interface interfere with the adsorbed colloids that are seen as 'obstacles' to the permeating capillary wave. If two colloids are placed on the interface at a mutual distance r, the fluctuation spectrum of capillary waves will depend on r as will the associated free energy of the capillary waves, resulting in a distance dependent fluctuation force which can be considered as a thermal variant of the Casimir effect.

The fluctuation potential has two contributions [26, 27]: The first being the effects of the fluctuating interface itself with the three-phase contact line held at constant, equilibrium position. The second contribution stems from the random motion of the three-phase contact line. The contributions to the latter can be varied by certain constraints imposed on the colloid which strongly influence the fluctuation energy at large distances. For example, spherical colloids equally immersed in both phases that are *fixed* (*e.g.* by laser tweezers) experience a fluctuation potential that is double to that of *freely fluctuating* particles [ref]. However, the fluctuation potential is independent from the constraints previously mentioned when the particles are very close together and is said to be strong, much like the van der Waals interaction [2].

2.1.3.3 Hydrophobic and hydrophilic interactions

Another possible contribution to $u(r)$ are so-called *hydrophobic* or *hydrophilic* interactions [23]. Hydrophobic particles describe particles that repel water from their surface, so when they are dispersed in water, they experience an attraction with each other. Hydrophobicity arises from the fact that since hydrophobes are unable to form hydrogen bonds, water is repelled in favour of bonding with itself [7]. On the other hand, hydrophilic particles (*i.e.* particles that have an affinity with water) do the exact opposite; they exhibit a net repulsion with each other. Experimentally at an air/water interface, the hydrophobic interaction is only detectable for contact angles greater than 64° and the hydrophilic interaction, less than 15° when measured through water, assuming minimal surface roughness [23]. The shape of this interaction is believed to be of an exponential form and short ranged.

2.1.3.4 Many-body effects and other systems

Recently Brunner *et al.* investigated the density dependence of pair interactions in 2D colloidal suspensions [28]. An inversion of structural data was used to obtain the potentials and these authors found that while the interaction at lower

Interaction	Character	Strength (k_BT)	Particle size (d)
Electrostatic			
- dipolar	rep	$10 ... 10^5$	$10^{-9} ... 10^{-6}$m
Van der Waals	att	$0.1 ... 1$	$10^{-9} ... 10^{-6}$m
Capillary			
- electrostatic	att	$1 ... 10^3$	$10^{-7} ... 10^{-6}$m
- anisotropic	att/rep	$1 ... 10^5$	10^{-6}m

Table 2.1: Summary of the major interactions for charged colloidal particles at fluid-fluid interfaces [2]. The 'character' illustrates whether the interaction is attractive ('att') or repulsive ('rep'). The 'strength' of the interaction relates to the prefactor of the corresponding functionality of the interaction mechanism. The final column indicates the range of particle sizes for which the corresponding interactions are expected to play a significant role.

densities obeyed a repulsive Yukawa form, an attractive component emerged as the density increased. The authors attribute the attraction to many-body effects produced by screening of the macroions in the aqueous sub-phase.

Our discussions up until to now have focussed on charged particles residing at a polar/non-polar fluid interface. By choosing more exotic colloids and carefully selecting the two bulk mediums, in principle one can further tune the interaction between the particles. For example, superparamagnetic colloids at an air/water interface under the influence of an external magnetic field exhibits a dipole-dipole interaction whose strength can be easily controlled by the strength of the external field [29, 30, 31]. Additionally, glycerol colloids at the interface between air and a nematic liquid crystal have been shown to exhibit a rich variety of effective interactions between the particles [32, 33, 34].

We summarise the major interactions for colloids at fluid interfaces in Table 2.1, where it is clear for micron sized particles that the dominant interaction is the dipolar electrostatic interaction. We will use this fact heavily throughout the remainder of this Thesis.

2.2 Methods for measuring $u(r)$

In order to determine the specific nature of the interactions between colloidal particles in a given system, it is vital that we are able to measure these interactions accurately. In what follows, we outline the two main methods for measuring the pair interaction potential between colloidal particles at an interface.

2.2.1 Direct measurement of $u(r)$

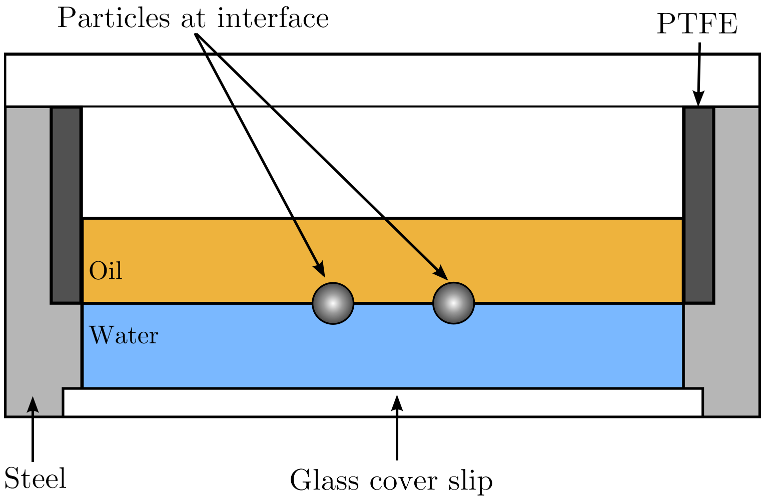

Figure 2.4: Schematic of the experimental laser tweezers setup used for determining the interaction potential between particles confined to a oil/water interface.

The first method is to measure $u(r)$ direct, *e.g.* using the laser tweezer method of Fletcher and co-workers [14]. The experimental setup is illustrated by figure 2.4: Two colloidal particles are trapped at a fluid interface with a fixed lateral distance using laser tweezers, where the laser trapping force can be tuned by changing the intensity of the laser. Initially one particle is fixed very strongly in the trap whilst the second particle, fixed with a weaker force is slowly moved towards the first particle. At sufficiently small interparticle separations, the second weakly held particle is ejected from the trap due to the interaction force of the first particle. This process is repeated for a range of laser trap strengths on the second particle, allowing a force-distance curve between the two colloids to obtained. We note that direct methods such as the one outlined above generally measure the *bare* pair interaction, *i.e.* the interaction between colloidal particles at infinite dilution. Many-body effects which are present at finite dilution are thus not included in such a measurement, but depletion effects (due to the solvent) and interfacial effects are included in such a measurement.

2.2.2 Inversion of pair correlation functions

The major alternative for determining $u(r)$ is to make use of *Integral Equation Theory* to address what is known as the *inverse problem*, that is, using structural measurements such as the radial distribution function $g(r)$, obtained from video microscopy measurements of colloidal monolayers or the structure factor $S(q)$, obtained from scattering experiments to obtain the effective pair potential $u(r)$. The effective pair potential is the interaction potential between two colloids that is mediated through all particles in the system to therefore include many-body effects. Therefore, it is **not** the bare colloidal interaction between two particles. The method has the advantage of allowing one to probe systems at higher densities in order to examine the density dependency on the interaction. However approximations are required since the full many-body problem involves an infinite number of particle interactions and is therefore analytically intractable. This route for determining $u(r)$ is one of the major points of focus for this Thesis. In order to understand how this method works, a description of the expressions that describe the structure and correlations of the colloidal system concerned is required, which will be fully explained in chapter 3.

2.3 Summary

The different mechanisms that contribute to the interaction potential in colloids at fluid interfaces have been discussed. The presence of an interface strongly modifies the interaction mechanisms in these systems due to the step change in dielectric constants and interfacial effects. In particular the origin of electrostatic, van der Waals and other contributions has been reviewed. The most significant contribution to $u(r)$ is the electrostatic interaction though and there is still considerable debate in the literature regarding its exact nature. For example, colloids at oil/water interfaces that feature a strong long-ranged repulsion between particles and a marked insensitivity to salt concentration in the aqueous sub-phase utilises mechanisms that presently are not entirely understood. Nevertheless, there has been significant advances in experimental and theoretical methods in measuring the forces in colloidal monolayers. However the accuracy of some of these methods, especially inversions schemes used in dense systems where many-body effects are important still needs to be improved; this is the subject of chapters 3, 4 and 5.

Chapter 3

Integral Equation Theory and computational methods

The interaction potential, $u(r)$ between particles at interfaces is intimately linked with the structure and therefore, the thermodynamic properties of the system. The procedure of relating thermodynamic and structural properties of translationally invariant systems to their interaction potential is provided by *Integral Equation Theories* (IET's). Specifically, a powerful method for obtaining the potential between particles is through the inversion of input structural data such as the radial distribution function $g(r)$, or the structure factor $S(q)$ using IET's [28, 35, 36, 37]. Indeed, there is a theorem which states that for any given $g(r)$ and number density ρ, there exists a unique pair potential $u(r)$ [38]. It should be emphasised that the potentials obtained from such inversions are *effective* pair potentials [38, 39], *i.e.* in addition to the bare pair potential, they may include many-body effects (*e.g.* for dense systems) or external fields (*e.g.* for monolayers adsorbed on a substrate). Nevertheless, such effective potentials can be of considerable help in analysing the behaviour and properties of adsorbed monolayers.

Ultimately what we seek is to simply link the structure of the fluid to the effective pair potential, $u(r)$. In a dilute solution, the *potential of mean force* is adequate for obtaining the pair potential between particles, when one can attain the details of the radial distribution function for that particular system. However, such a decomposition is not applicable to dense liquids since each particle in the liquid interacts with a large number of its neighbours. Consequently we must abandon common virial expansion techniques and look for methods that are reliable at high densities. The central ideas in most theories of liquids require what are known as *distribution functions*, which we will now discuss.

3.1 Classical fluid theory and distribution functions

The structural properties of an isotropic fluid are well-defined using a number of density correlation functions [40]. The simplest possible distribution function is a single particle distribution $\rho^{(1)}(\mathbf{r})$, and it is the probability that any one particle will be found at a particular position $\mathbf{r}$. This will vary depending on the medium in question; for example a crystal will be a periodic function with extremely sharp Bragg peaks at the particle locations due to long-range order being present, but in a fluid all the points within the volume are equivalent, which implies that $\rho^{(1)}(\mathbf{r})$ is independent of $\mathbf{r}$ [41]. For an isotropic fluid consisting of a number density ρ, it is well known that [42]

$$\frac{1}{V}\int \rho^{(1)}(\mathbf{r})d\mathbf{r} = \rho^{(1)} = \frac{N}{V} = \rho. \tag{3.1}$$

Accordingly in a fluid, the two particle density depends only on the magnitude of the difference between the vector positions of the two particles in question

$$\rho^{(2)}(\mathbf{r}, \mathbf{r}') = \rho^{(2)}(|\mathbf{r} - \mathbf{r}'|). \tag{3.2}$$

This brings us to a quantity that is of central importance in fluid theory, namely the *radial distribution function*

$$\rho^{(2)}(|\mathbf{r} - \mathbf{r}'|) = \rho^2 g^{(2)}(|\mathbf{r} - \mathbf{r}'|). \tag{3.3}$$

Physically, $\rho^2 g^{(2)}(|\mathbf{r} - \mathbf{r}'|)$ can be thought of as being the probability of finding a particle at position $\mathbf{r}'$ given that another is located at $\mathbf{r}$, implying that $g(r) \equiv g^{(2)}(|\mathbf{r} - \mathbf{r}'|)$ is a correlation function due to it 'correcting' for the 'non-independence' between particles. An equivalent definition for $g(r)$ can be obtained by taking an ensemble average over particle pairs [43]

$$g(r) = \frac{1}{\rho^2}\left\langle \sum_i \sum_{j \neq i} \delta(\mathbf{r}_i)\delta(\mathbf{r}_j - \mathbf{r}) \right\rangle = \frac{V}{N^2}\left\langle \sum_i \sum_{j \neq i} \delta(\mathbf{r} - \mathbf{r}_{ij}) \right\rangle. \tag{3.4}$$

Eqn.(3.4) is the algorithm that is commonly used in computer simulations when evaluating structural data sets and this will be discussed further in section 3.6.4. In general, $g(r)$ is defined as being the average number density of particles at a radial distance r from any given particle compared to the average number density in an ideal gas, at the same overall density [43]. The radial distribution function is of central importance because many thermodynamic functions can be related to $g(r)$ and it can also be determined experimentally to high precision.

Two more important quantities that are used to describe fluid structure which are closely related to radial distribution function are the *total correlation function*

$$h(r) = g(r) - 1, \tag{3.5}$$

and the *structure factor* $S(q)$ of a fluid, which is the Fourier transform of the total correlation function

$$S(q) = 1 + \rho \int h(r) e^{-i\mathbf{q}\cdot\mathbf{r}} d\mathbf{r}, \tag{3.6}$$

where $\mathbf{q}$ is the scattering wavevector and $q = |\mathbf{q}|$. $S(q)$ can be measured experimentally via scattering experiments. Specifically, monochromatic radiation impinges on a fluid sample and is scattered onto a detector which is used to measure the intensity of the scattered neutrons or photons [25]. This discussion shows that there is a one-to-one mapping between $g(r)$, $h(r)$ and $S(q)$, and typical forms of $g(r)$ and $S(q)$ for a isotropic fluid are shown in figure 3.1. The knowledge of $g(r)$ provides complete thermodynamic information about the system being studied since it is possible to express all thermodynamic quantities as integrals involving the radial distribution function. For example, the pressure P can be calculated from $g(r)$ using the so-called virial equation which in 2D is given by [44]

$$\frac{\beta P}{\rho} = 1 - \pi\rho \int_0^\infty r^2 dr g(r) \frac{d\beta u(r)}{dr}. \tag{3.7}$$

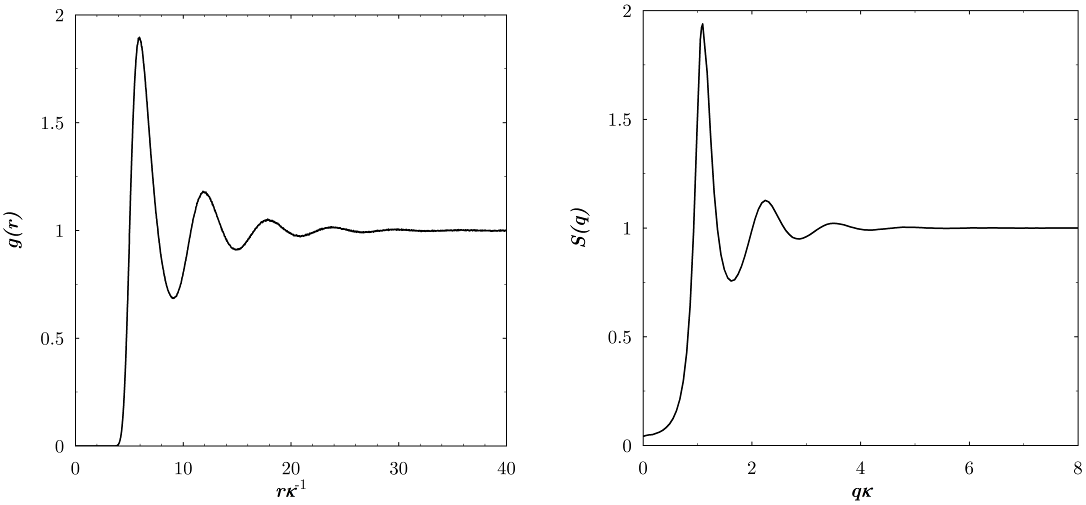

(a) (b)

Figure 3.1: Typical shapes of (a) the radial distribution function $g(r)$ and (b) the structure factor $S(q)$ for a dense colloidal fluid interacting through the Stillinger-Hurd repulsion (eqn.(2.4), where $\kappa^{-1} = 200n$m). Notice the oscillatory shape of both correlation functions, a common feature for fluids where the probability of a particle being located in successive co-ordination shells is always finite.

Similarly, the isothermal compressibility can be calculated from the so-called *compressibility equation*

$$\frac{\partial \beta P}{\partial \rho} = \left[1 + 2\pi\rho \int_0^{\infty} h(r) r dr \right]^{-1}. \tag{3.8}$$

In fact, the isothermal compressibility can be calculated using either the pressure equation (eqn.(3.7)), or using the compressibility equation (eqn.(3.8)). However, it is usual to find that each of these routes yield different results when an approximate expression for $g(r)$ is used for the integrations; this problem is known as *thermodynamic inconsistency*, and arises from the approximations that are undertaken when constructing $g(r)$ [6]. Methods to overcome this problem will be discussed in section 3.4.2 and in much greater detail in chapter 4.

3.2 Ornstein-Zernike equation

In 1914, Ornstein and Zernike proposed in their seminal paper *'Integral equation in liquid state theory'* [45] that $h(r)$ can be decomposed into two; a direct and indirect part. This was formalised with the direct part labelled the *direct correlation function*, $c(r)$. The indirect contribution is the influence propagated by say particle 1, on another particle say particle 3, which in turn exerts its influence on particle 2, directly or indirectly through the other particles in the system. This effect is weighted by the density and averaged over all positions of particle 3. This decomposes the total correlation function as follows [42]

$$h(r) = c(r) + \rho \int c(|\mathbf{r} - \mathbf{r}'|) h(r') d\mathbf{r}', \tag{3.9}$$

where $\mathbf{r} = \mathbf{r}_{12}$, $\mathbf{r}' = \mathbf{r}_{23}$ and therefore $\mathbf{r} - \mathbf{r}' = \mathbf{r}_{13}$. Eqn.(3.9) is called the *Ornstein-Zernike* (OZ) equation and can be used as the defining equation for the direct correlation function, $c(r)$. The term representing the indirect correlation in eqn.(3.9) appears as a convolution integral. The convolution, $f_1 * f_2$, of two integrable functions $f_1(\mathbf{r})$ and $f_2(\mathbf{r})$ is defined as

$$(f_1 * f_2)(\mathbf{r}) = \int d\mathbf{r}' f_1(\mathbf{r}') f_2(\mathbf{r} - \mathbf{r}') = \int d\mathbf{r}' f_2(\mathbf{r}') f_1(\mathbf{r} - \mathbf{r}'). \tag{3.10}$$

The convolution theorem states that

$$\int d(\mathbf{r}) e^{-i\mathbf{q}\cdot\mathbf{r}} (f_1 * f_2)(\mathbf{r}) = f_1(\mathbf{q}) f_2(\mathbf{q}), \tag{3.11}$$

Therefore, on taking the Fourier transform on both sides of eqn.(3.9) and utilising the convolution property given by eqn.(3.11), we obtain the following algebraic relation

$$h(q) = c(q) + \rho h(q)c(q), \tag{3.12}$$

where $h(q)$, $c(q)$ are the Fourier transforms of $h(r)$, $c(r)$ respectively. Eqn.(3.12) is the form of the OZ equation that is commonly used in actual calculations. In 2D, we can obtain the Fourier transforms of the correlation functions mentioned above from a *Hankel transform* [46]

$$h(q) = 2\pi \int_0^{2\pi} h(r)J_0(qr)dq. \tag{3.13}$$

Obtaining $h(q)$ allows for a direct calculation of $c(q)$ through the use of eqn.(3.12). To get back to real space, we need to perform an inverse Fourier transform, which (in 2D) can be achieved using the following expression

$$c(r) = \frac{1}{2\pi} \int_0^{2\pi} c(q)J_0(qr)dr. \tag{3.14}$$

Eqns.(3.12)-(3.14) will be used extensively to obtain the correlation functions required when inverting structural data to extract $u(r)$.

3.3 Closure relations

Having considered various correlation functions, we will now discuss the relationship between $g(r)$ and $u(r)$. In a dilute solution *i.e.*, $\rho \to 0$, $g(r) =$

$\exp[-\beta u(r)]$, we can write [41]

$$u(r) = -k_B T \ln g(r). \tag{3.15}$$

Eqn.(3.15) is derived from fixing two particles at a finite interparticle separation whilst the remaining $(N - 2)$ particles are canonically averaged over all configurations [42]. Generalising eqn.(3.15) to finite concentrations, we define the *potential of mean force* as

$$w(r) \equiv -k_B T \ln g(r). \tag{3.16}$$

Eqn.(3.15) is not suitable for dense systems where higher order density influences on the particles are required to deduce $u(r)$. In this case $g(r)$ is given by eqns.(3.5), (3.9), (3.12). Both equations are exact in the sense that all the information of the system is held within these equations, however because they introduce another function, the direct correlation function $c(r)$, another relationship or *closure* is required in order to determine $u(r)$, given $g(r)$. The exact relation that relates $g(r)$ and $c(r)$ to $u(r)$, reads as [6, 41]

$$g(r) = \exp[-\beta u(r) + g(r) - 1 - c(r) + B(r)], \tag{3.17}$$

where $B(r)$ is known as the *bridge function.* All known closures can be thought of as being approximations for $B(r)$, since the bridge function is analytically intractable. We are dealing with a many-body system; all particles within the fluid will have an effect on one another, thus approximations have to be made somewhere to essentially cut down the number of correlations. Common closures that are often employed are those known as the *Percus-Yevick* (PY) and *hypernetted chain* (HNC) approximations [41]. The use of diagrammatic methods to derive these approximations is beyond the scope of this work, instead we take a heuristic approach to motivate these approximate closures based upon the physical nature of $c(r)$.

3.3.1 Percus-Yevick closure

The function $c(r)$ represents the direct correlation between two particles in system containing $N-2$ other particles and this can be interpreted in the following way by re-arranging the OZ equation (eqn.(3.9)) like so [42]

$$c(r) = g(r) - \left[1 + \rho \int d(\mathbf{r}')c(r')\left\{g(|\mathbf{r}-\mathbf{r}'|) - 1\right\}\right] = g(r) - g_{ind}(r), \qquad (3.18)$$

where $g_{ind}(r)$ is the radial distribution function without the direct interaction between the two particles, $u(r)$. Since from eqn.(3.16) $g(r) = \exp[-\beta w(r)]$, we can approximate eqn.(3.18) as

$$c(r) = e^{-\beta w(r)} - e^{-\beta[w(r)-u(r)]}. \qquad (3.19)$$

At this point, it is convenient to introduce what is known as the *cavity function*

$$y(r) = e^{\beta u(r)} g(r). \qquad (3.20)$$

The cavity function $y(r)$ can be considered as describing the correlations between particle pairs when the direct interaction, $u(r)$ between them is turned off [47]. This function plays a prominent role in the iterative procedures that will be described in chapters 4 and 5. Substituting eqn.(3.20) into eqn.(3.19) we find

$$c(r) = g(r) - y(r). \tag{3.21}$$

Substituting eqn.(3.21) into the closure relation eqn.(3.17), the approximation for $B(r)$ now reads as

$$B_{\mathrm{PY}}(r) = -[g(r) - c(r)] + 1 + \ln[g(r) - c(r)]. \tag{3.22}$$

We now have a closed form for $B(r)$ in terms of $h(r)$, $c(r)$ and $u(r)$.

3.3.2 Hypernetted-Chain closure

The HNC equation, whose name stems from its diagrammatic derivation [48], can be obtained in a similar manner, however now we interpret the $g_{indirect}(r)$ term differently by assuming that $\beta[w(r) - u(r)]$ in eqn.(3.19) term is small, such that we can further approximate eqn.(3.19) by

$$\begin{aligned} c(r) &= e^{-\beta w(r)} - 1 + \beta[w(r) - u(r)], \\ &= g(r) - 1 - \ln y(r). \end{aligned} \tag{3.23}$$

Substituting eqn.(3.23) into eqn.(3.17) gives

$$B_{\mathrm{HNC}}(r) = 0. \tag{3.24}$$

3.3.3 Mean Spherical Approximation

Many systems that are of great interest in liquid state theory consist of potentials that have a hard core, excluded volume region plus a long-range tail. Such systems motivate a closure relation known as the *Mean Spherical Approximation* (MSA), first introduced into liquid state theory by Lebowitz and Percus in 1966 [49]. In the MSA, the radial distribution function and direct correlation function are approximated by

$$\begin{aligned} g(r) &= \quad 0 & r &< d, \\ c(r) &= -\beta u_2(r) & r &> d, \end{aligned} \tag{3.25}$$

where $u_2(r)$ is the potential situated outside the core region *i.e.*, for $r > d$. When supplemented with the OZ relation (eqn.(3.9)), these two expressions combine to yield a closed integral equation for $g(r)$. The MSA is well suited for short-range attractive and repulsive potentials, but it can predict spurious values for $g(r)$ near contact point for particles interacting in a dilute regime; this is because the MSA assumes a short-ranged interaction. One way to overcome this is to modify the MSA as follows: The MSA assumes the total potential is split into two; $u(r) = u_1(r)+u_2(r)$, with the core region obeying a hard-disk (HD) potential *i.e.* $u_1(r) = \infty$ for $r < d$. By generalising the MSA in such a way that the core potential is a soft repulsion and the tail is an attraction, one can deduce what is known as the *soft-core MSA* (SMSA) closure, which reads as [50]

$$g(r) = \exp(-\beta u_1(r))(1 + h(r) - c(r) - \beta u_2(r)). \tag{3.26}$$

Eqn.(3.26) reduces to the PY approximation (eqn.(3.21)) when $u_2(r)$ is small *i.e.* for potentials that have no attractive well outside the core. This closure has proved successful in approximating equations of state for Lennard-Jones fluids [41]. The SMSA closure will be expanded upon in section 4.2 where it will form the basis for one of the thermodynamically consistent inversion schemes that we develop.

3.4 One-Step inversions

3.4.1 Standard IET solutions

The closure relations discussed in the previous section provide a simple method for inverting $g(r)$ to obtain $u(r)$. Specifically substituting eqns.(3.21) and (3.23) into eqn.(3.17) both lead to closed equations that relate $u(r)$ to all the correlation functions described in section 3.1

$$\beta u(r) = \ln\left[1 - \frac{c(r)}{g(r)}\right], \qquad \text{(PY)} \tag{3.27}$$

$$\beta u(r) = h(r) + c(r) - \ln\left[g(r)\right]. \qquad \text{(HNC)} \tag{3.28}$$

Inversion schemes based on eqns.(3.27) and (3.28) allow us to calculate $u(r)$ from $g(r)$ using only a single iteration. Such inversion schemes are therefore called *one-step* (OS) inversion methods. These are the simplest inversion schemes because one assumes a simple form for the bridge function or equivalently, a simple closure relation in the integral equation theory. The HNC and PY closure relations have been used by a number of groups to invert pair-correlation data for a variety of 2D colloidal systems [6, 28, 35, 36, 51, 52]. However it is widely recognised that such closure relations are only approximate and may sometimes lead to inaccurate results. In particular, the HNC approximation appears to be more accurate for long-ranged, soft potentials while the PY approximation appears to be more accurate for short ranged, steep repulsions (*e.g.* HD potentials) [6].

3.4.2 Mixed closure methods

The problem of thermodynamic consistency was touched upon in section 3.1, where due to the approximations in constructing a closure relation (*i.e.*, the assumptions made in deducing $B(r)$), different routes for calculating the same thermodynamic quantity *e.g.* compressibility or free energy, yields a different answer. This directly affects the accuracy of the OS inversion methods presented in section 3.4.1 because the approximations made in constructing $B(r)$ are made with no *a priori* knowledge regarding the potential of the system. This problem of thermodynamic inconsistency can be addressed by modifying the integral equation through the inclusion within the closure relation of a function which contains one or more fitting parameters [6]. These parameters are then tuned until thermodynamic consistency is achieved. A particularly simple example of such closure relations is the Rogers and Young (RY) closure that is a mixture of the HNC and PY closures and reads [53]

$$g(r) = \exp\left[-\beta u(r)\right]\left[1 + \frac{\exp\left[\gamma(r) f(r)\right] - 1}{f(r)}\right], \qquad \text{(RY)} \qquad (3.29)$$

where $f(r)$ is an interpolating function with the form

$$f(r) = 1 - \exp\left(-\alpha r\right). \tag{3.30}$$

Thermodynamic consistency is achieved by varying the parameter $\alpha \in \{0, \infty\}$. Eqn.(3.29) reduces to the PY and HNC respectively when $\alpha = 0$ and $\alpha = \infty$. This equation however assumes that the thermodynamically consistent closure is in-between the HNC and PY approximations, which is only correct if the potential is purely repulsive. In chapters 4 and 5, we will introduce more general thermodynamically consistent closure relations that are applicable to both repulsive and attractive potentials.

3.5 Alternatives to closure methods: Predictor-Corrector routines.

As discussed before, the OS methods make severe approximations for the bridge function $B(r)$ that may not be suitable for the specific interaction at hand, since $B(r)$ will inevitably depend on the interactions occurring in a particular system [37]. An alternative method for improving the accuracy of the OS methods is the simulation based *Predictor-Corrector* (PC) method first developed by Reatto *et al* [54]; in principle this allows one to determine the exact solution for $B(r)$ through iterative means. Reatto *et al* assumes the use of the bridge function of a HS fluid with diameter d, $B_{\mathrm{HS}}(r)$, which is chosen by means of the following criterion [47]

$$\int \frac{\partial B_{\mathrm{HS}}(r)}{\partial d}\left[g(r) - g_{\mathrm{HS}}(r)\right] dr = 0, \tag{3.31}$$

where $g_{\mathrm{HS}}(r)$ is the radial distribution function corresponding to the HS fluid. The interaction potential $u(r)$ is directly linked to the bridge function, $B(r)$ through

$$\beta u(r) = h(r) - c(r) - \ln\left[h(r) + 1\right] + B(r). \tag{3.32}$$

Assuming $B(r) = B_{\mathrm{HS}}(r)$ in eqn.(3.32) allows for an initial guess for the interaction potential of the system, $u'(r)$. Reatto *et al* performed simulations using $u'(r)$ in order to determine the corresponding correlation functions $c'(r)$, $y'(r)$, $h'(r)$, and hence an improved estimate for the bridge function through the approximation

$$B(r) \approx c'(r) + \ln y'(r) - h'(r). \tag{3.33}$$

This was then repeated until convergence was achieved for the output potential, $u(r)$. The simulation based PC scheme of Reatto *et al* that was originally constructed for 3D systems has recently been extended to 2D by Rao *et al* [55]. This method in principle yields exact results for $u(r)$ but it is computationally very expensive because computer simulations of the system are required at each iteration. A computationally cheaper PC method in 3D has recently been constructed by Rajagopalan [36, 37], which requires the HS bridge function $B_{\mathrm{HS}}(r)$ being used for *every* iteration. This method is computationally much faster since very accurate expressions for $B_{\mathrm{HS}}(r)$ are known so that the only parameter changed at each iteration of the PC method is the HS diameter. In chapters 4 and 5 we extend the HSPC method of Rajagopalan to 2D.

3.6 Monte Carlo simulations

The previous sections have introduced various methods in order to extract the effective pair potential $u(r)$, from the radial distribution function $g(r)$, or equivalently the structure factor, $S(q)$. To test the accuracy of these and the schemes we develop in chapter 4, we require accurate $g(r)$ data of systems interacting via known pair potentials and this data will be initially generated through the use of computer simulations. This route has at least two advantages: Firstly, it is straightforward to generate very accurate $g(r)$ data from long simulation runs. Secondly, the use of simulations allows one to know the underlying potential *a priori*, enabling a direct comparison between the inverted potential and the original potential. The two main simulation methods that are suitable for generating the necessary $g(r)$ data are Molecular Dynamics (MD) and Monte Carlo (MC) simulations. MC methods do not follow the time evolution of the system unlike MD simulations, therefore dynamical properties of the system cannot be calculated, but a large number of configurations of the system can be generated allowing the equilibrium properties of the system to be calculated by performing an ensemble average over a large number of snapshots. We have chosen to use the MC method in this thesis and we will now discuss the relevant details of the MC simulation for colloids at interfaces.

3.6.1 Principles of Monte Carlo

The main idea behind all MC simulations is to generate a large number of configurations randomly and subsequently to calculate the average of a particular quantity of the system via an ensemble average [43]. However for our study, the main challenge is to design a scheme which efficiently samples the equilibrium distribution of the statistical mechanical ensemble that we wish to study. Specifically, we wish to study our colloidal monolayer within the canonical ensemble (N, V, T), which is the most commonly used ensemble in statistical thermodynamics, in which the system has a fixed number of particles N within a fixed volume V held at a fixed temperature T. For such an NVT ensemble, the probability P_i of finding the system in a particular microscopic state i according to the Boltzmann distribution law is [56]

$$P_i = \frac{\exp\left[-\beta u(\mathbf{r}_i)\right]}{\int_r \exp\left[-\beta u(\mathbf{r})\right] d\mathbf{r}}. \tag{3.34}$$

Eqn.(3.34) is what has to be satisfied in order to conduct a molecular simulation so that it remains in the canonical ensemble. Therefore an appropriate algorithm needs to be developed and this is achieved using the Metropolis algorithm.

3.6.2 Metropolis Monte Carlo algorithm

Metropolis *et al* proved that one could sample averages in the canonical ensemble and thus satisfy eqn.(3.34) by treating the problem as if it were a *Markov Chain* [57]. A Markov Chain is a sequence of trials that satisfies two conditions [43]:

1. The outcome of each trial has only a finite set of outcomes that defines what is called the *state space* of what is being tested.
2. The outcome of each trial depends on the outcome of the previous trial only.

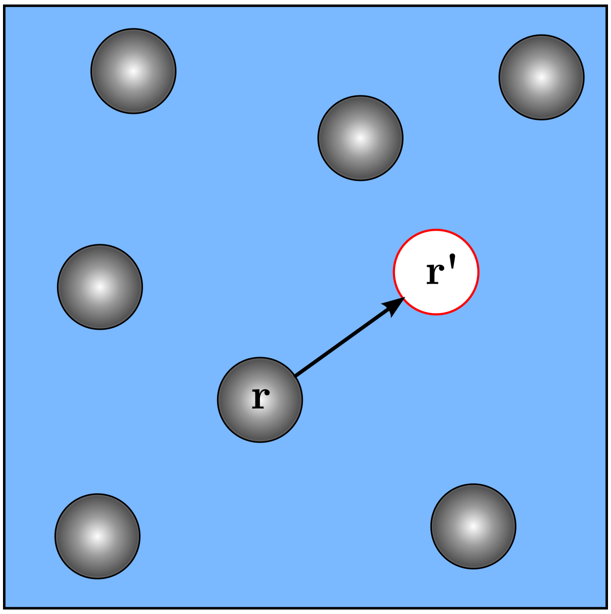

Figure 3.2: Possible choice of particle movement from position $\mathbf{r}$ to $\mathbf{r}'$ in MC simulations.

This sequence of events implies that the Markov chain is stochastic and only depends on the current state the system is in, therefore the knowledge of how the system actually reached that particular point is irrelevant. To illustrate the statements above, we consider an example using the Metropolis procedure for a 2D particle array in the NVT ensemble (see figure 3.2) [58]:

1. For a fixed number of particles N held within the monolayer, choose one at random and calculate its energy $u(\mathbf{r})$.
2. Give the particle a random displacement $\mathbf{r}' = \mathbf{r} + \Delta\mathbf{r}$ and calculate its new energy $u(\mathbf{r}')$.
3. Accept the move from state $\mathbf{r}$ to $\mathbf{r}'$ based on an acceptance probability:

$$A(\mathbf{r} \to \mathbf{r}') = min(1, \exp(-\beta[u(\mathbf{r}') - u(\mathbf{r})]). \tag{3.35}$$

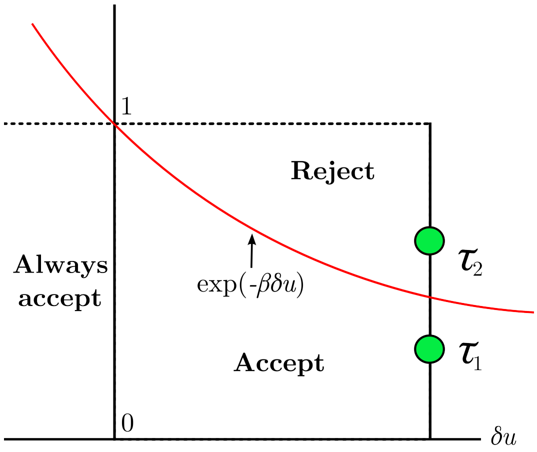

Figure 3.3: Accepting uphill moves in MC simulations through the use of $A(\mathbf{r} \rightarrow \mathbf{r}')$ (eqn.(3.35)).

Eqn.(3.35) defines the acceptance probability to create the required equilibrium conditions. If the move is downhill in energy *i.e.*, $\delta u = u(\mathbf{r}') - u(\mathbf{r}) < 0$ then the move is accepted straight away. However if the move is uphill in energy *i.e.*, $\delta u > 0$ then the move is accepted with the probability $\exp(-\beta[u(\mathbf{r}') - u(\mathbf{r})])$. This is achieved by computing a random number that is uniformly distributed over the range $(0, 1)$ (see figure 3.3). For a given δu, if the random number is less than $\exp(-\beta[u(\mathbf{r}') - u(\mathbf{r})])$ as shown by the position of τ_1, then the move is accepted and counted in the averaging. If the random number is larger than $\exp(-\beta[u(\mathbf{r}') - u(\mathbf{r})])$ as shown by τ_2, the move is rejected and returned to its original position and again counted in the averaging. The inclusion of this particular acceptance probability arises from imposing the requirement known as *detailed balance*, which ensures the final distribution of micro-states obeys the canonical Boltzmann distribution [58].

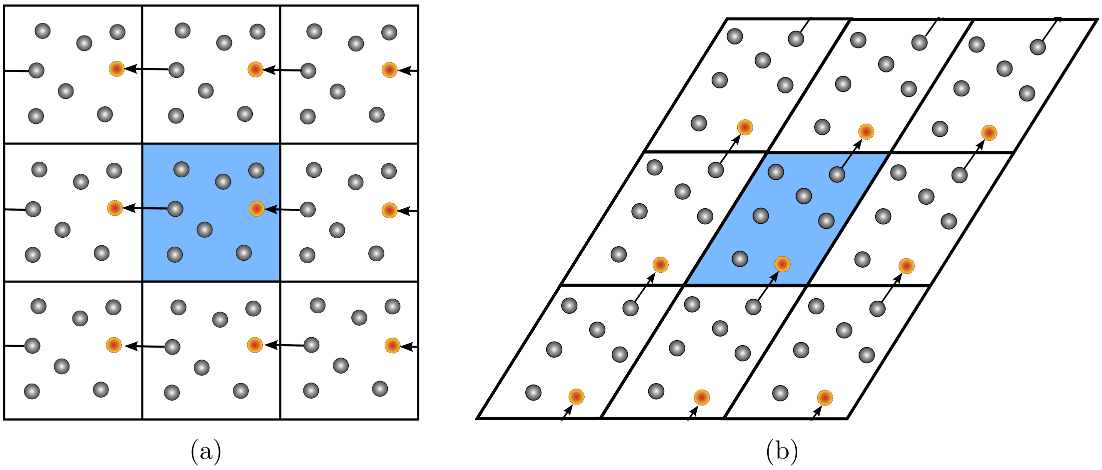

Figure 3.4: Implementation of Periodic Boundary Conditions for (a) a square and (b) a rhombic unit cell topology. The coloured ring indicates the position over the boundary to where the particle would be relocated. This is replicated in all cells around the original unit cell in the centre.

3.6.3 Monte Carlo boundary conditions

MC simulations, like any other simulation technique, require boundary conditions to specify what happens when a particle comes to the edge of the simulation box. Precautions are undertaken so that no inadvertent edge effects occur that may induce spurious statistics into the ensemble averaging. Specifically we employ what are known as *periodic boundary conditions* (PBC), which are often used to simulate bulk systems that are sufficiently far away enough from the edge. This is implemented by specifying that when a particle leaves the simulation box passing through a particular face, it will re-emerge in the simulation box at the opposite face. This essentially makes the simulation box an infinite system of periodically repeating sub-systems. This concept is illustrated in figure 3.4 for square and rhombic geometries, both of which will be used for the data that is generated in chapters 5 and 7. Note that due to its periodic nature, PBC's minimise but do

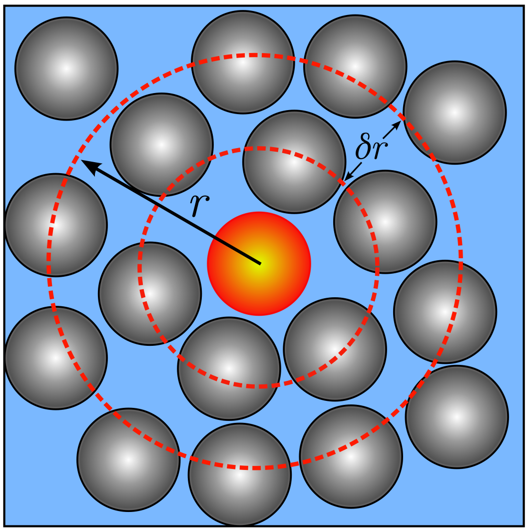

Figure 3.5: Physical interpretation of $g(r)$. The red dashed rings of width δr can be considered as 'bins' where if a particle centre is located within it, it will be counted for that particular snapshot and then used in the averaging process.

not eliminate finite size effects.

A consequence of using PBC is that once a particle has re-entered at opposite side of the simulation box, the surrounding particles that were in the vicinity before the MC move was made will no longer be in the vicinity. To overcome this, we implement the *minimum image convention* (MIC), where the chosen particle interacts with the closest image of the remaining particles in the system [43].

3.6.4 Radial distribution function from simulations

In this section we will describe how we calculate the radial distribution function $g(r)$, from our simulation data. Physically $g(r)$ can be thought as being the number of particles at a distance r from a given particle, compared with the number at same distance in an ideal gas at the same overall density [43]. Referring specifically to figure 3.5, $g(r)$ can be calculated as follows:

1. Consider each particle in an N particle system in turn. Sort all inter-particle separations into a histogram $n_{his}(b)$, where each bin has a width δr, by counting all particles that lie in-between a radial distance $r \rightarrow r + \delta r$ from the centre of chosen particle.

2. Assuming there are N_S statistically independent snapshots taken of the system, the average number of particles a given distance away from a chosen particle is
$$n(b) = \frac{n_{his}(b)}{N \times N_s}. \tag{3.36}$$

3. The average number of particles at the same interval of an ideal gas at the same density ρ is,
$$n^{id}(b) = 2\pi\rho \left[(r + \delta r)^2 - r^2\right]. \tag{3.37}$$

4. To ensure that $g(r) = 1$ for data with no structure, we must divide our original histogram of particle separations $n(b)$, by the equivalent number in an ideal gas $n^{id}(b)$ to obtain the definition of the radial distribution function
$$g\left(r + \frac{\delta r}{2}\right) = \frac{n(b)}{n^{id}(b)}. \tag{3.38}$$

This is shown pictorially by figure 3.5, where the concentric rings surrounding the chosen particle (the central red particle in this case) can be considered as being ‘bins’ of width δr, so that particle centres within a particular bin are counted and averaged over many snapshots.

3.7 Summary

In this chapter we have discussed the salient properties of the radial distribution function $g(r)$ and its related distribution functions, namely the total correlation function $h(r)$, the structure factor $S(q)$ and the direct correlation function $c(r)$. We have shown that with the use of the Ornstein Zernike equation (eqn.(3.9)) and relevant closure relations (*e.g.*, Hypernetted-Chain and Percus-Yevick solutions), one can find a suitable method in obtaining $u(r)$ for a 2D liquid. The complexity of these methods range from one-step methods to Predictor-Corrector methods, the latter being the focus of chapters 4 and 5.

We have also provided details on how to simulate the colloidal monolayers through Monte Carlo simulations and discussed relevant boundary conditions. Finally, we have provided details on how to calculate $g(r)$ physically from particle co-ordinates obtained from our simulations. All these tools will be used extensively in chapters 4 and 5, where we construct more accurate Predictor-Corrector and thermodynamically consistent inversion schemes for colloidal monolayers.

Chapter 4

Thermodynamically consistent inversion schemes

In chapter 3, we introduced a number of pair correlation functions that characterise the structure of a liquid and discussed how they are related to the effective pair potential, $u(r)$ via Integral Equation Theory. We also showed that it is in principle, possible to extract $u(r)$ from the radial distribution function $g(r)$ or the structure factor $S(q)$ of the liquid. However due to the many-body nature of these systems, approximations need to be made for the form of the Bridge function $B(r)$, in order to find a closed equation that can link the pair potential with $g(r)$ or $S(q)$. The most common approximations for $B(r)$ (or equivalently the closure relations) are the Percus-Yevick (PY) and Hypernetted-Chain (HNC) approximation. However these approximations can sometimes lead to inaccurate inverted potentials because they do not satisfy thermodynamic consistency as discussed in section 3.4.2. The objective of this chapter is to outline two thermodynamically consistent inversion methods that we have developed for extracting effective pair potentials from $g(r)$ or $S(q)$ of a 2D system. These self consistent inversion methods are labelled as being *thermodynamically consistent* due to the fact that they are continually iterated until the output satisfy given thermodynamic consistency criteria.

As we shall see in the next chapter, these thermodynamically consistent schemes lead to much more accurate inverted potentials compared to the one-step (OS) inversion schemes discussed above. The first is known as the *Hard-Disk Predictor-Corrector* (HDPC) method, which utilises the use of a hard-disk (HD) bridge function, and the second is known as the *HMSA* method, which is a mixed closure scheme that works in a similar manner to the RY closure described in section 3.4.2.

4.1 2D Predictor-Corrector method

If one is willing to sacrifice the convenience of OS inversions for a significant improvement in accuracy, the exact closure can be incorporated in the inversion by employing an iterative scheme in combination with computer simulations at each iteration, as first illustrated by Reatto *et al.* [54]. In order to place the iterative methods we propose within a unified framework, it is convenient to recast the Ornstein-Zernike (OZ) equation and its closure as follows.

The basic idea behind any inversion scheme based on the OZ equation is to use the OZ equation *i.e.*

$$h(q) = c(q) + \rho h(q)c(q), \tag{4.1}$$

where $h(q)$ is the total correlation function and $c(q)$ is the direct correlation function in Fourier space, in combination with the general closure relation [6, 41]

$$g(r) = \exp[-\beta u(r) + g(r) - 1 - c(r) + B(r)], \tag{4.2}$$

to extract $u(r)$ from the experimental $g(r)$ or $S(q)$ at the known density ρ, of the system. By rearranging the OZ equation above, we can relate $c(r)$ in the closure to the experimental data $S(q)$ through $c(q)$ [37]

$$c(q) = \frac{1}{\rho}\left[1 - \frac{1}{S(q)}\right]. \tag{4.3}$$

It is the lack of a direct link between the experimental data and $B(r)$ that prevents one from using eqn.(4.2) to obtain $u(r)$ directly from $S(q)$. The OS inversion methods circumvent this problem by either neglecting $B(r)$ altogether (as in the HNC closure) or approximating it in terms of known information (as in the PY closure). In this section, we extend the 3D PC method of Rajagopalan and Rao [37] to 2D as a means to providing a more accurate inversion method.

4.1.1 Predictor equation

We begin our derivations by providing what is known as the *Predictor* equation which can be used to calculate the potential of the 2D system of interest in relation to the correlation functions of a reference system. To do this, we rewrite eqn.(4.2) for the actual system relative to a 2D reference system interacting via a potential $u'(r)$

$$\beta u(r) = \ln\left(\frac{y'(r)}{[h(r)+1]}\right) + [h(r) - h'(r)] - [c(r) - c'(r)] + \Delta, \tag{4.4}$$

where the prime identifies the correlation functions pertaining to the reference system and $\Delta = [B(r) - B'(r)]$. In eqn.(4.4), $y(r)$ is the cavity function given by

$$y(r) = e^{\beta u(r)} g(r), \tag{4.5}$$

which was first introduced in section 3.3.1 whilst deriving the PY closure and it deserves special mention here. The cavity function, in contrast to $g(r)$ which for HD systems has a discontinuity at $r = d$ by definition, has the useful property that it is continuous for all r. It agrees with $g(r)$ when $u(r) = 0$, and its name stems from the fact that it is a smooth, non-zero continuation of $g(r)$ into the core region of r, *i.e.*, for $r < d$. The finite nature of $y(r)$ for $r < d$ is because the factor exp$[\beta u(r)]$ removes any discontinuities from $g(r)$, which is particularly important for the case of HD fluid, where this feature will be utilised for our thermodynamic consistency measurements in section 4.1.3. The calculation of $y(r)$ for a HD system can be problematic due to the infinite nature of $u(r)$ at low r, however as we shall explain, in section 4.1.2 the core values of $y(r)$ can be calculated through the use of the method devised by Henderson and Grundke [59]. If one insists upon the use of simulations to deduce the reference state correlation functions, this method lacks the efficiency needed for quick solutions of $y(r)$ and hence $u(r)$, which directly affects the choice of correlation parameters pertaining to our reference potential, $u'(r)$.

Therefore the key task in constructing the PC scheme is to choose a suitable reference potential such that $\Delta \to 0$. For the reference system in their 3D scheme, Rajagopalan and Rao use a hard-sphere (HS) potential. This approximation leads to remarkably accurate inversions for a wide range of potentials in 3D [37]. This success is due to the fact that $B(r)$ is of short range and is generally determined by the repulsive core of $u(r)$ [6, 41], so that replacing $B(r)$ with the HS bridge function is a good approximation. Following Rajagopalan and Rao, we therefore choose the HD potential as our reference potential in our 2D inversion scheme, *i.e.* $u'(r) = u_d(r)$ where d is the HD diameter. The HD potential is simply a step function that obeys the following

$$u_d(r) = \begin{cases} \infty; & r < d, \\ 0; & r > d. \end{cases}$$

Referring to eqns.(4.3), (4.4) our HDPC method therefore requires accurate and convenient expressions for various HD correlation functions, including $c_d(r)$, $h_d(r)$, $y_d(r)$ and $S_d(q)$.

4.1.2 Hard-disk correlation functions

For the direct correlation function $c_d(r)$, we use the analytical expression proposed by Guo and Riebel [60]

$$\begin{aligned} c_d(r) = {} & \Theta\left(1-r\right)\left[-\frac{1-p\eta^2}{\left(1-2\eta+p\eta^2\right)^2}\right. \\ & \left.\left\{1-a^2\eta+a^2\eta\frac{2}{\pi}\left[\arccos\left(\frac{r}{a}\right)-\frac{r}{a}\left(1-\frac{r^2}{a^2}\right)^{\frac{1}{2}}\right]\right\}\right], \end{aligned} \tag{4.6}$$

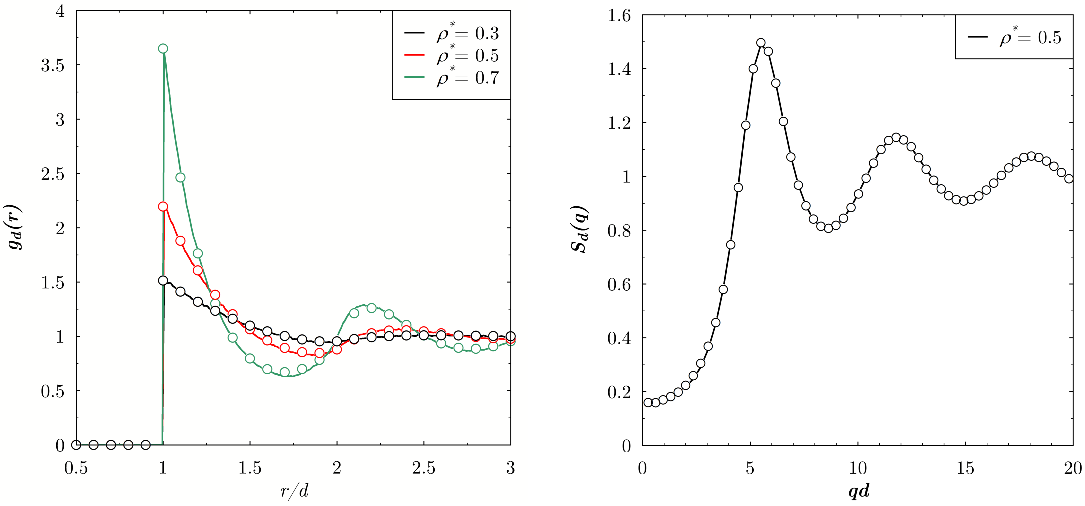

(a) (b)

Figure 4.1: (a) HD $g(r)$ at various reduced densities ($\rho^* = \rho d^2$) and (b) HD structure factor at $\rho^* = 0.5$. The solid lines are the theoretical predictions and the open circles are the corresponding simulation results.

where $\Theta(x)$ is the Heaviside step function, $p = \left(4\sqrt{3}\pi - 12\right)/\pi^2$, $\eta = \pi\rho d^2/4$ and a is a function of η with a convenient parametrisation given in ref.[60]; this parametrisation is rather long and therefore it is not reproduced here.

Knowing $c_d(r)$, the HD radial distribution function $g_d(r)$ can be readily calculated using the OZ relation (eqn.(4.1)). Denoting the resultant radial distribution function as $g_{d0}(r)$, comparison with simulation results on HD fluids shows that $g_{d0}(r)$ is accurate for all r except near the contact point $r = d$. Following Verlet and Weis [61], we therefore include a correction term to $g_{d0}(r)$ as follows. We assume that the corrected HD radial distribution function is given by

$$g_d(r) = g_{d0}(r) + \delta g_d(r), \tag{4.7}$$

where $\delta g_d(r)$ is our correction term given by

$$\delta g_d(r) = \frac{C}{r}\exp[-\mu(r-d)]\cos(r-d), \tag{4.8}$$

where C and μ are constants that are found by requiring that the pressure calculated from the HD pressure equation,

$$\frac{pA}{Nk_BT} = 1 + 2\eta y(d), \tag{4.9}$$

where p is the pressure, A is the area and N is the number of particles of the system respectively, and the compressibility calculated from the 2D compressibility equation,

$$k_BT\left(\frac{\partial\rho}{\partial p}\right)_T = 1 + 2\pi\rho\int_0^\infty h(r)rdr, \tag{4.10}$$

are equal to the corresponding expressions calculated from the HD equation of state. Specifically, we use the simple but accurate equation of state to represent the compressibility factor analytically, as proposed by Santos *et al.* [62]

$$Z(\eta) = \left[1 - 2\eta + \frac{2\eta_0 - 1}{\eta_0^2}\eta^2\right]^{-1}, \tag{4.11}$$

where $\eta_0 = \sqrt{3}\pi/6 = 0.9069$ is closed-packed area fraction for HD.

$S_d(q)$ is obtained from the corrected $g_d(r)$ via Fourier transform (eqn.(3.6)). In all cases, all Fourier transforms are performed using the efficient numerical Fourier transform algorithm provided by Lado [63], which we present in Appendix A for completeness. In figure 4.1, we compare our calculated results for both $g_d(r)$ and

$S_d(q)$ with MC simulations on HD fluids at various reduced densities. We see that the agreement between the two is excellent across the entire range of r and q, even for relatively high densities.

Finally, we turn our attention to the HD cavity function $y_d(r)$. From eqn.(4.5), we see that $y_d(r) = g_d(r)$ for $r \geq d$. However for $r < d$, we cannot calculate $y_d(r)$ directly using eqn.(4.5) because the potential is infinite in this region. Instead we use the method of Henderson and Grundke here [59]. Specifically for $r < d$, we assume that $\ln y_d(r)$ has the polynomial form

$$\ln y(r) = \sum_{n=0}^{3} a_n r^n, \tag{4.12}$$

and we determine the coefficients $\{a_n\}$ using the boundary conditions for $y_d(r)$ at $r = 0$ and $r = d$. At $r = 0$, $\ln y_d(r)$ obeys the boundary conditions

$$\ln y_d(0) = \mu_{ex}, \tag{4.13}$$

$$\frac{\partial}{\partial r} \ln y_d(r)|_{r=0} = -2d\rho g_d(d), \tag{4.14}$$

which have been derived by Hoover and Poirier [64] and Meeron and Siegert [65] respectively. In eqn.(4.13), μ_{ex} is the excess chemical potential given by

$$\mu_{ex} = \eta \frac{\partial F_{ex}}{\partial \eta}, \tag{4.15}$$

and F_{ex} is the excess Helmholtz free energy which can be obtained by integrating

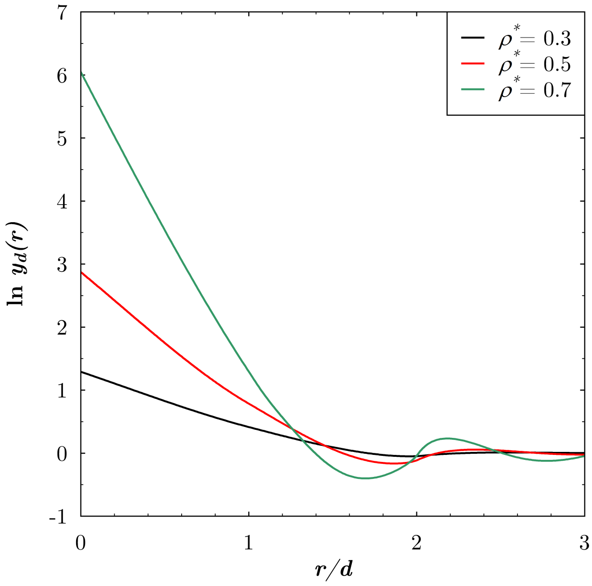

Figure 4.2: The HD cavity function, $\ln y_d(r)$ at various reduced densities ($\rho^* = \rho d^2$).

the equation of state, eqn.(4.11) with respect to η [41]

$$\begin{aligned} F_{ex} &= \int_0^\eta \frac{Z(\eta)-1}{\eta} d\eta, \\ &= \frac{\ln\left(1 - \frac{\eta(2\eta_0-1)}{\eta_0}\right)(2\eta_0 - 1) - \ln\left(1 - \frac{\eta}{\eta_0}\right)}{2(1-\eta_0)}. \end{aligned} \tag{4.16}$$

Eqns.(4.13) and (4.14) allow us to determine the coefficients a_0 and a_1 in eqn.(4.12) while the remaining coefficients a_2 and a_3 are determined by requiring that $y_d(r)$, $\partial y_d(r)/\partial r$ be continuous at $r = d$. Figure 4.2 shows the HD cavity function calculated in this way at a number reduced densities.

4.1.3 Predictor-Corrector algorithm

1. Given input structural data such as $g(r)$ or $S(q)$, we can extract a pair potential $u(r)$ from eqn.(4.4) via the iterative scheme described below. To obtain a first estimate of the HD diameter d, we use the well-known relationship between isothermal compressibility and $S(q = 0)$ [41]

   $$\frac{1}{S(q=0)} = \left[\frac{\partial \beta P}{\partial \rho}\right]_T, \tag{4.17}$$

   where $S(q = 0)$ is calculated from the input structural data (via eqn.(4.27)) whilst the right hand side is calculated from our chosen equation of state, eqn.(4.11). Using this value of d in eqn.(4.4) then provides us with the first estimate of $u(r)$.

2. In order to refine our estimate of d and ultimately $u(r)$, we require a procedure that correctly separates out the individual features of the potential that determine the coarse-grain and the fine-grain structures of the fluid. For this, we appeal to *Perturbation Theory*, which shows that the core of the potential and the effective density of the fluid determine the coarser features of the structure while the tail of the potential determines all the other features of the structure [41]. This particular theory appeals to our assumption of using HD correlation functions. With this in mind, we refine our estimate of d by splitting the potential into a core part $u_1(r)$ and a perturbative part $u_2(r)$ using the so-called *Barker-Henderson* (BH) criteria [66]

   $$u(r) = u_1(r) + u_2(r), \tag{4.18}$$

where

$$\begin{aligned} u_1(r) &= \begin{cases} u(r) & r < r_0, \\ 0 & r > r_0, \end{cases} \\ u_2(r) &= \begin{cases} 0 & r < r_0, \\ u(r) & r > r_0, \end{cases} \end{aligned}$$

where r_0 is the smallest value of r for which the potential is zero. The BH separation for a typical Lennard-Jones potential is illustrated in figure 4.3.

3. The core part of the potential is then used to obtain an improved estimate for d via the thermodynamic consistency condition [47]

$$\int_0^{\infty} \frac{\partial y_d(r)}{\partial d} \left[e^{-\beta u_1(r)} - e^{-\beta u_d(r)} \right] 2\pi r dr = 0, \qquad (4.19)$$

which serves as our *Corrector* equation. Eqn.(4.19) is derived by requiring that the free energy of the system of interest be minimum with respect to variations in $y_d(r)$ [41].

This new value of d is then used in eqn.(4.4) to improve our prediction of $u(r)$ and the procedure is repeated until d and $u(r)$ converge.

Note that $u(r)$ can be separated into core and perturbative parts using other criterion. For example, Rajagopalan and Rao use the *Weeks-Chandler-Andersen* (WCA) criterion [67] where the potential is separated at the first potential minima r_m. The WCA separation for a typical Lennard-Jones potential is also illustrated in figure 4.3. We have also used this separation and find that it yields essentially the same results as the BH separation at low densities. However at high densities

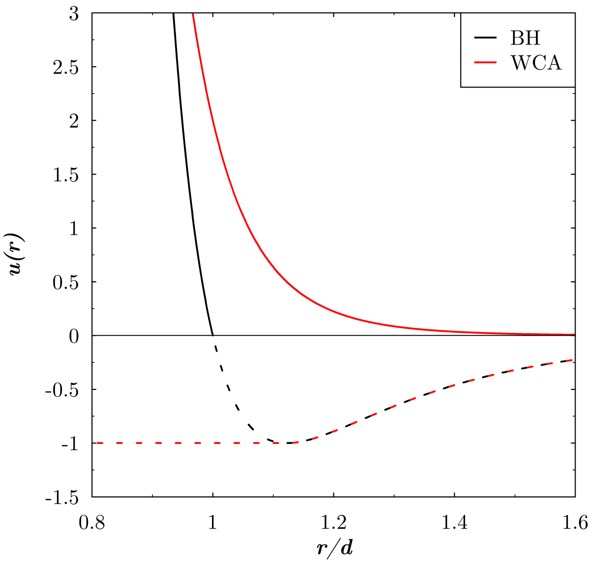

Figure 4.3: Comparison between the Barker-Henderson (BH) and the Weeks-Chandler-Andersen (WCA) separations for a typical Lennard-Jones potential. The full curves illustrate the core, reference potential whilst the dashes show the perturbation

(where the area fraction of the reference HD fluid approaches the closed packed area fraction for HD, η_0), we find that using the BH separation leads to more stable numerics compared to the WCA separation because the WCA separation leads to larger values of d.

4.2 HMSA method

We now turn our attention to the second method that we have developed that can be used to obtain $u(r)$ from $g(r)$ of a 2D system which is based on thermodynamically consistent closure relations. We introduced in section 3.4.2 the most well known of these, namely the Rogers-Young (RY) closure [53] that interpolates between the HNC and PY closures. The crossover from PY to HNC is governed by a switching function containing a single parameter that is determined by imposing thermodynamic consistency. This ‘mixed’ closure relation leads to very accurate results for the radial distribution function and thermodynamic properties in the case of purely repulsive potentials but breaks down for potentials containing an attractive well as thermodynamic consistency is no longer possible in this case [50]. To overcome this problem, Zerah and Hansen [50] have proposed an alternative mixed closure relation known as the HMSA closure that interpolates between the HNC and the SMSA closures. The resultant mixed closure is found to be applicable to both repulsive and attractive potentials. Zerah and Hansen have also used the HMSA closure to invert structural data from a 3D system interacting via the Lennard-Jones potential and achieved reasonable success [50].

We begin the description of our HMSA based 2D inversion method by providing details of the HMSA closure itself, followed by a description of the algorithm for obtaining $u(r)$.

4.2.1 HMSA closure

Similar to the HDPC method, the HMSA closure requires the pair potential to be separated into two parts. Therefore we first separate the total interaction potential $u(r)$ in a similar manner to the BH criteria but in this instance we separate the potential at the potential energy minimum, *i.e.* using the

Weeks-Chandler-Andersen (WCA) separation [67]

$$
\begin{aligned}
u_1(r) &= \begin{cases} u(r) - u(r_m) & r \leq r_m, \\ 0 & r \geq r_m, \end{cases} \\
u_2(r) &= \begin{cases} u(r_m) & r \leq r_m, \\ u(r) & r \geq r_m, \end{cases}
\end{aligned}
$$

where r_m is the position of the primary potential minima *i.e.*, the potential minima with the smallest r (see figure 4.3). The use of the WCA separation as opposed to the BH separation here increases the effectiveness of the SMSA closure, which has been shown to give very good results in extracting thermodynamic properties when the potential is divided at the minimum, rather than $u(r) = 0$ [41]. In terms of $u_1(r)$ and $u_2(r)$, the HMSA closure is given by

$$g(r) = \exp[-\beta u_1(r)] \left[1 + \frac{\exp[f(r)(\gamma(r) - \beta u_2(r)] - 1}{f(r)} \right], \qquad \text{(HMSA)} \quad (4.20)$$

where

$$\gamma(r) = h(r) - c(r), \tag{4.21}$$

which is called the *'indirect'* correlation function, and is illustrated in figure 4.4.

Here $f(r)$ is the switching function introduced in section 3.4.2 and is given by

$$f(r) = 1 - \exp\left(-\alpha r\right), \tag{4.22}$$

where $\alpha \in \{0, \infty\}$. The HMSA closure contains the same single fitting parameter like the RY closure, α in $f(r)$ that is varied until thermodynamic consistency is achieved. The HMSA closure, eqn.(4.20), has the very useful property that

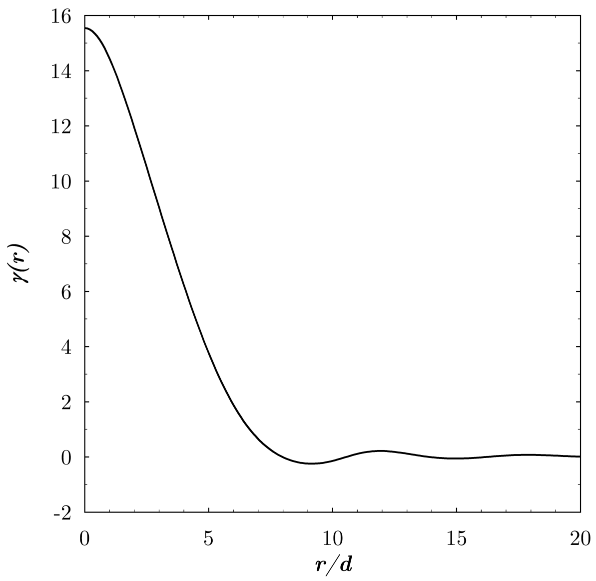

Figure 4.4: Example plot of $\gamma(r) = h(r) - c(r)$, the 'indirect' correlation function, for a fluid colloid system interacting via an exponential decay potential ($u(r) \propto \exp(-r/d)$) at a reduced density $\rho^* = \rho d^2 = 0.015$.

it reduces to the RY closure [53] for purely repulsive potentials (*i.e.* $u_2 = 0$ or $r_m = \infty$), making it essentially 'universal' for inverting all types of interaction potential.

4.2.2 HMSA inversion algorithm

Having defined the HMSA closure, the inversion scheme based on this closure now proceeds as follows.

1. The input data for the scheme is once again the radial distribution function, $g(r)$ (or the structure factor $S(q)$), and the corresponding number density ρ of the given system. In addition, we also need the correlation functions $c(r)$, $h(r)$ and hence $\gamma(r)$ which are readily obtained from the input $g(r)$ using the OZ relation (eqn.(4.1)). Note that two parameters are required in

order to calculate a pair potential using the HMSA closure from $g(r)$: The first being r_m, the cut-off radius used to refine the potential and the second being α, the fitting parameter in the switching function.

2. We use $\alpha = 0.1$ as the initial guess for all the potentials studied. Eqn.(4.20) with the initial guess for α then provides the first estimation of $u(r)$. Specifically, for the region $r \geq r_m$, $u_2(r)$ is given by eqn.(4.20) in conjunction with the WCA criteria

$$\beta u_2(r) = -\hat{C}(r) \equiv -\left[c(r) + \frac{\ln\left[1 + f(r)h(r)\right] - f(r)h(r)}{f(r)}\right]. \tag{4.23}$$

   Minimising $u_2(r)$ with respect to r enables us to determine r_m, the position of the primary minima of the potential.

3. Having obtained r_m, for $r \leq r_m$, we can now extract the core region of the potential, $u_1(r)$ using eqn.(4.20) again with the WCA criterion

$$\beta u_1(r) = \ln\left[\frac{\hat{g}(r)}{g(r)}\right] - \hat{C}(r_m), \tag{4.24}$$

   where

$$\hat{g}(r) = \frac{\exp\left[f(r)\left(\gamma(r) + \hat{C}(r_m)\right)\right] + f(r) - 1}{f(r)}. \tag{4.25}$$

   Note that in eqns.(4.23)-(4.25), we use $h(r)$, $\gamma(r)$ and $c(r)$ calculated from the *input* $g(r)$ data; this is important when enforcing thermodynamic consistency later. It is important to note also that eqns.(4.23)-(4.25) correct for the typographical errors in the corresponding equations in the original Zerah and Hansen paper [50].

4. Finally, the total potential is given simply by

$$\beta u(r) = \beta u_1(r) + \beta u_2(r). \tag{4.26}$$

5. An improved value of α is obtained by imposing thermodynamic consistency. Specifically, we opt for the compressibility route where we require the isothermal compressibility calculated from the well-known compressibility equation eqn.(4.10) [41]

$$\frac{\partial \beta P}{\partial \rho} = \frac{1}{S(q=0)} = \left[1 + 2\pi\rho \int_0^\infty h(r) r dr\right]^{-1}, \tag{4.27}$$

   to be equal to that calculated from the 2D virial equation [44]

$$\frac{\beta P}{\rho} = 1 - \frac{\pi\rho}{2} \int_0^\infty r^2 dr g(r) \frac{d\beta u(r)}{dr}. \tag{4.28}$$

6. In order to calculate $\partial\beta P/\partial\rho$ via eqn.(4.27), we use the input $h(r)$ on the right hand side of eqn.(4.27). In order to calculate $\partial\beta P/\partial\rho$ via eqn.(4.28), we differentiate eqn.(4.28) with respect to ρ

$$\frac{\partial \beta P}{\partial \rho} = 1 - \pi\rho \int_0^\infty r^2 dr g(r) \frac{d\beta u(r)}{dr} - \frac{\pi\rho^2}{2} \int_0^\infty dr \frac{\partial g(r)}{\partial \rho} r^2 \frac{d\beta u(r)}{dr}. \tag{4.29}$$

   The function $\partial g(r)/\partial\rho$ in eqn.(4.29) is then calculated by differentiating

$g(r)$ from eqn.(4.20) with respect to ρ to give

$$\frac{\partial g(r)}{\partial \rho} = \begin{cases} w(r)\exp[f(r)\,(\gamma(r)-\beta u(r_m))]\frac{\partial \gamma(r)}{\partial \rho}; & r \le r_m, \\ \exp[f(r)\,(\gamma(r)-\beta u(r))]\frac{\partial \gamma(r)}{\partial \rho}; & r \ge r_m, \end{cases} \tag{4.30}$$

where $w(r) = \exp(-\beta u(r) + \beta u(r_m))$.

7. We now need to obtain $\partial\gamma(r)/\partial\rho$ in order to use eqn.(4.30), which can be readily obtained from the OZ relationship (eqn.(4.1)) and the HMSA closure (eqn.(4.20)). On the whole, we have found that it is numerically more stable to work in terms of $c(r)$ and $\gamma(r)$, rather than $c(r)$ and $h(r)$. The latter two distribution functions appear more susceptible to numerical instabilities, probably due to the strong oscillations of $h(r)$ at low r. Therefore, we rewrite eqns.(4.1) and (4.20) in terms of $c(r)$ and $\gamma(r)$ and from differentiating, we obtain

$$\frac{\partial \gamma(q)}{\partial \rho} = \frac{c(q)^2}{(1-\rho c(q))^2} + \frac{2\rho c(q) - \rho^2 c(q)^2}{(1-\rho c(q))^2}\frac{\partial c(q)}{\partial \rho}, \tag{4.31}$$

and

$$\frac{\partial c(r)}{\partial \rho} = \begin{cases} \frac{\partial \gamma(r)}{\partial \rho}\left(w(r)\exp[f(r)(\gamma(r)-\beta u(r_m))]-1\right); & r \le r_m, \\ \frac{\partial \gamma(r)}{\partial \rho}\left(\exp[f(r)(\gamma(r)-\beta u(r))]-1\right); & r \ge r_m. \end{cases} \tag{4.32}$$

Note that in eqns.(4.29)-(4.32) we have implicitly assumed that thermodynamic consistency is *local*, *i.e.* that α (and hence $f(r)$) and $u(r)$ are constant with respect to any changes in the density. The assumption that α is constant with respect to ρ is in general an excellent approximation since α is always found to be a slowly varying function of density [50]. Also note that in eqns.(4.31) and (4.32), we use the initial guess for α to calculate $f(r)$ (eqn.(4.22) and the initial guess for $u(r)$ calculated from eqns.(4.23)-(4.26).

8. We can now calculate $\partial\gamma(r)/\partial\rho$ by iterating between (4.31) and (4.32) using a simple Picard scheme until convergence is obtained. For the initial guess of $\partial\gamma(q)/\partial\rho$, we use the first term on the right hand side of eqn.(4.31) only. The number of iterations required is approximately 200. This part of the scheme could be speeded up by employing the Gillan Newton-Raphson based method [68] but we have found that the simpler Picard method is fast enough using modern day processing power.

9. To complete our calculation of $\partial\beta P/\partial\rho$ via eqn.(4.29), for $g(r)$ in the second term of the right hand side of eqn.(4.29), we insert the HMSA expression given by eqn.(4.20) with the value of α undetermined. An improved value of α is obtained by varying this α until the $\partial\beta P/\partial\rho$ calculated from eqn.(4.27) agrees with $\partial\beta P/\partial\rho$ calculated from eqn.(4.29). This new value of α is now used to improve our estimate for $u(r)$ and the procedure is repeated until α and $u(r)$ converge, so that thermodynamic consistency is enforced. Typically convergence of α to within 0.5% was achieved after about five iterations.

In order to avoid singularities in $u(r)$ at $r = 0$, it is in fact numerically more convenient to work in terms of $w(r) = \exp(-\beta u(r) + \beta u(r_m))$ instead of directly with $\beta u(r)$ for the region $r \leq r_m$. The relevant equations (*i.e.* eqns.(4.24),(4.29)) in terms of $w(r)$ rather than $u(r)$ are given in Appendix B.

4.3 Summary

In this chapter we have derived using Integral Equation Theory, two new methods for extracting the effective pair potential $u(r)$ from $g(r)$ (or $S(q)$) data, the first is the *Hard-Disk Predictor-Corrector* (HDPC) method, and second the *HMSA* method which is based on the HMSA closure. Both methods require the use of the Ornstein-Zernike equation and the determination of a number of relevant correlation functions, such as the total correction function $h(r)$ and the direct correlation function $c(r)$. The HDPC method is an extension of the 3D scheme of Rajagopalan and Rao [37] to 2D, using hard-disk fluids as the reference state. Specifically the undetermined bridge function $B(r)$ is replaced with the hard-disk bridge function $B_d(r)$ which requires that the unknown hard-disk diameter d is determined through an iterative scheme. To this end, we have derived convenient forms for the necessary pair-correlation functions for the reference hard-disk fluid, including the cavity function $y_d(r)$.

The second method involves mixing two integral equations, namely the Hypernetted-Chain closure and soft core Mean Spherical Approximation, assuming that the solution for the pair potential lies in-between these two solutions, forming what is known as the HMSA closure relation (as proposed by Zerah and Hansen [50]). In our implementation of the scheme, the unknown fitting parameter α in the HMSA closure is determined by requiring thermodynamic consistency between the virial and compressibility equations of state, and iterated until we obtain convergence in the unknown fitting parameter.

For the two methods presented here, we plan to implement the algorithms described in sections 4.1.3 and 4.2.2 on simulation data interacting via a wide range of interaction potentials in chapter 5, as well as using the routines to analyse real experimental data in chapter 6.

Chapter 5

Inversion of $g(r)$ obtained from simulations

In this chapter, we will compare the accuracy of our HDPC and HMSA routines that were presented in chapter 4, on $g(r)$ data obtained from simulations. As we pointed out in chapter 3, the use of simulation data has at least two advantages: Firstly, it allows one to generate very accurate $g(r)$ data by performing long simulation runs and averaging over many snapshots. Secondly, using MC simulations means that we know the underlying potential *a priori*, thus allowing one to directly assess the accuracy of the inversion scheme. We aim to systematically increase the level of noise in $g(r)$ data generated from our MC simulations. This will allow us to quantitatively assess how noise levels in the input $g(r)$ affect the final accuracy of the inversion. We also look to test our two inversion methods against the conventional OS routines, HNC and PY for the systems studied.

We begin this chapter by providing details and the rationale behind the use of the selected test potentials that will feature in our MC simulations, as well as all technical details of our MC simulations. We then present inversion results using the HDPC and HMSA methods compared to HNC and PY methods on $g(r)$ data obtained from MC simulations. We will also test the effect of density and noise on the accuracy of the different schemes in an attempt to mimic common problems encountered with experimental data.

5.1 MC simulation details

5.1.1 Test pair potentials

We now present a number of pair potentials that will be used in our MC simulations in order to benchmark our inversion techniques against the conventional OS routines. Specifically we consider the following four classes of potentials:

1. **Exponential decay potentials**: Quesada-Pérez *et al.* [35] studied systems using soft pair potentials, with and without attractive wells through the inversion of simulation and experimental $g(r)$ data using the HNC closure. Soft interaction potentials at relatively high monolayer densities are often encountered in colloidal systems. In particular this type of interaction featuring a repulsive core that is of long range has found to exist for an assembly latex beads at an air/water interface [35]. Following Quesada-Pérez *et al.* [35], for a soft repulsive interaction we use the

exponential decay potential

$$\beta u(r) = 200\exp(-0.65r/\sigma), \tag{5.1}$$

while for the soft interaction with an attractive well we use the potential

$$\beta u(r) = 200\exp(-0.65r/\sigma) + 10\exp(-0.15r/\sigma)\cos(0.3r/\sigma), \tag{5.2}$$

where σ controls the range of interaction. Note that the repulsive core is the same for both eqns.(5.1) and (5.2).

2. **Stillinger-Hurd potential**: In chapter 2, we presented the expressions introduced by Stillinger [9] and Hurd [10] for the electrostatic dipole-dipole interaction between two colloid particles at an air/water interface. Following Stillinger and Hurd, for a colloid diameter of σ, we use the following potential,

$$u(r) = \begin{cases} \infty & r < \sigma; \\ \dfrac{\xi}{\varepsilon(\kappa r)^3} + \dfrac{\xi}{\kappa r}\dfrac{\varepsilon^2}{\varepsilon^2 - 1}\exp[-\kappa r] & r \geq \sigma, \end{cases} \tag{5.3}$$

where $\xi = 2z^2e^2\kappa/4\pi\varepsilon\varepsilon_0$, z is the total charge of the colloid particle, e is the elementary charge, ϵ is the relative dielectric constant, ε_0 is the dielectric constant of a vacuum and κ^{-1} is the Debye screening length. Following Terao *et al.* [12], we use the following parameter values: $\beta\xi = 1/5.621 \times 10^{-4}$, $\epsilon = 80$ and $\kappa^{-1} = 200$nm.

3. **Lennard-Jones (LJ) potential**: The LJ pair potential for particles in dense media consists of two 'parts'; a steep repulsive term that describes a Pauli repulsion at short ranges due to overlapping electron orbitals, and a smoother attractive term representing the London dispersion forces [69] (see section 2.1.2). Even though the LJ interaction is not strictly a potential that characterises colloids at the interface, the inclusion of a steep repulsive core and an attractive component for micrometre sized particles does provide a suitable and feasible mechanism for the type of systems we are interested in. The LJ potential can be formally parametrised as

$$\beta u(r) = 4\beta\xi \left[\left(\frac{\sigma}{r}\right)^{12} - \left(\frac{\sigma}{r}\right)^{6} \right], \tag{5.4}$$

   where ξ and σ are respectively the fundamental energy and length scale of the potential with $\beta\xi = 1/1.25$.

4. **DLVO potential**: First introduced by Derjaguin and Landau in 1941 [70], and later modified in 1948 by Verwey and Overbeek [71], DLVO theory is used to describe the interactions between charged colloids in an electrolyte. The specific form we shall use is the same as that given by Rajagopalan [36]

$$\beta u(r) = \beta u_A + \beta u_E + \beta u_B, \tag{5.5}$$

   where u_L is the strong London-van der Waals attraction term, u_E the weak electrostatic repulsion term and u_B a steep Born-type, hard-core repulsion term. Specifically assuming a colloid diameter of unity,

$$\beta u_L(r) = -N_L \left\{ \frac{1}{2r^2} + \frac{1}{2(r^2-1)} + \ln\left[\frac{r^2-1}{r^2}\right] \right\}, \tag{5.6}$$

where $N_L = \beta A_H/6$ with A_H being the Hamaker constant,

$$\beta u_E(r) = N_E \frac{\exp\left[-\kappa R(r-1)\right]}{r}, \tag{5.7}$$

where R is the radius of the particles ($= 0.5$ in our dimensionless units) and N_E is a pre-factor related to the contact potential,

$$\beta u_B(r) = N_B \left(r-1\right)^{-12}, \tag{5.8}$$

with N_B being the Born parameter that appropriately scales the interaction. The numerical values that have been chosen for the dimensionless parameters are $N_A = 0.7$, $N_E = 3.5$, $N_B = 2.275 \times 10^{-18}$ and $\kappa R = 10$. The DLVO potential has been very successful in determining the properties of colloids in the bulk *i.e.*, 3D systems. Like the LJ potential, it is not strictly an interaction encountered at the interface, but the complicated nature of the potential will be a stringent test for the inversion schemes we shall be using (see figure 5.4).

* * *

There are a number of reasons for choosing these potentials: In addition to the fact that they are representative of the broad spectrum of interaction potentials found in 2D colloidal systems, they also contain additional attributes that allow us to test the inversion scheme rigorously. For example, the exponential decay potential and the Stillinger-Hurd potential are purely repulsive and have a soft core. On the other hand, the exponential potential with oscillatory tail and the LJ potential have an attractive well, with the latter having a harsh repulsion. Finally the DLVO potential is a very complex potential which includes a hard-core, an intermediate range attractive well, a longer range repulsive barrier and finally a soft tail (see figure 5.4) and therefore serves as a very stringent test for the inversion schemes.

5.1.2 Other simulation details

We can use either $g(r)$ or $S(q)$ as the input data for our inversion scheme. Most experimental structural studies on 2D colloidal monolayers report results for $g(r)$ and in this chapter, we therefore focus on $g(r)$ as the input data. The source data for the potentials listed above in section 5.1.1 will be generated using MC simulations in the canonical ensemble using periodic boundary conditions and the minimum image convention (see section 3.6.1). Simulations are performed with particle numbers ranging from 1024 to 2025 to confirm that finite size effects are negligible. An acceptance ratio of 50% of trial moves in the MC scheme by the self adjustment of the particle displacements was enforced throughout all simulations.

For all systems studied, we aim to choose densities high enough to exhibit several peaks in the $g(r)$ data but low enough to ensure that the correlation length remains smaller than the simulation box size. Most of the densities in this chapter are chosen to be low enough so that the first maximum in $g(r)$ was lower than 3, which is the value above which 2D fluids generally undergo an ordering transition to either a hexatic or crystalline phase [12, 72]. The specific densities used for each system are given below. Later in this chapter when we consider the effect of density on the accuracy of the different inversion schemes, we will also consider higher densities close to ordering transitions for the monolayer.

For all our simulations, 60,000 MC steps per particle were used for the equilibration phase while 100,000 MC steps per particle were used for the analysis phase. For most of the simulation based inversions in this chapter, $g(r)$ curves are obtained by averaging over 10,000 snapshots from the latter phase of the simulation (*i.e.* 1 snapshot for every 10 MC steps per particle to ensure the snapshots are independent) in order to minimise noise. However, later in this chapter where we consider the effect of noise in the input $g(r)$ data on the accuracy of the inverted potentials, we will make use of $g(r)$ data obtained from 1 snapshot only, to mimic experimentally realistic levels of noise in the input $g(r)$ data. In calculating $g(r)$, we follow the algorithm presented in section 3.6.4. Radial bin sizes of order 50nm were used (assuming colloid diameters to be of order $\approx 1\mu$m); this level of resolution, though challenging, should be accessible experimentally. All Fourier transforms of the various correlation functions were performed using the method outlined by Lado [63], where we have always used at least a frequency of 1000 Fourier modes throughout the calculations to maintain high quality Fourier transforms.

5.2 Accuracy of HDPC and HMSA compared to one-step methods

We first discuss results for the exponential decay potentials (eqns.(5.1)-(5.2)). Note that while the exponential decay potential is purely repulsive, the exponential decay with oscillatory tail has a primary minima around $r/\sigma = 10$ (see figure 5.1). In both cases, a density of $\rho\sigma^2 = \rho^* = 0.015$ was used, the same as used by Quesada-Pérez *et al.* [35]. Note our HDPC method could not be used in this case because it was numerically unstable at this density as the area fraction of the reference HD fluid was too close to close packing density. However no such limitation was found for the HMSA scheme. This indicates that the HMSA scheme is more suitable for soft potentials compared to the HDPC method because densities approaching the close packing density of the reference HD fluid are often encountered in these systems. This point will be discussed in more detail in the subsection 5.3.

The inversion of the purely repulsive, exponential decay potential by HMSA, HNC and PY schemes is shown in figure 5.1(a). The fitting parameter α, in the HMSA scheme converges to a value of $\alpha = 0.130$. Clearly the HMSA scheme leads to a very accurate inversion of the potential and is much more accurate compared to either the HNC or PY. In fact, strictly speaking HMSA predicts a very shallow minima at $r_m = 28.462$ with a depth $\beta u(r_m) = -0.016$. However since the magnitude of this minima is negligible compared to k_BT, the inverted potential is effectively purely repulsive.

In figure 5.1(b), we show that the inversion by all three schemes of the exponential decay potential with an oscillatory tail where the fitting parameter

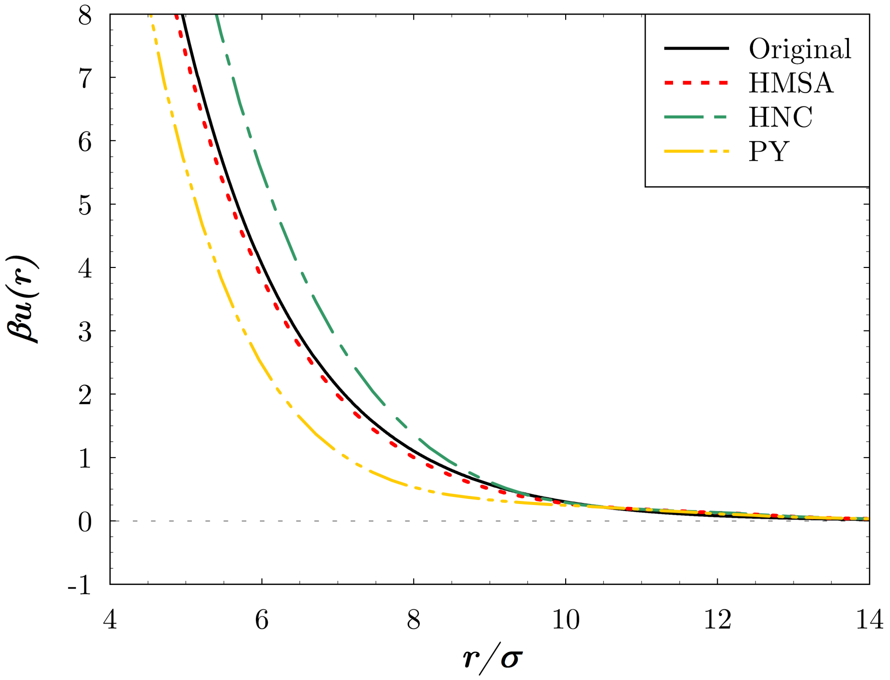

(a) Inversion of exponential decay potential.

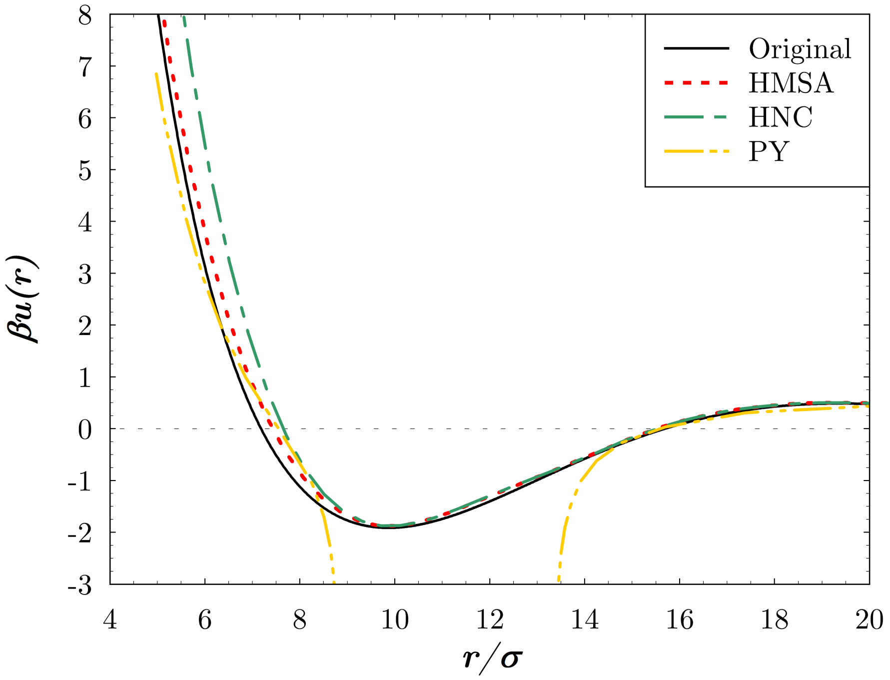

(b) Inversion of exponential decay with oscillatory tail potential.

Figure 5.1: Inversion results for the HMSA, HNC and PY closures for both exponential decay potentials, *i.e.* eqns.(5.1) and (5.2). Both potentials were conducted at a reduced density $\rho^* = \rho\sigma^2 = 0.015$.

α, in the HMSA scheme converges to a value of $\alpha = 0.161$. The HMSA scheme again yields very accurate results as well, reproducing all the features, especially the primary minima and oscillatory tail though it slightly overestimating the soft core. In terms of the OS methods, HNC overestimates the soft core to a much larger degree compared to HMSA, though it reproduces the primary minima and oscillatory tail well. In contrast, the inversion by PY is very poor for this potential, breaking down altogether generating non-physical values between $8 < r/\sigma < 13$. Thus for potentials containing an attractive well, the potential is no longer bracketed by HNC and PY so it is not possible to use RY to invert the potential as thermodynamic consistency cannot be achieved in this case (see section 3.4.2). In contrast the HMSA scheme is able to faithfully invert both repulsive potentials and potentials containing an attractive well.

Next we examine the Stillinger-Hurd potential, which is a more realistic potential for colloids at a polar/non-polar liquid interface. A reduced density $\rho^* = \rho\pi\sigma^2/4 = 0.005$ was used. The inversion results are shown in figure 5.2. Unlike the previous potentials, the HDPC scheme is numerically stable at this density. The HDPC scheme converged value of d corresponds to an area fraction $\eta = \rho\pi d^2/4 = 0.373$ for the reference HD fluid. The HDPC scheme leads to a very accurate inversion of the potential, and is much more accurate compared to either HNC or PY. We note that as for the purely repulsive exponential decay potential, the actual potential is once again bracketed by HNC (upper bound) and PY (lower bound).

The HMSA scheme converges to a value of $\alpha = 0.170$. Once again, the HMSA scheme leads to a very accurate inversion of the potential, and is much more accurate compared to either the HNC or PY, and comparable to the HDPC

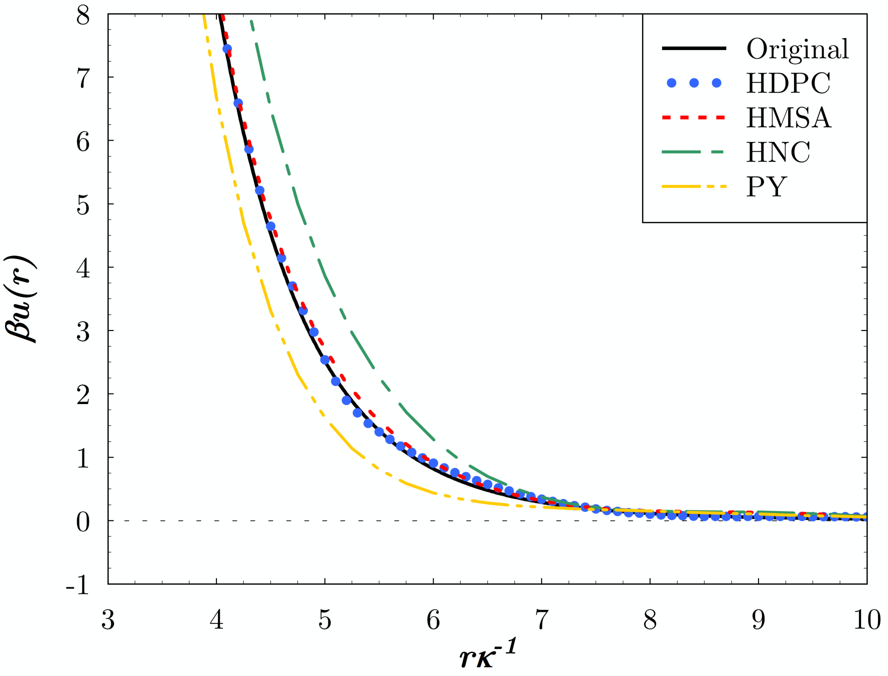

Figure 5.2: Inversion results for screened coulomb and dipole potential with a hard-core, *i.e.* eqn.(5.3) at an area fraction $\eta = 0.005$.

scheme.

The third potential we test is the LJ potential and the inversion results are shown in figure 5.3. A reduced density of $\rho^* = \rho\sigma^2 = 0.5$ was used for the monolayer. For the HDPC scheme, the converged value of d corresponds to $\eta = \rho\pi d^2/4 = 0.366$ for the reference HD fluid. We see that the HDPC scheme reproduces the potential reasonably accurately, though it slightly overestimates the well depth. For the HMSA scheme, α converged to a value of $\alpha = 0.898$. We see that the HMSA scheme reproduces the core and long-range tail accurately, although it also overestimates the attractive well depth slightly. In terms of the OS methods, HNC is superior to PY as it reproduces both the repulsive core and long-range tail accurately but predicts a well depth that is too shallow; in

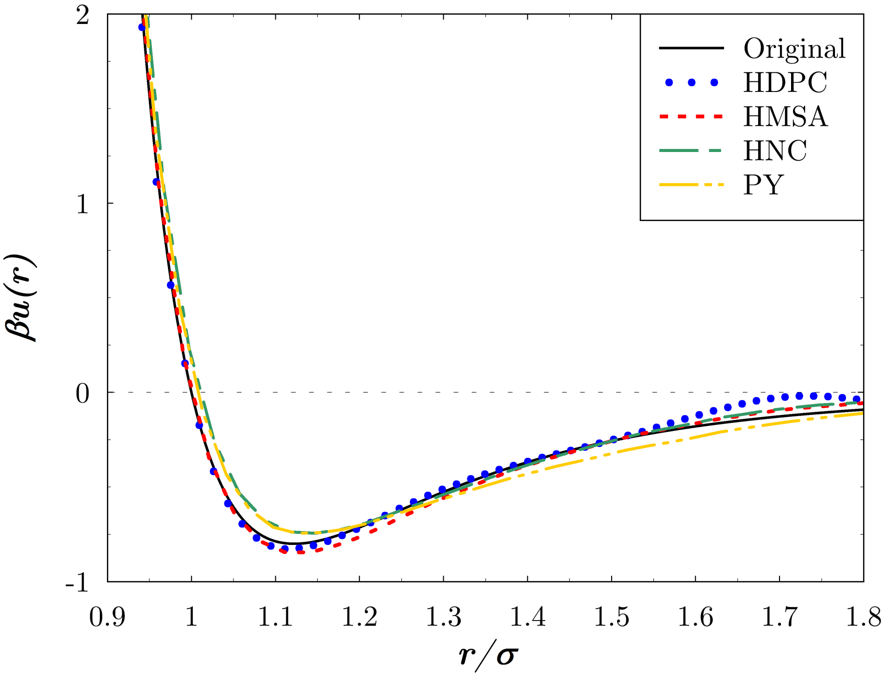

Figure 5.3: Inversion results for LJ potential, *i.e.* eqn.(5.4) at a reduced density of $\rho^* = 0.5$.

contrast the accuracy of PY is relatively poor over the entire range of r except near the steep repulsive core. However both the accuracy of the HDPC and HMSA schemes are at least as good as the best OS method, which in this case is HNC, especially in modelling the attractive well.

The final potential we shall consider is the DLVO potential. The resultant $g(r)$ for this potential is shown in figure 5.4(a): Note that this interaction potential required a higher number of Fourier modes for the inversion (approximately 2000 modes) because the sharp peak in the input $g(r)$ data required higher resolution. As shown in figure 5.4(b), this potential is very complicated as it includes a short range hard-core repulsion, an intermediate range attractive well, a longer range repulsion and finally a soft tail and therefore serves as a very stringent

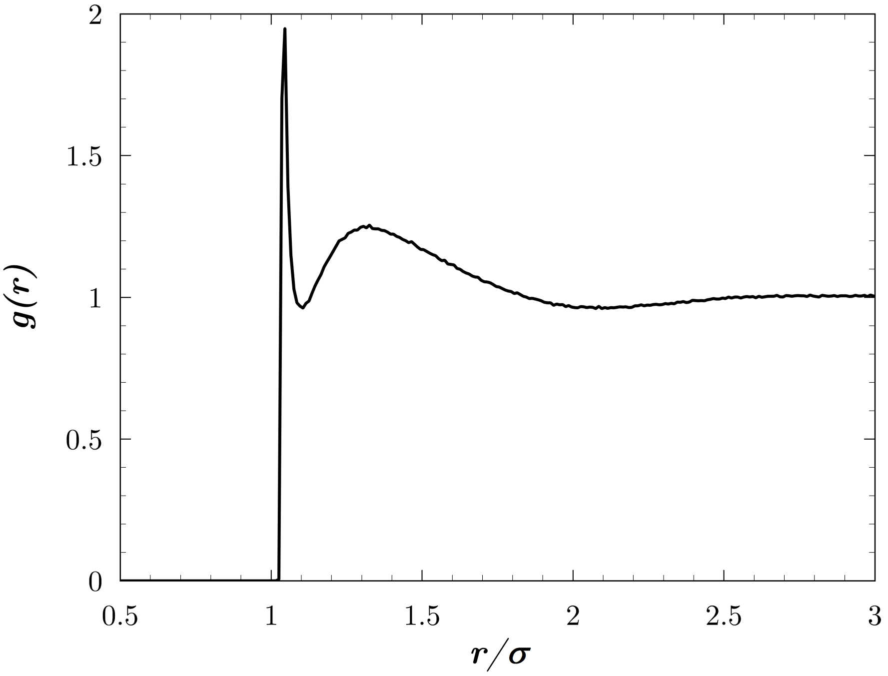

(a) Source $g(r)$ data for DLVO potential.

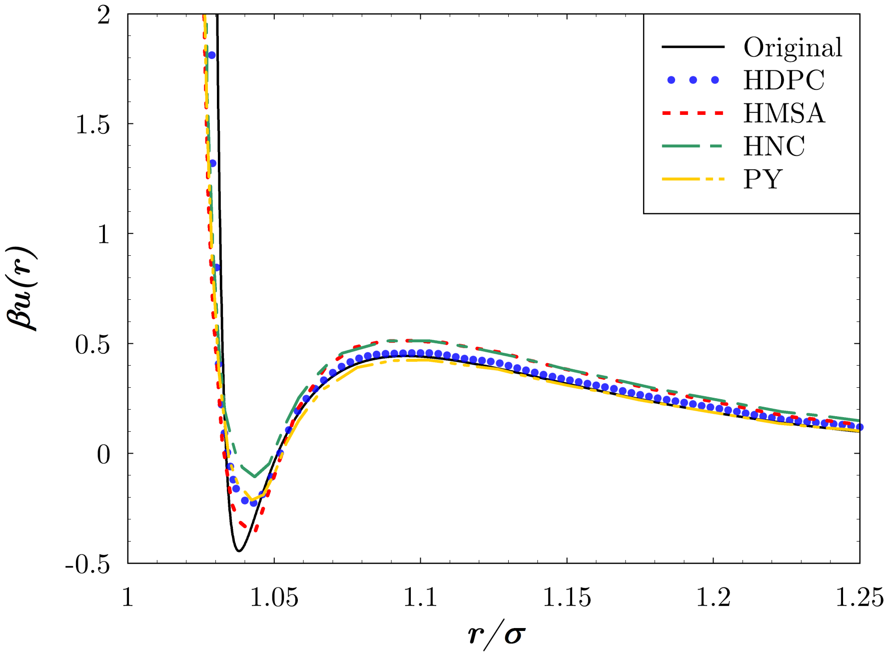

(b) Inversion of DLVO potential.

Figure 5.4: Inversion results for DLVO potential, *i.e.* eqns.(5.5)-(5.8), conducted for a reduced density $\rho^* = 0.2$.

test for any inversion scheme. The inversion was conducted for a reduced density $\rho^* = \rho\pi\sigma^2/4 = 0.2$ and the results are shown in figure 5.4(b). For the HDPC scheme, the converged value of d corresponds to $\eta = \rho\pi d^2/4 = 0.211$ for the reference HD fluid, and for the HMSA scheme, the converged value of α was $\alpha = 0.014$. We see that the accuracy of the HDPC scheme is comparable to that of HMSA and PY and the HDPC, HMSA and PY are significantly better than the HNC scheme for this potential. Specifically both the HDPC and HMSA reproduce the hard-core repulsion, the repulsive barrier and the soft tail very accurately, though they underestimate the depth of the attractive well. We see that the HMSA scheme is the best method for predicting the well depth of the DLVO potential. Specifically, it predicts the short ranged hard-core Born repulsion and the long-range soft tail well, though it slightly underestimates attractive well depth and overestimates the repulsive barrier, and its prediction of the position of the primary minima is slightly too large.

For the OS routines, PY is more accurate compared to HNC, as it models the hard-core repulsive, long-range tail and primary attractive well more accurately. This is presumably due to the fact that PY is more accurate for short-range hard interactions compared to HNC and is therefore better adapted to the hard-core repulsion present in the DLVO potential. However PY predicts the attractive well depth less accurately compared to HDPC and HMSA, though it predicts the repulsive barrier more accurately compared to the HDPC and HMSA. Taken as a whole, the accuracy of the HDPC and HMSA schemes are therefore marginally better to that of PY for this potential.

Overall, we have shown that the relative accuracy of the HNC and PY schemes depend on the interaction potential, but the HDPC and HMSA routines always provide an inversion result that is at least as good as the most accurate OS method.

5.3 Effect of density on inversions

In the previous subsection, we performed inversions at one specific density for each of the potentials studied. In order to study how the relative performance of the different inversion schemes depends on density, in this subsection we compare the accuracy of the HMSA and the HDPC scheme with the HNC and PY schemes for a few representative potentials as we increase the density of the monolayer. We first consider the exponential decay potential without an oscillatory tail which has a soft-core. In figures 5.5(a), 5.5(b) and 5.5(c) we present inversion results for this potential at the reduced densities of $\rho^* = \rho\sigma^2 = 0.008, 0.01, 0.015$ respectively. We see that while HNC and PY yield reasonably accurate results at the lowest density, the accuracy of these schemes becomes progressively worse as we go to higher densities. On the other hand, both HMSA and HDPC yield very accurate inversion results for $\rho^* = 0.008, 0.01$ which are comparable to each other. However as noted in the previous subsection, the HDPC scheme breaks-down at $\rho^* = 0.015$ because at this density, the area fraction of the reference HD fluid ($\eta = 0.637$ as estimated from the compressibility equation eqn.(4.27)) is too close to the close packed area fraction of $\eta_0 = 0.9069$. In contrast, the HMSA scheme remains numerically stable at this density and still provides very accurate inversion results.

Next we consider the LJ potential which has a strong repulsion and an attractive well. In figures 5.6(a), 5.6(b) and 5.6(c) we present inversion results for the LJ potential at the reduced densities of $\rho^* = \rho\sigma^2 = 0.4, 0.6, 0.7$ respectively.

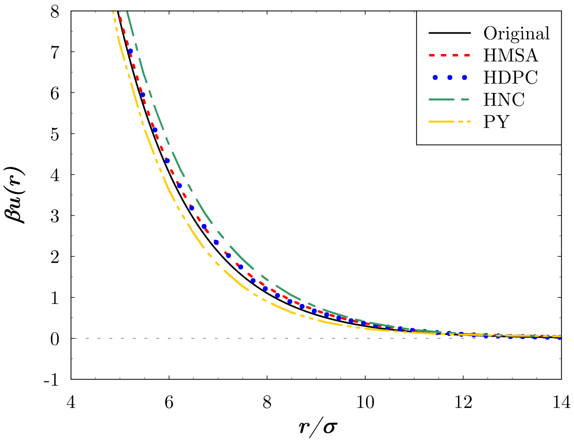

(a) $\rho^* = 0.008$

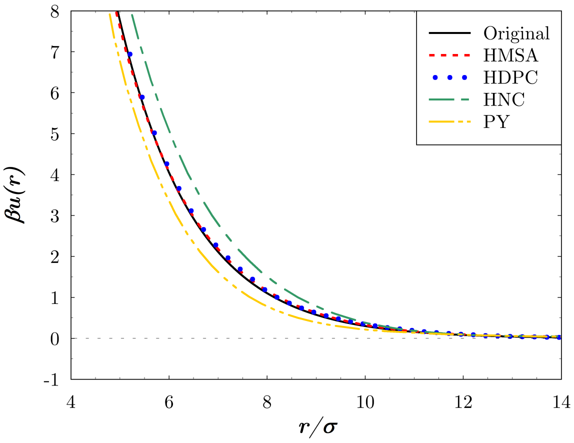

(b) $\rho^* = 0.01$

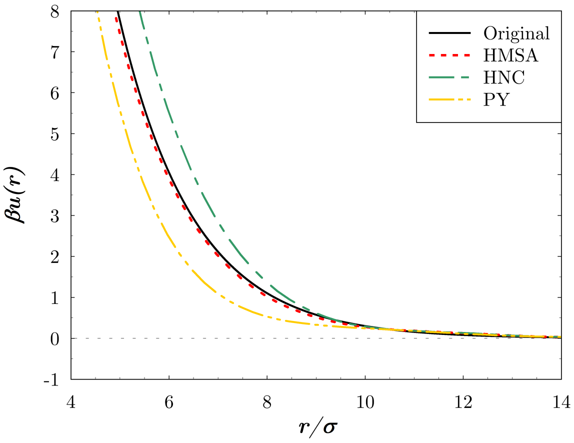

(c) $\rho^* = 0.015$

Figure 5.5: Results illustrating the effect of density on the inversion for exponential decay potential, *i.e.* eqn.(5.1) using all the considered inversion methods.

Just as for the case of the exponential decay potential, both HNC and PY yield accurate inversion results at the lowest density but become progressively worse as we go to higher densities. In contrast, the HDPC scheme yields accurate results for all the densities studied (though even this scheme becomes slightly less accurate at the highest density of $\rho^* = 0.7$). Interestingly, while the HMSA scheme yields accurate results for $\rho^* = 0.4, 0.6$ (comparable to HDPC), it performs much worse than HDPC for $\rho^* = 0.7$, though it is still marginally better than either HNC or PY.

The poor performance of HMSA at $\rho^* = 0.7$ is probably due to the fact that at this density, the LJ fluid is close to an ordering transition. This is evidenced by the fact that the height of the first maximum in $g(r)$ is about 2.7 which is close to the value of $3.3 - 3.4$ where the LJ fluid undergoes an ordering transition to either a hexatic or crystalline phase [72]. This is supported further by the fact that the LJ system in 2D appears to enter a metastable phase of solid-liquid coexistence at $\rho^* \approx 0.7$ when $T^* \approx 1/1.25$ [73]. Since HMSA is fundamentally an integral equation theory for the isotropic fluid state, it is not surprising that the theory breaks down close to an ordering transition. In contrast, for the exponential decay potential, the height of the first maximum in $g(r)$ is about 1.8 for the highest density studied. We therefore expect this system to be deep in the isotropic fluid state where the HMSA scheme is valid. Interestingly, the HDPC scheme yields accurate inversion results for all the densities studied for the LJ potential even though it is also based on integral equation theory. This suggests that the key approximation behind this scheme, *i.e.* that the actual bridge function is equal to the HD bridge function, remains accurate even close to an ordering transition. Note that unlike the exponential decay potential case,

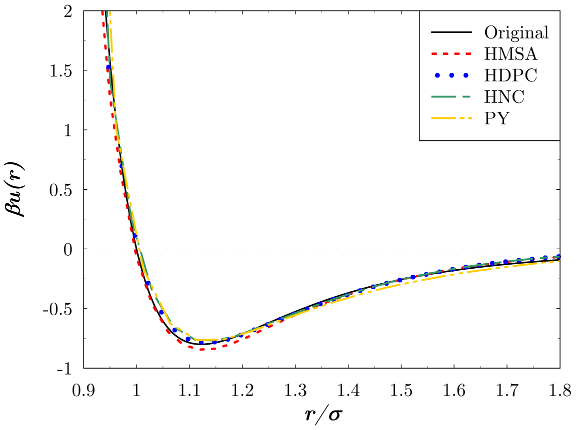

(a) $\rho^* = 0.4$

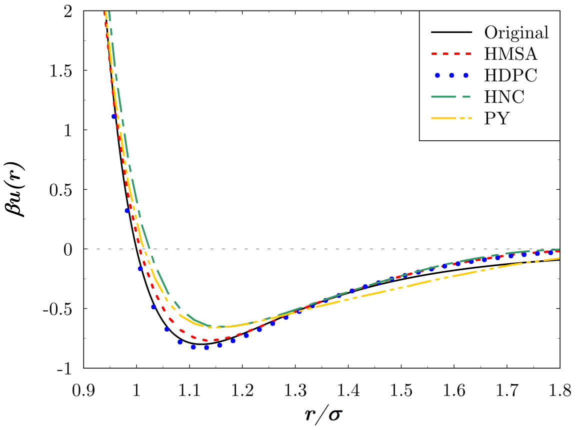

(b) $\rho^* = 0.6$

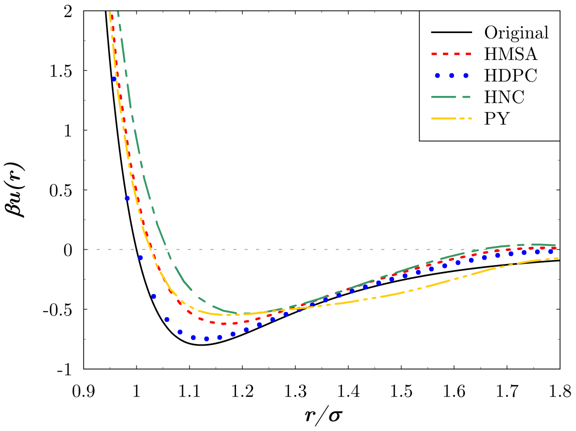

(c) $\rho^* = 0.7$

Figure 5.6: Results illustrating the effect of density on the inversion for LJ potential, *i.e.* eqn.(5.4).

the HDPC scheme remains numerically stable at the highest density studied for the LJ potential. This is because of the harsh repulsion the LJ potential possess at low r that drives long-range statistical ordering within the fluid. This means that even close to an ordering transition, the area fraction of the reference HD fluid can still be quite far from the close packing density. For example for $\rho^* = 0.7$ where the height of the first maximum in $g(r)$ is 2.7, the area fraction of the reference HD fluid is 0.605. In contrast for the exponential decay potential, for $\rho^* = 0.01$ where the height of the first maximum in $g(r)$ is 1.52, the area fraction of the reference HD fluid is 0.552, while for $\rho^* = 0.015$ where the height of the first maximum in $g(r)$ is 1.71, the area fraction of the reference HD fluid is 0.637.

Comparing our results for the exponential decay potentials and the LJ potential, we conclude that the accuracy of the HMSA and HDPC schemes are superior to HNC and PY, especially as we go to higher densities. For densities away from an ordering transition and the close packed density of the reference HD fluid, both HMSA and HDPC schemes yield very accurate inversion results which are comparable to each other. For densities close to an ordering transition (as evidenced by the height of the first maximum in $g(r)$ approaching the value of 3), the HDPC scheme is much more accurate compared to the HMSA scheme. The HDPC scheme is therefore better suited to studying hard-core monolayers (*e.g.*, monolayers interacting via the LJ potential) where there can be significant statistical ordering in the monolayer for relatively small area fractions of the corresponding reference HD fluid. However for densities close to the close packing density of the reference HD fluid, the HDPC scheme becomes unstable while the HMSA scheme remains numerically stable. The HMSA scheme is therefore better suited to studying soft-core monolayers (*e.g.*, monolayers interacting via the exponential potential) where significant ordering in the fluid only occurs for densities close to the close packing density of the reference fluid. The HMSA and HDPC schemes are therefore complementary to each other.

5.4 Effect of noise and truncation on accuracy of inversions

In the previous subsections, all inversions were performed on high quality $g(r)$ data obtained by averaging over a large number of snapshots (10,000) in MC simulations. However $g(r)$ data obtained from real experiments will obviously be significantly more noisy. In order to quantitatively assess how errors in the input $g(r)$ affect the final accuracy of the inversion, in the next subsection we use the HMSA and HDPC schemes to invert more noisy $g(r)$ data obtained from a single snapshot in our MC simulations. This procedure generates experimentally realistic levels of noise in the input $g(r)$ data. In addition to noise, $g(r)$ $(S(q))$ data obtained from experiments will in general be restricted in their r (q) range. We will therefore also consider how truncation in the r or q range affects the accuracy of the inversion.

We first consider the exponential decay potentials, with and without an oscillatory tail, where the monolayers in both cases are at a density of $\rho^* = 0.015$. Since the HDPC scheme is unstable at this density, we shall only consider inversions using the HMSA scheme for these potentials (we will consider the HDPC scheme later for the LJ potential). The advantage of considering these two potentials is that they have the same soft core but different intermediate

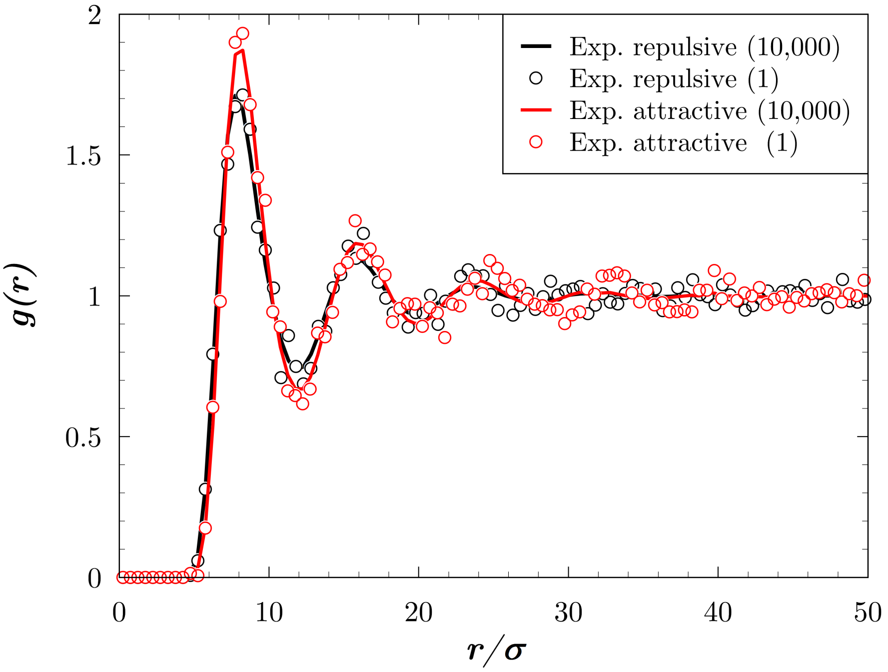

Figure 5.7: Radial distribution plots from simulations for exponential decay without an oscillatory tail (repulsive) and with oscillatory tail (attractive) potentials, both at $\rho^* = 0.015$. The solid black and red lines represent $g(r)$ data obtained by averaging over 10,00 snapshots for repulsive and attractive potentials respectively while the black and red open circles represent $g(r)$ data obtained from 1 snapshot for the repulsive and attractive potentials respectively.

and long-range behaviour: the first has an intermediate range attractive well, while the second has a purely repulsive tail. By comparing the two, we can therefore assess whether, in the presence of experimentally realistic levels of noise, our inversion scheme can still accurately distinguish between differences in the intermediate and long-range behaviour of the underlying potential. It is particularly important that one is able to resolve differences in $u(r)$ in this range since there is considerable controversy in the literature over the existence of an intermediate range attractive component in the effective pair potential between quasi-2D charged colloids confined between two parallel plates

[28, 51, 74, 75, 76, 77].

In figure 5.7, we present $g(r)$ data for these two potentials; the (solid and dashed) lines represent high quality $g(r)$ data obtained from averaging 10,000 snapshots, while the data points represent the noisy $g(r)$ data obtained from 1 snapshot. Clearly, the differences in $g(r)$ between these two potentials is greater than the amplitude of the noise for the first peak and first trough, though the differences in $g(r)$ become smaller than the noise amplitude for subsequent peaks and troughs. This shows that even in the presence of noise, there is still sufficient information in the pair correlation function to distinguish between differences in the intermediate and long-range behaviour of $u(r)$. We also note from figure 5.7 that the differences in the intermediate and long-range behaviour of $u(r)$ primarily manifest themselves as differences in $g(r)$ in the intermediate r range, *i.e.* in the first few maxima in $g(r)$, while the differences at small and large r are small. This point is confirmed in figure 5.8 where we plot (high quality) $S(q)$ data for both the exponential decay potentials. In this case, the difference between $S(q)$ primarily occurs in the intermediate q range, while the difference in the low q range (inset) is very small. The latter point is not surprising since the low q regime of $S(q)$ is controlled by the isothermal compressibility [41], which in turn is primarily determined by the core, rather than the long-range region of $u(r)$. From the above analysis, we conclude that while the core of $u(r)$ influences the behaviour of $g(r)$ ($S(q)$) over the entire r (q) range, the influence of the intermediate and long-range region of $u(r)$ on $g(r)$ ($S(q)$) is primarily restricted to the intermediate r (q) range. Thus while truncation of the r or q range of the input $g(r)$ or $S(q)$ data severely affects the accuracy of the inversion for the core region of $u(r)$, we expect the effect to be much less severe for the intermediate and long-range

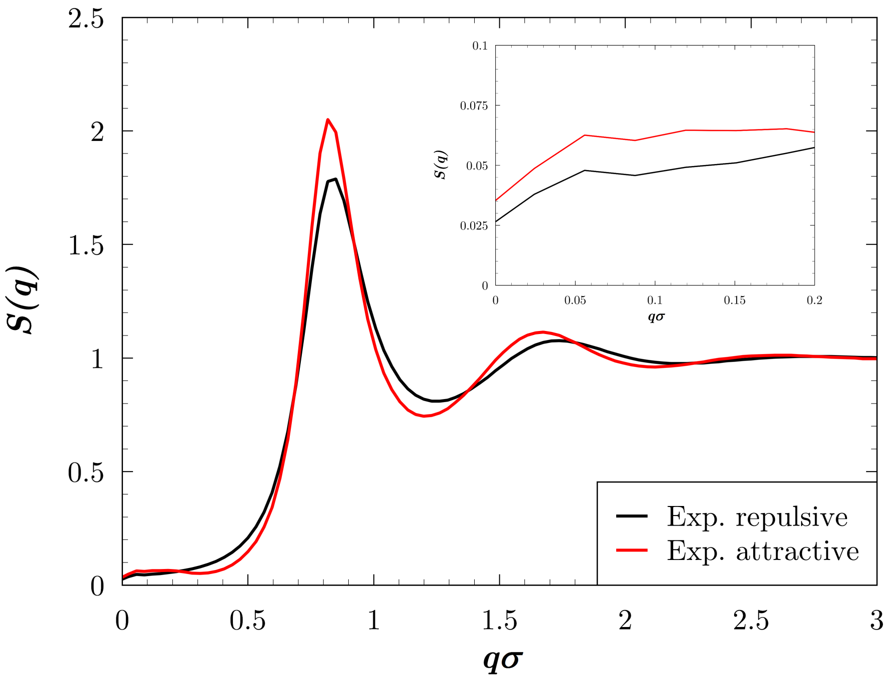

Figure 5.8: High quality $S(q)$ data for the exponential decay potentials without an oscillatory tail (black) and with an oscillatory tail (red) for $\rho^* = 0.015$. The inset shows the results for the low q regime.

region of $u(r)$, provided that the truncated data includes the first few maxima in $g(r)$ or $S(q)$.

In figure 5.9(a) and figure 5.9(b), we present HMSA inversion results for the exponential decay potential without and with the oscillatory tail respectively. In order to quantify the error in the inverted potential, for each potential we inverted $g(r)$ obtained from 3 independent snapshots. This resulted in 3 independent inverted potential outputs, from which we could calculate the mean and the standard deviation, which are the data points and error bars respectively shown in these figures. Clearly, despite the noisy input $g(r)$ data, the HMSA inversion scheme is able to accurately distinguish between the purely repulsive tail in figure 5.9(a) and the attractive well in figure 5.9(b). This is particularly

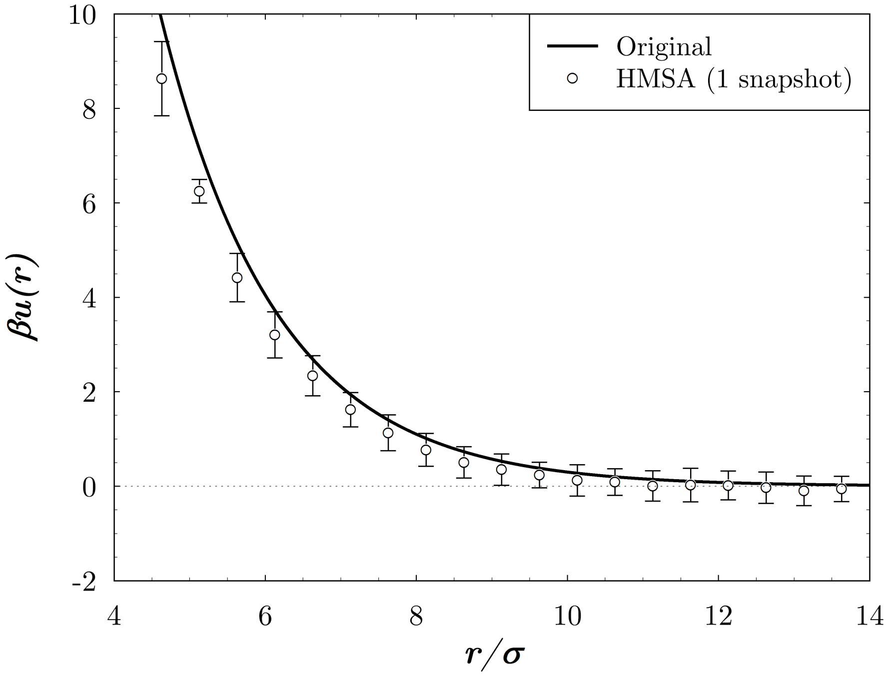

(a)

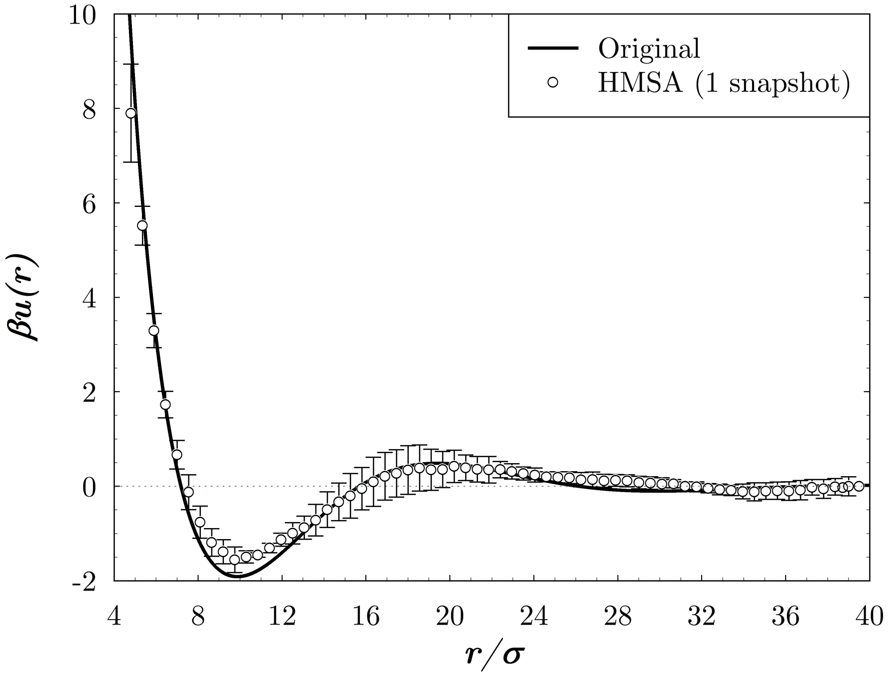

(b)

Figure 5.9: Inversion of (a) exponential decay without and (b) with oscillatory tail potential using the HMSA closure relation from $g(r)$ data taken using only one snapshot.

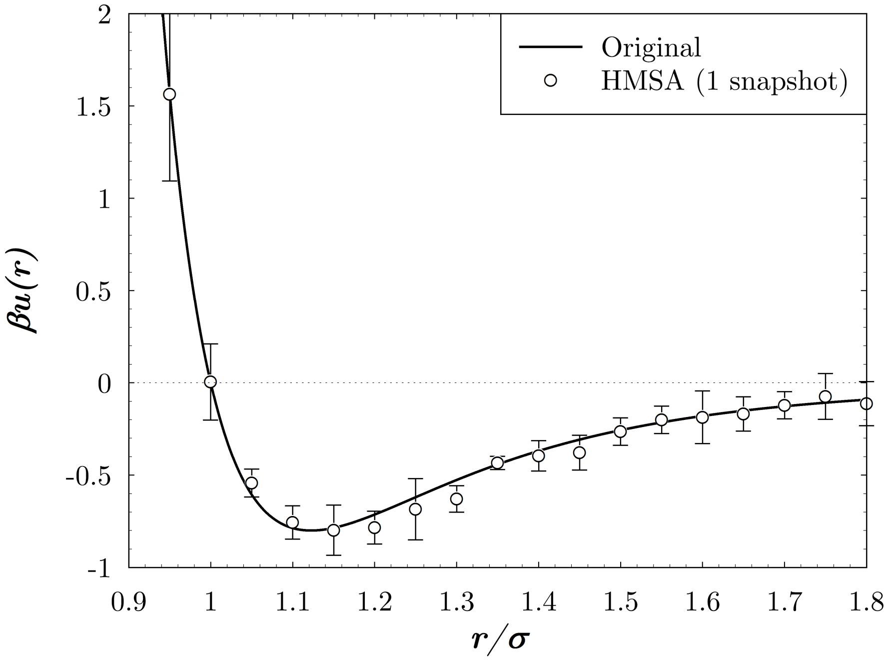

(a)

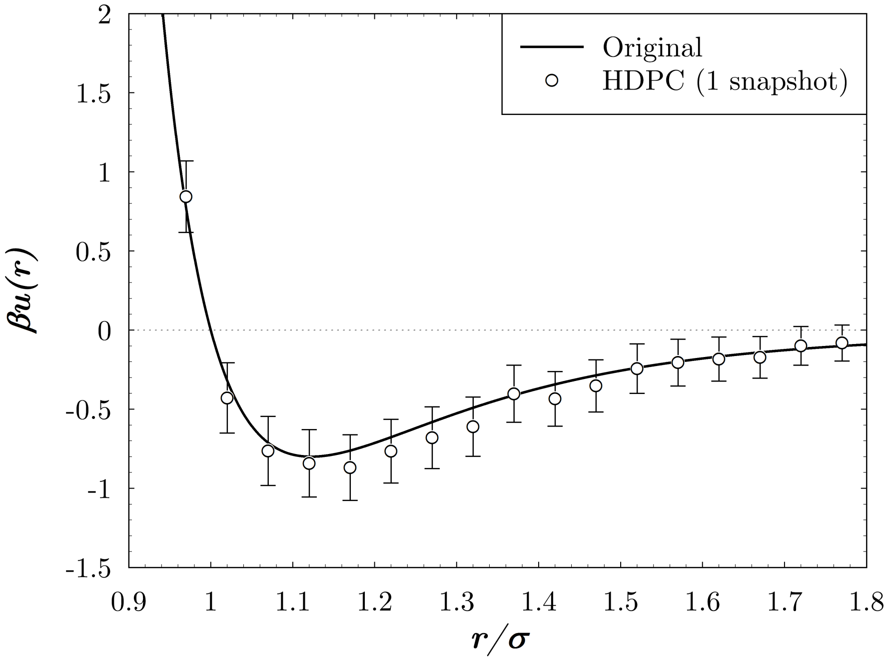

(b)

Figure 5.10: Inversion of LJ potential using the (a) HMSA closure relation and (b) HDPC method from $g(r)$ data taken using only one snapshot.

impressive given the very modest well depth of about $2kT$ used here for the attractive potential. However, the amplitude of the noise in the input $g(r)$ is such that it is not possible to resolve the sub-kT long-range oscillatory tail in $u(r)$ using our HMSA scheme.

Following the same procedure, in figure 5.10(a) and figure 5.10(b) respectively, we present HMSA and HDPC inversion results for the LJ potential, where the monolayer is at a density of $\rho^* = 0.5$. Once again, despite the noisy input $g(r)$ data, both the HMSA and HDPC schemes are able to accurately invert all the salient features of the LJ potential, including the repulsive core and the intermediate range attractive well. We note also that the accuracy of both schemes is comparable. The results in this subsection are very encouraging, demonstrating that both HMSA and HDPC schemes are robust with respect to noise and truncation of the input $g(r)$ data and therefore provide a convenient and accurate method for extracting the effective pair interaction potential from experimental $g(r)$ data for general 2D monolayers.

5.5 Summary

In this chapter we have compared the accuracy of our HDPC with the HMSA scheme with conventional routines based upon the HNC and PY closures for a range of 2D potentials including; exponential decay, Stillinger-Hurd, Lennard-Jones and DLVO. We find that for all these potentials, the HMSA and HDPC schemes are superior to HNC and PY, especially when higher densities are encountered. For densities close to an ordering transition, we find that HDPC scheme is more accurate than the HMSA scheme. The HDPC scheme is therefore better suited to studying hard-core monolayers where there can be significant statistical ordering in the monolayer for relatively small area fractions of the corresponding hard-disk fluid. On the other hand, the HMSA scheme remains numerically stable at densities close to the close packing density of the reference hard-disk fluid where the HDPC scheme becomes unstable. The HMSA scheme is therefore better suited to studying soft-core monolayers where the monolayer can be far from an ordering transition even for densities close to the close packing density of the reference hard-disk fluid. The HMSA and HDPC schemes are therefore complementary to each other.

We have considered the effect of noise and truncation of the r-range of the input $g(r)$ data on the accuracy of the different inversion schemes. We find that a truncation of the r-range of the input $g(r)$ data affects the accuracy of the inversion much less for intermediate to long-range region of $u(r)$ compared to the core region of $u(r)$. Thus, provided our primary focus is to resolve differences in $u(r)$ in the intermediate to long-range, we expect the HMSA and HDPC schemes to be reasonably robust with respect to truncation. We find that even in the presence of experimentally realistic levels of noise in the input $g(r)$ data from simulations, both the HMSA and HDPC schemes are able to faithfully extract the key salient features of the underlying interaction potentials.

Chapter 6

Inversion of $g(r)$ from experiments

In the previous chapter, we tested the accuracy of our HDPC and HMSA inversion schemes on a $g(r)$ data obtained from MC simulations for a wide variety of potentials, and we found that both schemes lead to very accurate inverted potentials, even at high monolayer densities and in the presence of experimentally realistic levels of noise in the input $g(r)$ data. In this chapter we apply the HDPC scheme on $g(r)$ and $S(q)$ generated from experimental data of colloidal monolayers which was kindly supplied to us by Dr. Pietro Cicuta and Dr. Armando Maestro of Cambridge University. We have found that for these data, the HDPC and HMSA schemes essentially yield the same effective potential. For the sake of clarity, we have therefore omitted the HMSA results for the plots from this chapter.

We will first describe the experimental system that we intend to invert, followed by details of how we accurately calculated $g(r)$ and $S(q)$ for the inversion

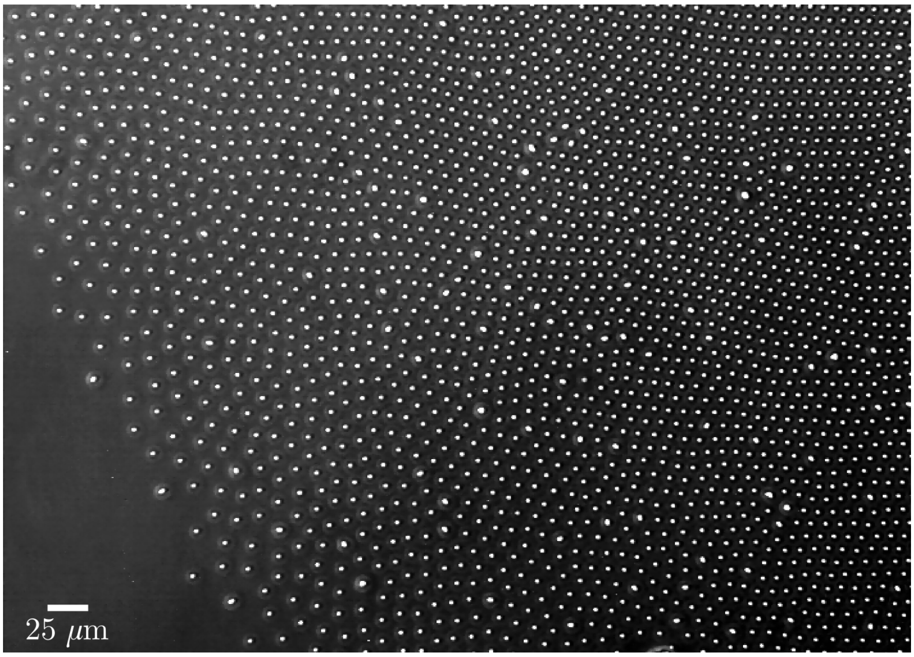

Figure 6.1: Sample snapshot of the oil/water experimental system used for our inversions. The left hand side indicates the co-existence of a fluid-like region with an area featuring no polystyrene particles. Average particle separation on the far right side of the image is $\approx 10\mu$m whilst on the left $\approx 26\mu$m. The scale bar is equal to 25μm. Image data courtesy of Dr. Pietro Cicuta.

process. We will then present the inversion results using the HDPC scheme and the conventional HNC scheme on the experimental data and discuss the nature of the inverted potentials obtained. Finally we summarise the findings of the work presented in this chapter and provide ideas for future research.

6.1 Experimental system

The experimental system consists charge stabilised spherical polystyrene particles, 2μm in diameter confined to an oil/water interface with a contact angle $75 \pm 5°$ measured through the water phase [14] (see appendix C for further experimental details). The particles were spread at the interface and the particle

System	Density ρ (μm^{-2})	Salt Conc. (mM NaCl)	Snapshots available
37p	6.64×10^{-4}	0	330
110p	1.54×10^{-3}	0	20
128p	1.72×10^{-3}	0.05	20
168p	2.29×10^{-3}	0.5	20

Table 6.1: Summary of experimental parameters for the systems studied in this chapter. The significantly higher number of snapshots for the very dilute 37p case was necessary to reduce experimental noise.

positions were tracked over time using video microscopy. From this a large number of snapshots of the particle positions were generated for each of the systems studied. This was the data supplied to us by our collaborators in Cambridge. Using this data as our starting point, we then calculated $g(r)$ and $S(q)$ for each system as discussed in the next section.

A summary of the systems that we invert here are presented in Table 6.1. To investigate the effect of density on the interaction potential, we study two different densities at zero salt concentration in the aqueous sub-phase (*i.e.* 37p, 110p). To investigate the effect of salt concentration, we study three different salt concentrations at approximately the same density (*i.e.* 110p, 128p, 168p).

A detailed study of charged colloids confined to a polar/non-polar interface is very timely because as we discussed in chapter 2, there is still considerable debate in the literature regarding the nature of interactions in such systems. In addition, these systems appear to undergo 2D bulk phase separation into dense crystalline solid regions co-existing with a dilute gas region (see figure 6.1), suggesting the existence of an attractive component within the effective interaction potential. Therefore $u(r)$ obtained from the inversion of $g(r)$ will hopefully shed some light regarding the exact nature of the particle interactions in these systems.

6.2 Calculation of $g(r)$ and $S(q)$ from experimental snapshots

In order to obtain the effective pair potential which are as accurate as possible from our inversion scheme, we need to minimise noise and extend the r-range of our input $g(r)$ data. Specifically we have seen from our discussions in chapter 5 that to obtain accurate inverted potentials, we ideally require $g(r)$ data that contain a few correlation peaks but also converges to 1 at large r, for over at least a quarter of the r-range. For experimentally derived $g(r)$ data, this can be problematic due to the limited field of view and box edges not being periodic like in our simulation data. Therefore, when calculating $g(r)$, we require a more complex algorithm compared to the one described in subsection 3.6.4; specifically the concentric rings created around each particle must be truncated where it crosses the edge of the experimental field of view [78]. Alternatively, one could calculate $g(r)$ using a subset of particles within a smaller box that is inside the original experimental field of view, where all the particles in the inner box are far away enough from the box edge that the concentric circles around these particles do not need to be truncated. This however would drastically reduce the range of r available for our inversions, thus reducing the accuracy of our extracted potentials.

To overcome these problems, we employ a different algorithm altogether: The procedure to calculate $g(r)$ in this way is as follows:

1. For a particular snapshot, we calculate all the interparticle distances r of an N particle system without employing the minimum image convention.

We designate $n_{his}(b)$ as being the number of particles in a particular bin b of width δr that extends from r to $r + \delta r$.

2. In order to reduce experimental noise, we calculate $n(b)$ over N_S snapshots of the system being investigated, and calculate the avergae number of particles in bin b using
$$n(b) = \frac{n_{his}(b)}{N \times N_s}. \tag{6.1}$$

3. In order to normalise the binned data, $n(b)$, we generate pairs of particle co-ordinates randomly within our designated box size, calculate the distances between them and bin them into a separate histogram, $n^{id}_{his}(b)$. The fraction of ideal gas particles at a distance corresponding to a particular bin b away from any ideal gas particle is then given by
$$\frac{n^{id}_{his}(b)}{\sum_b n^{id}_{his}(b)}. \tag{6.2}$$

4. For an N particle system in the box (or field of view), the number of ideal gas particles at a distance b apart from any given particle is
$$n^{id}(b) = (N-1) \times \frac{n^{id}_{his}(b)}{\sum_b n^{id}_{his}(b)}. \tag{6.3}$$

5. Therefore, in order to calculate the radial distribution function, we only need to divide $n(b)$ by $n^{id}(b)$ so that we have our normalised pair correlation function like so
$$g\left(r + \frac{\delta r}{2}\right) = \frac{n(b)}{n^{id}(b)}. \tag{6.4}$$

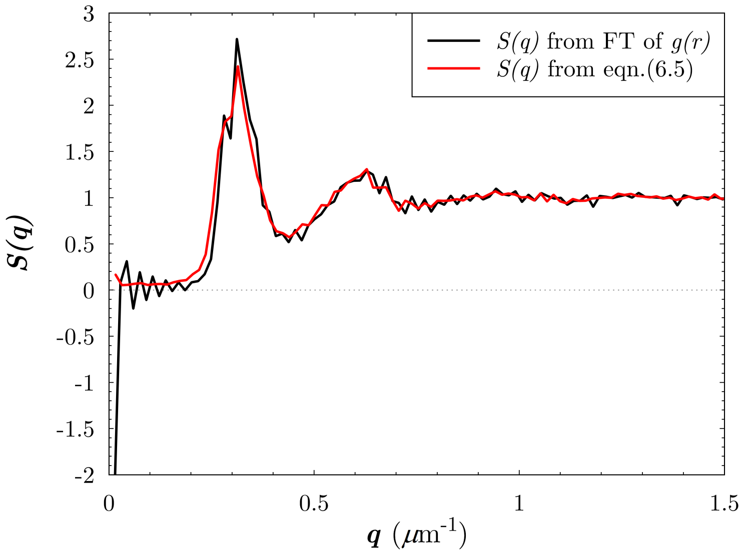

Figure 6.2: Comparison between the structure factor for the system 168p obtained by Fourier transform of $g(r)$ data (black line) and through direct means (red line).

In this way, we can obtain $g(r)$ curves for r values up to the diagonal distance of the box. This substantially increases the r-range of the calculated $g(r)$ and removes the need for any complex algorithms to account for the edge of the system. The $g(r)$'s calculated using our algorithm for all four systems are shown in figure 6.3. It is important to note that for the most dilute case of 37p, we required a substantially larger number of snapshots to reduce experimental noise (see Table 6.1).

As discussed in chapter 3, the inversion methods require *both* $g(r)$ and $S(q)$ data as the input. For $g(r)$ obtained from MC simulations, $S(q)$ can be calculated accurately from the Fourier transform of $h(r) = g(r) - 1$ (see eqn.(3.5)). However for $g(r)$ calculated from experimental data, we have found that the Fourier transform of $g(r)$ generated $S(q)$ data that were extremely noisy in the low q region (see figure 6.2). In particular this procedure generated negative values of $S(q)$ at low q which is unphysical (since this implies negative values for the isothermal compressibility, *i.e.* eqn.(4.17)) and caused all of our inversion schemes to become numerically unstable and produce unphysical oscillations in the inverted potentials. This problem is in fact well documented in the literature [37, 79], and to overcome this problem, it is necessary to calculate $S(q)$ directly from the input snapshots [37, 79]. Specifically, we can calculate the structure factor directly using the formula

$$S(\mathbf{q}) = \frac{1}{N}\left[\left(\sum_{i=1}^{N}\cos(\mathbf{q}\cdot\mathbf{r}_i)\right)^2 + \left(\sum_{i=1}^{N}\sin(\mathbf{q}\cdot\mathbf{r}_i)\right)^2\right], \tag{6.5}$$

where $\mathbf{r}_i$ is the vector position of the ith colloidal particle. For snapshots contained within a square box of length L, the scattering wavevector is restricted to the values $\mathbf{q} = (2\pi/L)(n_x, n_y)$, where $n_x, n_y = 0, 1...N$, except for $n_x = 0$ *and* $n_y = 0$. In order to obtain $S(q)$, *i.e.* the structure factor as a function of the scalar $q = |\mathbf{q}|$, we circularly average $S(\mathbf{q})$ for our 2D homogeneous fluid. Using this method gave smooth and positive values in the low q region for $S(q)$ which could then be used in our inversion scheme (see figure 6.2). We have also checked that using $S(q)$ calculated from this direct method gave the same results for the inverted potentials in chapter 5 thus validating the method.

6.3 Inversion results and discussion

In this section we present the effective potentials extracted using our HDPC scheme for the four experimental systems listed in Table 6.1. We begin by presenting the inversion results for different densities at zero salt concentration

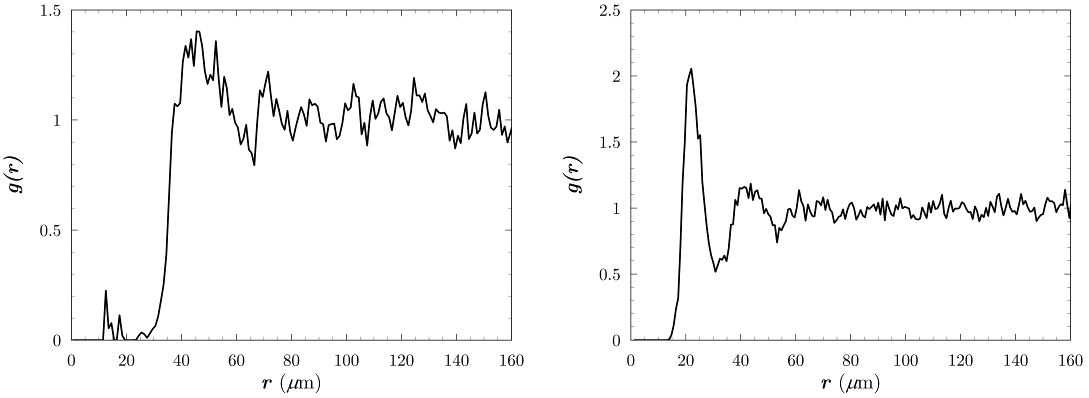

(a) 37p ($\rho = 6.64 \times 10^{-4} \mu\text{m}^{-2}$)

(b) 110p ($\rho = 1.54 \times 10^{-3} \mu\text{m}^{-2}$)

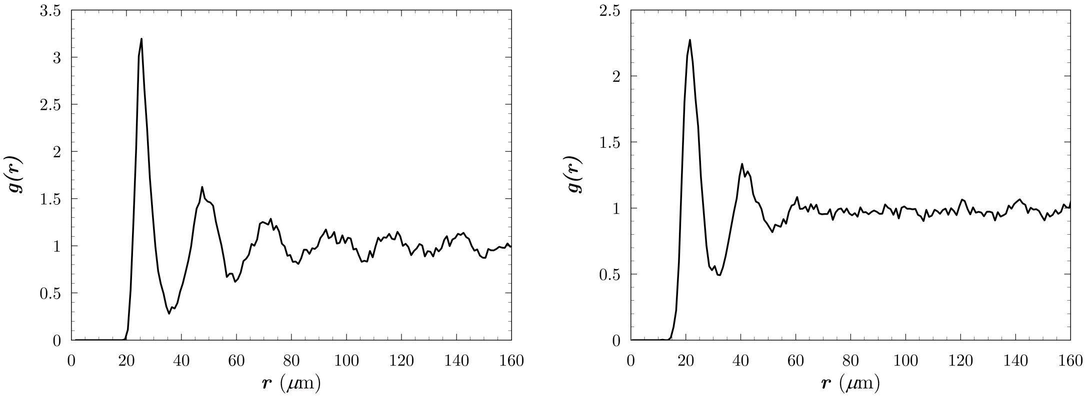

(c) 128p ($\rho = 1.72 \times 10^{-3} \mu\text{m}^{-2}$)

(d) 168p ($\rho = 2.29 \times 10^{-3} \mu\text{m}^{-2}$)

Figure 6.3: Experimental $g(r)$ data calculated from video microscopy snapshots for the systems listed in Table 6.1.

within the water phase. The inverted potentials obtained from the most dilute system **37p** (0mM NaCl, $\rho = 6.64 \times 10^{-4} \mu\text{m}^{-2}$) is shown in figures 6.4(a) and 6.4(b). The error bars shown on figure 6.4 (and on figure 6.5) have been calculated from the standard deviation from inversions of three independent sets of snapshots. Figures 6.4(a) and 6.4(b) also show the HNC inversion result for this dilute case. We can see that the HNC results agree with the HDPC results within the error bars, which suggests that the experimental system is in the dilute regime

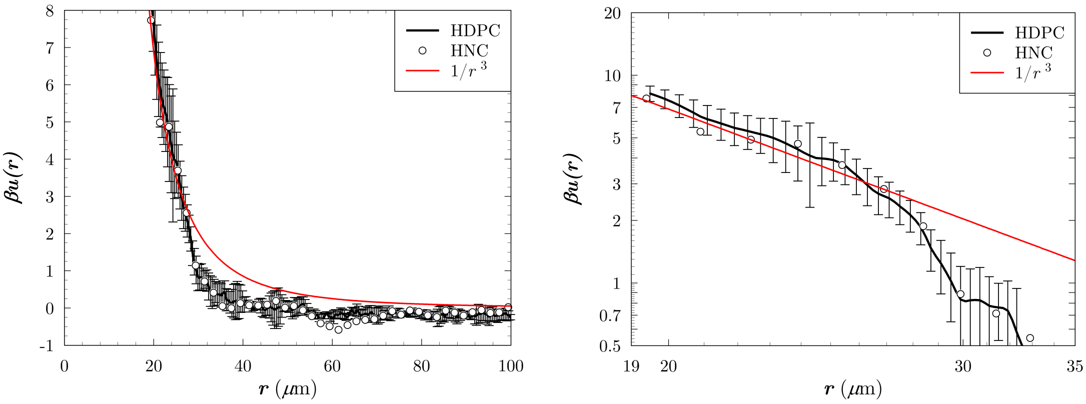

(a) 37p

(b) 37p

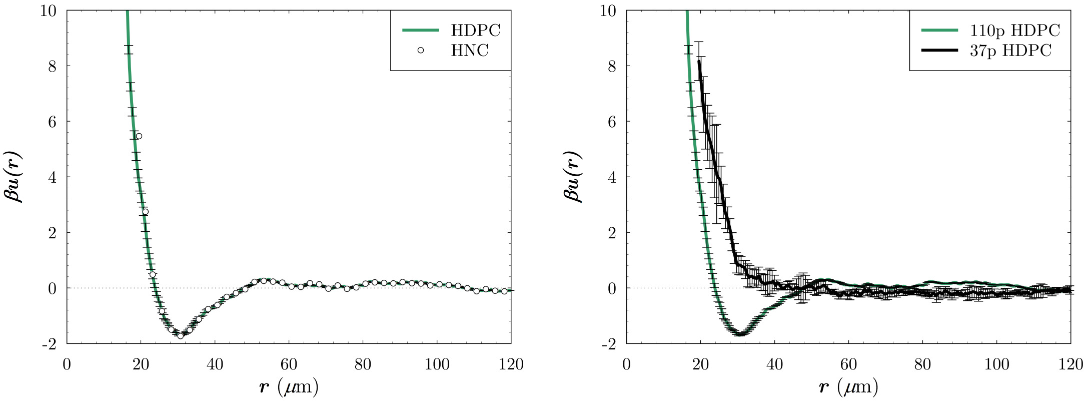

(c) 110p

(d) 37p & 110p

Figure 6.4: Inversion potentials for the 37p system (a),(b) and 110p system (c) using the HDPC and HNC methods. (b) shows the low r region of the inverted potential as a log-log plot, while (d) shows the HDPC results for both 37p and 110p. For comparison, we also show the dipole-dipole r^{-3} form on both (a) and (b).

as far as the inversion is concerned, where all the inversion schemes converge (see figures 5.5 and 5.6) and faithfully represent the underlying potential. From figures 6.4(c) and 6.5, we also see that all other systems studied in this chapter (*i.e.* 110p, 128p and 168p) are also in this regime where the HNC and HDPC converge.

We can see that from figures 6.4(a) and 6.4(b) the inverted effective potentials are purely repulsive. For comparison, in figure 6.4(a) and 6.4(b) we have also plotted the dipole-dipole form of r^{-3} expected for very dilute charged colloidal systems at a polar/non-polar interface [14, 18]. At small r, we can clearly see that the dipole-dipole form is followed, however for $r \gtrsim 30\mu$m, the interaction potential decays much faster than r^{-3}. Preliminary forward checks that involve MC simulations of colloids interacting via the r^{-3} potential and an interpolated form of the extracted potential shown in figure 6.4(a) indicate that the input $g(r)$ data can be reproduced by the interpolated potential but not the r^{-3} potential. These forward checks suggest that the deviations away from r^{-3} are in fact *real* and not due to random noise. Since it is well established in the ultra dilute regime that the interactions in this system have a dipole-dipole form, our results for 37p suggests that many-body effects may be significant even for this relatively low concentration system.

Next we consider the higher density sample, **110p** (0mM, $\rho = 1.54 \times 10^{-3}\mu\text{m}^{-2}$) where the inversion results using the HDPC and HNC schemes are illustrated in figure 6.4(c). We can see that the interactions in this system clearly develop an attractive component and that the magnitude of the attractive well ($\approx 1.9kT$) is much greater than the error bars, suggesting that this attractive well is real and not due to random noise in the source $g(r)$ data. In order to highlight the density dependence of the interaction potentials, in figure 6.4(d) we superpose the inverted potentials for 37p and 110p. We see that while the interaction potentials for both systems converge at small and large r, the behaviour at intermediate r ($\approx 30\mu$m) clearly depends on the density of the monolayer and goes from repulsive to attractive as we increase ρ.

As already discussed, it is well established from previous studies [14, 18] that the bare potential for this system (*i.e.* the potential at infinite dilution) is purely

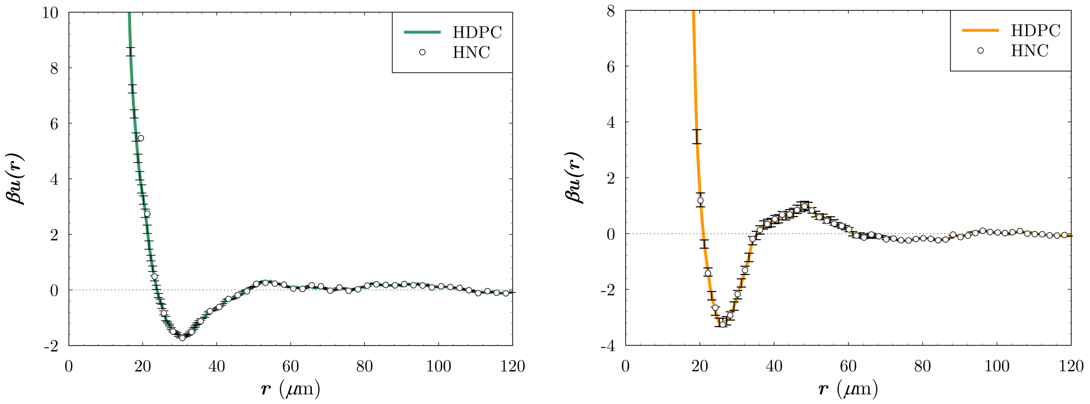

(a) 110p (0mM NaCl)

(b) 128p (0.05mM NaCl)

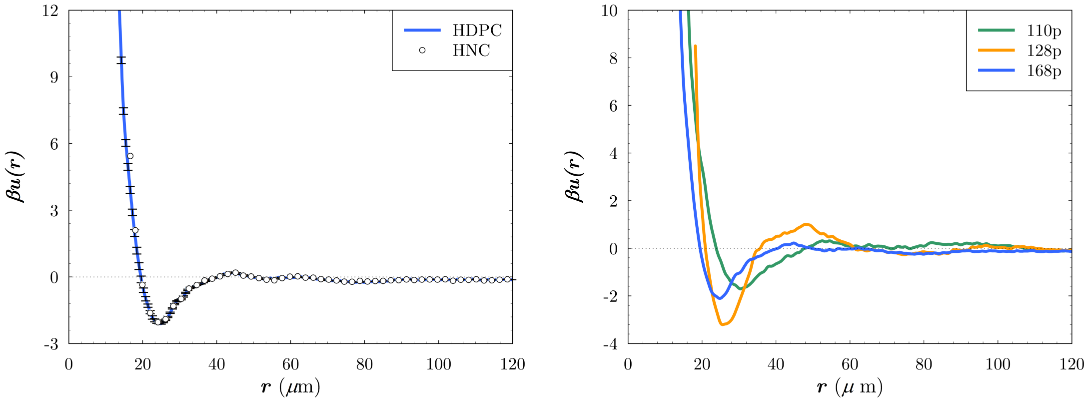

(c) 168p (0.5mM NaCl)

(d) 110p, 128p & 168p

Figure 6.5: Inversion results for the higher density samples of varying salt concentration using the HDPC and HNC methods. The error bars are the standard deviation from three independent inversions for each system.

repulsive and of a dipole-dipole form. Our results in figure 6.4 clearly deviate from this accepted form which is unexpected and thus very important. The attractive component seen for 110p is consistent with the experimental image in figure 6.1 illustrating the co-existence between a fluid and a solid phase. The nature of the attractive component found in figure 6.4(c) will be discussed in further detail later in this section.

We now consider the inversion results for systems of varying salt concentration in the water phase at approximately equal number densities. Specifically, in figures 6.5(a), 6.5(b) and 6.5(c) we show the HDPC and HNC inversion results for the **110p** (0mM NaCl, $\rho = 1.54 \times 10^{-3}\mu\text{m}^{-2}$), **128p** (0.05mM NaCl, $\rho = 1.72 \times 10^{-3}\mu\text{m}^{-2}$) and **168p** (0.5mM NaCl, $\rho = 2.29 \times 10^{-3}\mu\text{m}^{-2}$) respectively, while in figure 6.5(d) we superpose the HDPC inversions for all three systems on one single plot.

It is evident that all of the inversion results using both the HDPC and HNC have attractive wells at $\approx 25\mu$m. The magnitudes of the attractive wells for all three systems is much greater than the error bars indicating that these attractive components are real and not artefacts of the inversion (specifically, the depth of the potential well ranges from $\approx 1.9kT$ for the 110p case to $\approx 3.5kT$ in the 128p case). Furthermore, we see that by superposing all three HDPC inversions as shown by figure 6.5(d) that the inversion results are reasonably *insensitive* to salt concentration, though we note that for the 128p system, the medium density of the three cases considered here, has the deepest attractive well and a small repulsive barrier at $\approx 50\mu$m which is absent in the 110p and 168p. The presence of a significant attractive well in our colloidal monolayer is thus robust with respect to variations in salt concentration.

As discussed in section 2.1.1, the dominant contribution to the interaction in this system is likely to be presence of residual charges trapped on the surface of the colloidal particle in the oil phase. The relative insensitivity to salt concentration in the interaction potential as shown by figure 6.5(d) appears to support this model. Finally we note that the position of the attractive well at $\approx 25\mu$m is in good agreement with the average distance between particles for fluid regions in the centre of figure 6.1.

The origin of the attractive component in our inverted potentials at high density remains unclear at present. We note that a number of studies of charged colloidal particles confined in a thin sample cell (*i.e.*, between two parallel plates), have found that a long ranged attraction appears in these systems [74, 75, 76, 77]. This like-charge attraction cannot be explained with the standard mean field theories, irrespective of whether the particles are in the bulk or in a confined geometry. However, it has been reported very recently that the observed like-charge attracttion may in fact be an artefact of optical distortions in the video microscopy results [51].This phenomenon appears to only interfere with samples that are in confinement and for particles that are close to one another where they are likely to encounter a reduced double layer effect *i.e.* $r < 2d$.

A number of other studies have considered many-body phenomenon in colloidal monolayers confined to 2D by optical traps. These experimental studies focus on the density dependence of the effective interaction, obtained either through the inversion of pair correlation functions, where the number density of the monolayer is systematically increased, or by utilising a setup that involves the analysis of three particles in isolation to thus obtain a *three-body interaction* potential [80, 81, 82]. The inclusion of a third particle will partially cancel the electrostatic repulsion between the original two particles. This phenomena, which is commonly referred to as *macroion screening* [28], will in the case for a pair potential, appear as an attractive well. This many-body effect in bulk suspensions has been shown to cause significant deviations from the expected Yukawa-like potential. One key difference between our system and these considered above is that in our case the colloids are confined to 2D by a fluid interface, while those in the studies above are confined to 2D by the walls of the container or by an optical trap. We therefore expect the physics leading to an attractive pair potential in our system to be different from that in the studies above. The origin of the attractive component in the interaction potential of our monolayers will be the subject of a future study.

6.4 Summary and future work

In this chapter, we have we applied the HDPC scheme on $g(r)$ and $S(q)$ calculated from experimental data of colloidal monolayers. Specifically, we have investigated how the effective interaction potential depends on the density and salt concentration of a system of polystyrene particles confined to an oil/water interface. We observe that there is a clear density dependence on the effective interaction; at low number densities the interaction potential is purely repulsive while at higher densities an attractive well gradually appears. For samples of approximately the same number density, we find that the interaction potential, including the potential well, is largely insensitive to salt concentration, thus supporting the idea that the interaction for this system perhaps occurs due to residual charges interacting through the oil phase.

The convergence of HDPC and HNC routines provide indirect evidence that the inverted potentials are accurate. We acknowledge the fact that these inversion results only provide a preliminary solution to the problem of interactions at oil/water interfaces and therefore inversions on new experimental data are required. However, in order to confirm accuracy of inverted potentials directly, for future work we plan to use the inverted potentials in Monte Carlo simulations to see if they reproduce the input $g(r)$. However this requires accurate but numerically convenient parametrisations of $u(r)$ found through the inversion process.

For charged colloids at a polar/non-polar fluid interface, it is well established that interaction has a dipole-dipole form in the ultra dilute regime. For our most dilute sample (37p), we observe a dipole interaction form at small r but not at large r. For future work, it would therefore be useful to study an even more dilute system to see if we can recover the dipole interaction over all r. This will not only allow us to make a connection with previous experimental studies, but it will also help us to determine at what densities many-body interactions start to become important.

Finally, the origin of the attractive component in extracted $u(r)$ at high densities for our system is still unknown at the current time, though the well depth clearly depends on density but is independent of salt concentration, suggesting that this is a many-body effect. This will be the subject of a more detailed study in the near future.

Chapter 7

Structure of binary colloidal monolayers

Up till now, we have focussed our attention on deducing the functional form of the effective interaction potential between colloids at fluid interfaces. As we indicated in chapter 1, the interaction between colloids has a profound influence on the structure of colloidal monolayers. For example, by tuning the interaction between colloidal particles *e.g.* by changing the wetability of the particles, it is possible to obtain either ordered crystals or disordered, aggregated clusters in a one component colloidal monolayer at an oil/water interface [1].

In recent years, there has been growing interest in the structure of binary systems, *i.e.* colloidal systems consisting of two different species of colloidal particles. For example, in 3D, both binary mixtures of hard spheres [83, 84] and charged colloids [85, 86, 87, 88] have been observed experimentally and predicted theoretically to form lattice structures from NaCl cubic to AB_{13} with almost every stoichiometry in between, including structures with no atomic analog [87, 86].

Binary colloidal crystals in 2D have been theoretically predicted to have an equally rich phase behaviour. For binary HD systems, Likos and Henley [89] using local packing arguments have predicted over ten distinct stable pure alloy phases. For binary colloidal systems interacting via a softer dipole-dipole repulsion, theoretical investigations at zero temperature ($T = 0$ K) have also predicted a similarly large number of stable alloy phases spanning all five Bravais lattices, with a basis comprising various stoichiometries of A and B particles [90, 91], while MD simulations at finite temperatures predict stable hexagonal AB_2 and AB_6 super-lattices [92]. Further research on binary dipolar colloidal systems have investigated the effect of tilted magnetic fields on the zero temperature structures [93] and the phonon spectra of periodic structures formed by 2D mixtures of dipolar colloidal particles [94].

In this chapter, we focus on the structure of 2D binary mixtures of colloidal particles interacting via a dipole-dipole potential. Our study is motivated by recent experimental results by Dr. Tommy S. Horozov (Department of Chemistry, University of Hull) on mixed monolayers of large and small very hydrophobic silica particles at an octane/water interface.

In this chapter, we first present experimental results for the structure of this mixed monolayer system obtained by Dr. T. S. Horozov. We then discuss the parametrisation of the system, followed by investigations into the behaviour of the binary crystals at zero temperature ($T = 0$ K), in order to establish the ground state crystal structures. This will be compared directly to the behaviour of binary colloids at finite T, investigated using MC simulations. Specifically we investigate the thermodynamic stability of the zero temperature binary structures, the melting transition of these crystals, and the metastability of the binary system.

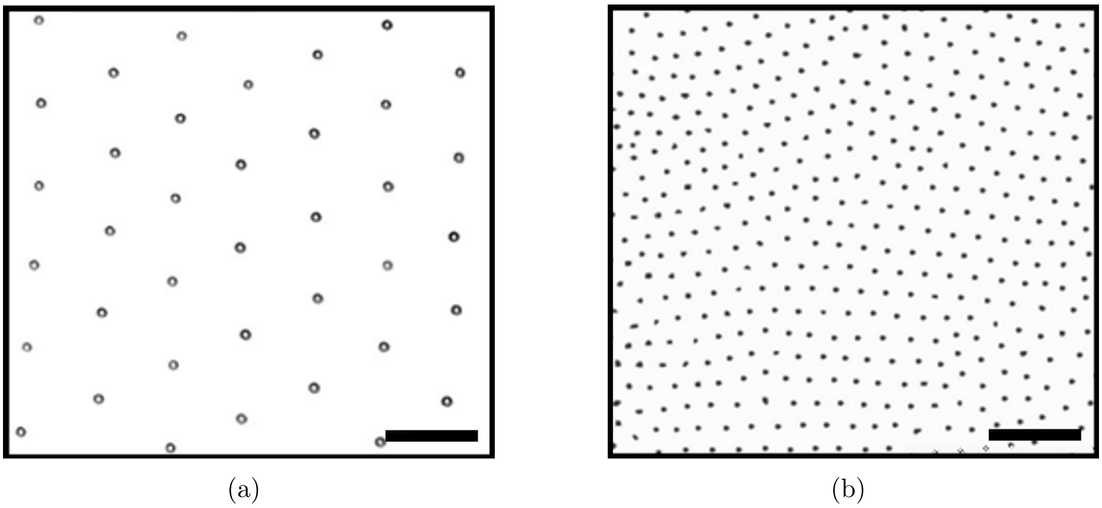
(a)

(b)

Figure 7.1: One component monolayers of silica particles with diameter (a) $3\mu m$ and (b) $1\mu m$ at a horizontal octane/water interface. The scale bars are equal to $30\mu m$ and the average distance between large particles in (a) is $28\mu m$.

Finally we give a summary of our results and outline future work.

7.1 Experimental details and results for binary system

Here we present a summary of the experimental data kindly supplied to us by Dr. T. S. Horozov of the Department of Chemistry, University of Hull. The experimental system is a mixture of large (A) and small (B) very hydrophobic spherical silica particles with diameters $3.00 \pm 0.05\mu$m and $1.00 \pm 0.05\mu$m respectively, trapped at a octane/water interface. Full details can be found in appendix D. These particles easily form ordered one component hexagonal crystals as shown by figure 7.1. For both one and two component monolayers, the average distance between the large particles in the hexagonally ordered monolayers is given by

$$l = \left(\frac{\sqrt{3}\rho_A}{2}\right)^{-1/2}, \tag{7.1}$$

which can be varied by modifying the number density of the large particles spread at the liquid interface, ρ_A. The experimental results that we present in this section correspond to $l = 28\mu$m, but well ordered arrays of large particles were also observed at $l = 60\mu$m, suggesting that strong long-ranged repulsive particle interactions are occurring in the studied systems [95].

We now present results of the mixed monolayers at the octane/water interface. It is convenient in this case to introduce the number fraction of small (B) particles as

$$\xi = \frac{\rho_B}{\rho_A + \rho_B}, \tag{7.2}$$

where ρ_B is the number density of the small particles. We begin by illustrating the results for the lowest concentration of B particles with respect to the A particles *i.e.* $\xi < 2/3$ as shown by figure 7.2(a). We can see that each small particle resides in the interstitial sites between three large particles without distorting the large particle lattice, thus suggesting that the repulsive interaction strength of the small particles is much smaller than that of the large particles. At higher ξ, AB_2 super-lattices were observed in those regions of the mixed monolayer where $\xi = 2/3$ (figure 7.2(b)). These regions were surrounded by large areas with underdeveloped ($\xi < 2/3$, figure 7.2(a)) or overdeveloped ($\xi > 2/3$, figure 7.2(c)) AB_2 structures as a result of the non-uniform distribution of the small particles. Note that the interesting 'zigzag' structure shown in figure 7.2(c) (in regions where $\xi \approx 3/4$) can be obtained by inserting small particles in the interstitial sites between two large particles. Further increase of ξ to $\xi = 5/6$ resulted in

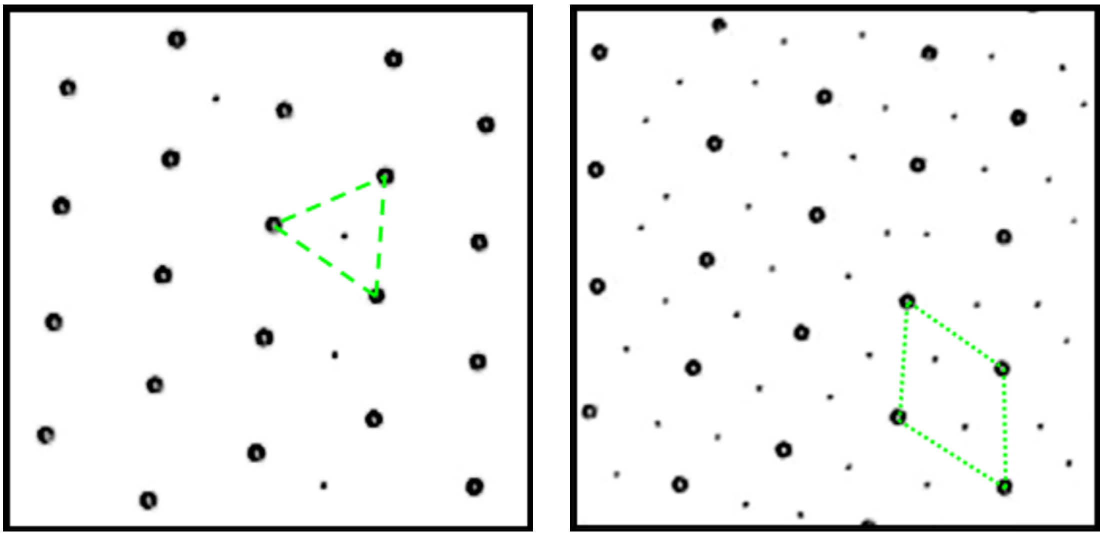

(a) $\xi < 2/3$

(b) $\xi = 2/3$

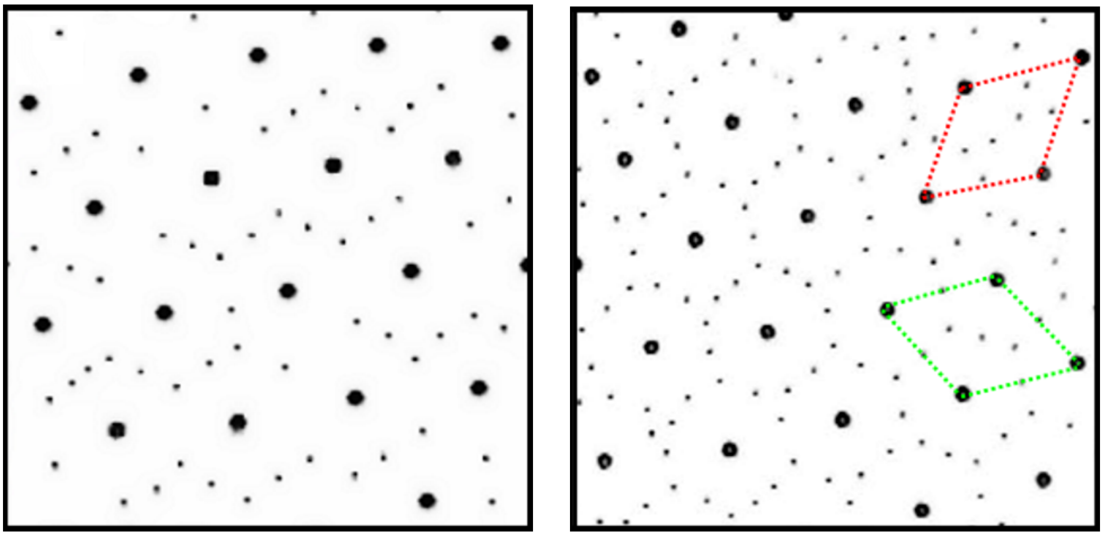

(c) $\xi \approx 3/4$

(d) $\xi \approx 5/6$

Figure 7.2: Structure of mixed monolayers of large and small silica particles at the horizontal octane/water interface for different number fractions of small particles, ξ. The average distance between the large particles is $l = 28\mu$m. Images courtesy of Dr. T. S. Horozov.

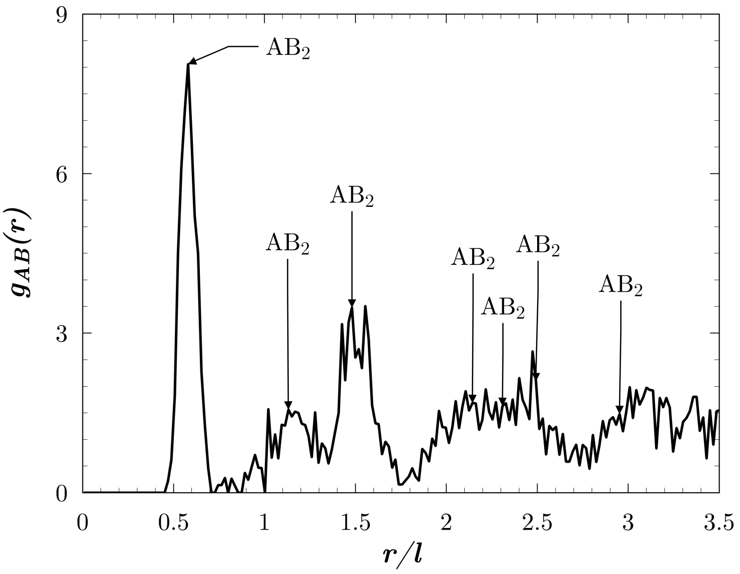

Figure 7.3: The radial distribution function g_{AB} for the structure shown in 7.2(b); the theoretically calculated Bragg peak positions for the AB$_2$ minimum energy configuration are indicated by arrows..

the formation of regions with a honeycomb-like structure (figure 7.2(d)) where coexisting unit cells of AB$_5$ and AB$_6$ lattices can be identified.

We note that the range of order seen in figures 7.2(b), 7.2(c) and 7.2(d) is substantially longer than in any previous experimental studies of 2D binary colloids. In particular, the AB$_2$ system ($\xi = 2/3$) exhibits long-range order. This can be seen in figure 7.3 where we show the experimental radial distribution function of B particles around any given A particle $g_{AB}(r)$, for this structure and compare this with the theoretically calculated Bragg peak positions for an AB$_2$ minimum energy configuration (*i.e.* the global energy minimum), though they are not clearly resolved from each other due to experimental noise. In order to understand these structures theoretically, in what follows we first discuss a suitable parametrisation for the colloidal interaction in this system. Using these interaction potentials, we then calculate the structure of the mixed monolayer at both zero temperature and finite temperature.

7.2 System parameters

7.2.1 Form of the interaction potential

We have reviewed in section 2.1.1 the main contributions to the interaction between particles confined to an oil/water interface. For the hydrophobic silica particles discussed in the previous section, the magnitude of these different contributions have been estimated in ref.[95]. Specifically these contributions include Pieranski dipole repulsions [8] due to the asymmetric double layer around the colloidal particles on the aqueous side at the level of the linearised Stillinger-Hurd model [9, 10], electrostatic repulsions due to dipoles [96] and residual charges [97, 14] at the particle/oil interface and capillary attractions due to the undulated three phase contact lines around the particles caused by surface roughness [98, 99] (see section 2.1.1 for further details). It was found that the dominant term in the colloidal interactions is the repulsion due to residual charges at the particle/oil interface [95]. This is also consistent with the fact that the repulsion was essentially unaffected by the pH [95] or salt concentration (up to 1M NaCl) [100] of the aqueous sub-phase.

We note that a recent theory by Frydel *et al.* [17] has incorporated non-linear charge re-normalisation effects into the Pieranksi dipole repulsions and found that this also led to a very weak dependence on salt concentration. However this theory under-predicts the experimentally measured colloidal repulsions by at least an

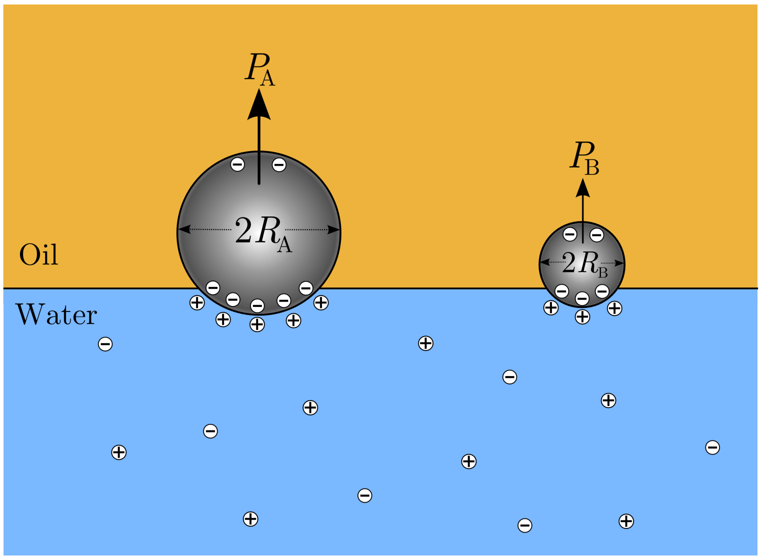

Figure 7.4: Schematic diagram illustrating binary colloidal model of large (A) and small (B) particles of diameters $2R_A$ and $2R_B$ respectively separated by an interparticle distance r. Residual surface charges create an effective dipole with the image charge formed in the water (polar phase). P_A and P_B are the effective dipoles of the large and small particles respectively due to these charges.

order of magnitude. Very recently, Vermant and coworkers [18] have shown that the dipole moment from the dense counter-ion ('Stern') layer at the particle/water interface can lead to dipolar interactions of the correct order of magnitude. However this contribution is likely to be small for our very hydrophobic silica particles where the area of the particle/water interface is very small (6.7% of the total particle area). Having carefully considered all the contributions above, we believe that the presence of residual charges at the particle/oil interface remains the most plausible explanation for the very strong electrostatic repulsions found in our experimental system.

In order to calculate the colloidal interactions due to these residual charges, we use the model presented by Aveyard *et al.* [97] where the residual charge for a colloid particle of species $i (i = A, B)$ with radius R_i, contact angle θ and surface charge density at the particle/oil interface σ (assumed to be the same for large and small particles), is represented by a point charge $q_i = 2\pi R_i \sigma (1 - \cos\theta)$ at a distance $\zeta_i = R_i(3 + \cos\theta)/2$ above the oil/water interface. This creates an effective dipole moment of $P_i = 2q_i\zeta_i$ due to the residual charge in the aqueous sub-phase [97] (see figure 7.4). For large particle separations $r \equiv |\mathbf{r}|$ such that $(\zeta_i/r) \ll 1$, a condition that is easily satisfied for the relatively low particle densities considered in section 7.1, the pair interaction potential between particles of species i, j separated by a interparticle distance r has an asymptotic dipole-dipole form

$$\beta U_{ij}(r) = \Gamma m_i m_j \frac{l^3}{|\mathbf{r}|^3}, \qquad i, j = A, B, \tag{7.3}$$

where $m_i = P_i/P_A$ is the dipole moment ratio, l is the average distance between large particles in the hexagonal phase (eqn.(7.1)) and the energy scale of the interaction is set by

$$\Gamma = \frac{P_A^2}{8\pi\varepsilon_r\varepsilon_0 k_B T l^3}, \tag{7.4}$$

where P_A is the dipole moment on the A particle. Note that our binary colloidal system is fully characterised by three parameters: The interaction strength Γ, the dipole ratio m_B and the number fraction of small particles ξ, respectively.

The interaction potential, eqn.(7.3) is also relevant to other binary dipolar systems such as the system presented by Hoffman *et al.* [101] which consists of a binary mixture superparamagnetic colloids held within a strong magnetic field $\mathbf{B}$ that induces the dipole moment $\mathbf{M_i} = \chi_i \mathbf{B}$ on each particle, where χ_i is the magnetic susceptibility. For this system however the interaction strength Γ is

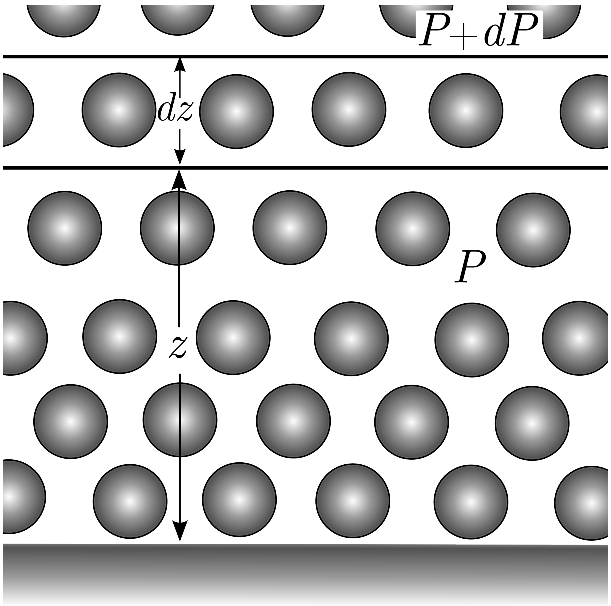

Figure 7.5: Sedimentation of a vertical colloidal monolayer due to gravity. The surface pressure at height z and $z + dz$ is P and $P + dP$ respectively.

given by $\Gamma_M = \mu_0 \chi_A^2 \mathbf{B}^2 / 4\pi l^3$, where μ_0 is the permeability of free space.

7.2.2 Estimation of interaction parameters

In order to estimate the interaction strength Γ, we require values of the parameters included in eqn.(7.4). Most of these values are known accurately except for the charge density at particle/oil interface σ which is a key parameter in determining Γ. In order to estimate σ for our system, we use previous experimental data for the sedimentation of vertical monolayers of the 3μm silica particles [95]. For a vertical monolayer of colloid particles at the interface, the gravitational force acting on the colloid particle leads to sedimentation so that both the surface density ρ and surface pressure P of colloids in the monolayer vary with height z. Let us consider a thin horizontal slice of the vertical monolayer of thickness dz at a height z as shown in figure 7.5. At equilibrium, the differential surface pressure between the top and bottom edge of the slice dP must balance the gravitational force acting on the slice, *i.e.*,

$$dP = -\rho m * g dz, \tag{7.5}$$

where $m * g$ is the difference between the particle weight and the buoyancy force from both the water and oil phase and is given by the expression [95]

$$m * g = g(\rho_p - \rho_w)V_{pw} + g(\rho_p - \rho_o)V_{po}, \tag{7.6}$$

where g is the acceleration due to gravity, V_{pw} and V_{po} are the particle volumes immersed in the water and oil phases respectively, and ρ_p, ρ_w and ρ_o are the mass densities of the particle, water and oil, respectively. For a colloid particle, the volumes immersed in both phases are given by $V_{pw} = \pi R^3(1 + \cos\theta)^2(2 - \cos\theta)/3$ and $V_{po} = 4\pi R^3/3 - V_{pw}$.

Using eqn.(7.1), the surface density of the monolayer ρ is related to the average interparticle distance through the following relationship

$$\rho(l) = \frac{2}{\sqrt{3}l^2}. \tag{7.7}$$

We assume that the major contribution to the surface pressure in the monolayer is from the repulsion between residual charges trapped at the particle/oil interface and that $l \gg R$. With these in mind, the surface pressure P is related to l

through the following relationship [97]

$$P(l) = \frac{4\sqrt{3}q^2\zeta^2}{\pi\varepsilon\varepsilon_0 l^5}. \tag{7.8}$$

Inserting eqns.(7.7) and (7.8) into eqn.(7.5) and integrating with respect to l and z, we find that l varies with z such that

$$\frac{1}{l^3} = \frac{1}{l_0^3} - \alpha z, \tag{7.9}$$

where l_0 is the interparticle spacing at $z = 0$ and

$$\alpha = \frac{m * g\pi\varepsilon\varepsilon_0}{10q^2\zeta^2}. \tag{7.10}$$

Finally, we can obtain an expression for the surface charge density by rearranging eqn.(7.10) such that

$$\sigma = \frac{1}{2\pi R^2(1-\cos\theta)}\left(\frac{m * g\pi\varepsilon\varepsilon_0}{10\alpha\zeta^2}\right)^{1/2}. \tag{7.11}$$

Therefore if we plot l^{-3} against z, we can determine α and hence σ. The variation of l with respect to height z was found in vertical monolayers by Horozov *et al.* using the method outlined in ref.[95] for a system comprised of vertical water films in octane whose surfaces were sparsely covered with 3μm very hydrophobic silica particles. The reported result was that the interparticle distance increases with z from about 13μm at the bottom of the monolayer to 16μm close to the top. This indicates that there is strong long-range repulsion between the particles which is capable of opposing the gravity, thus keeping the particles well separated and ordered in a hexagonal lattice. From the plot of l^{-3} against z in figure 7.6, we

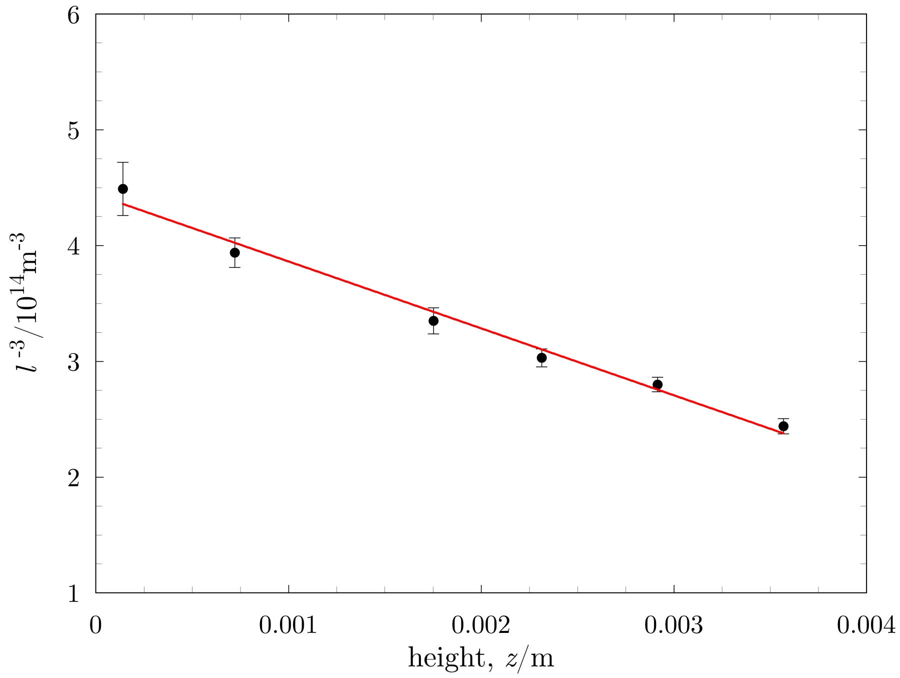

Figure 7.6: Variation of the inter-particle distance, l with height, z, in a vertical monolayer of 3μm hydrophobised silica particles at the octane/water interface plotted as l^{-3} versus z to determine the surface charge density at the silica particle/octane interface. The red line is the best fit line according to eqn.(7.11) with $\alpha_x = 5.8 \pm 0.3 \times 10^{16}$ m^{-4}. Experimental data provided by T. S. Horozov.

find $\alpha = 5.8 \pm 0.3 \times 10^{16}\mathrm{m}^{-4}$. Inserting this and the remaining system parameters $\rho_w = 1000$ kg·m^{-3}, $\rho_o = 703$ kg·m^{-3}, $\rho_p = 2000$ kg·m^{-3}, $\theta = 150°$, $R = 1.5\mu$m, $\varepsilon = 2.0$ into eqn.(7.11), we find $\sigma = 98 \pm 3 \times 10^{-6}$ C·m^{-2}. Using this value of σ and $l = 28\mu$m, we obtain $\Gamma = 1.7 \pm 0.1 \times 10^3$. It is important to note that our calculated interaction strength is approximately an order or magnitude greater than those predicted in other binary experiments, such as the investigation conducted by Hoffmann *et al.*, where the interaction strength used in ref.[101] is $\Gamma \approx 100$. Our higher value for Γ is at least one order of magnitude higher than that in ref.[101] and may therefore explain why the range of order observed in section

7.1 is substantially longer that what has been observed in previous experimental systems.

Assuming the same value of σ for large and small particles, we also find that $m_B = (R_B/R_A)^3 = 0.037$. For the finite temperature MC simulations in section 7.5.1, we primarily focus on systems with these experimental values for Γ and m_B. However for the zero temperature lattice sum calculations in section 7.4, we also explore other values of m_B around the experimental value in order to understand how the binary crystal structure varies with m_B (Γ is irrelevant for zero temperature calculations).

7.3 Theoretical methods

7.3.1 Lattice sum method

In order to understand theoretically the super-lattice structures formed by the binary colloid system, we will calculate the minimum energy configurations (MECs) adopted by the system at $T = 0$ K using a lattice sum method [90, 91, 94]. Calculating structures at $T = 0$ means that the minimised energy is the internal energy of the system, and that any entropic effects are neglected. In order to simplify our calculations, we only consider crystal structures containing one A particle and n_B B particles in the unit cell. In this case we can define the unit cell as the parallelogram formed by neighbouring A particles which is spanned by two lattice vectors $\mathbf{a}= a(1,0)$ and $\mathbf{b}= a\gamma(\cos\phi, \sin\phi)$, where ϕ is the angle between $\mathbf{a}$ and $\mathbf{b}$ and $\gamma = b/a$ is the aspect ratio (see figure 7.7). Within this unit cell, the A particle is at $(0, 0)$ and the B particles are at $\mathbf{r}_i^B$ ($i = 1 \ldots, n_B$).

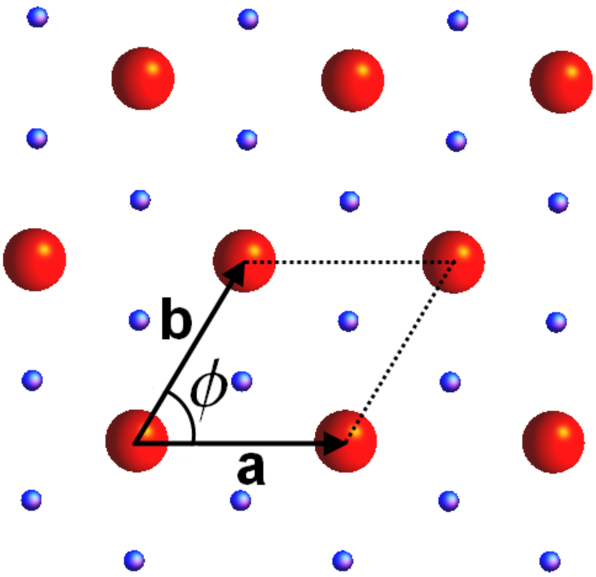

Figure 7.7: Definition of the lattice vectors **a** and **b** and angle ϕ and unit cell of the 2D binary crystal.

Given that we are working at a fixed large particle density ρ_A, the lattice constant a is fixed by the condition $|\mathbf{a} \times \mathbf{b}| = \rho_A^{-1}$ which leads to $a = (l\sqrt{3})/(2\gamma \sin\phi)$. The energy per unit cell E of such a binary crystal is given by the lattice sum [90, 91, 94]

$$\begin{aligned} E &= \frac{1}{2}\sum_{hk}{}' U_{AA}(h\mathbf{a}+k\mathbf{b}) + \frac{1}{2}\sum_{hk}{}' U_{BB}(h\mathbf{a}+k\mathbf{b}) \\ &+ \sum_{hk}\sum_{i=1}^{N_B} U_{AB}(\mathbf{r}_i^B + h\mathbf{a}+k\mathbf{b}) \\ &+ \sum_{hk}\sum_{i=1}^{N_B-1}\sum_{j=i+1}^{n_B} U_{BB}(\mathbf{r}_i^B - \mathbf{r}_j^B + h\mathbf{a}+k\mathbf{b}), \end{aligned} \tag{7.12}$$

where $U_{ij}(i,j = A,B)$ is given by eqn.(7.3) and the summations over h,k run over all integer values such that $|ha+kb| < r_c$, where r_c is the cut-off radius. In order to ensure good convergence of our results when minimising E, we chose a large cut-off radius of $r_c = 85l$. The primed summations indicate that the term $h, k = 0$ is omitted in the sum.

In order to obtain the equilibrium crystalline structure at $T = 0$ K for a given concentration ξ and dipole ratio m_B (Γ is irrelevant for $T = 0$ K since it is infinite in this case), E is minimised with respect to γ, ϕ and the positions of the B particles within the unit cell $\left\{\mathbf{r}_i^B\right\}$.

To perform the energy minimisation, we use the Powell algorithm which is equivalent to a one-dimensional search made in a sequential way along mutually conjugate (non-interfering) directions [102]. Specifically we have used a fractional tolerance $= 1 \times 10^{-6}$ in conjunction with the accepted routines for the supporting line minimisation methods [102]. We have found that the method can take from less than 1 minute and up to 60 minutes, depending on the cut-off radius of the minimisation and the starting positions of the B particles within the unit cell. Before each minimisation, we begin by assuming that $\phi = 60°$, $\gamma = 1$. To confirm that the MEC is a global minimum rather than a local minimum, we use different random initial configurations (or search vectors) for the B particles and check that they all converged on the same final state.

7.3.2 Details of Monte Carlo simulations

In order to study the thermodynamic stability of the different MEC's at finite T, we perform MC simulations (see section 3.6) of our binary colloid system using a three different starting conditions:

1. We can test the thermodynamic stability of the MECs at finite T by *using*

the MECs as the starting configuration in our MC simulations. If the binary alloy is thermodynamically stable, the particles will remain in the MEC lattice, even after a long simulation run. For these simulations we use a simulation box with the same shape as the unit cell of the MEC.

2. In order to probe the kinetic stability of the different MEC configurations, we also use starting configurations that are *partially ordered*, *i.e.* where large particles are ordered in a hexagonal lattice with the small particles randomly positioned in between. For these simulations, we also use a simulation box with the same shape as the unit cell of the MEC.
3. In order to probe the kinetic stability of the system further, we also use a starting configuration where both the large and small particles are random. For these simulations we use a square simulation box.

Specifically, MC simulations of the binary colloid system were performed in the NVT ensemble for particles interacting via the pair potential given by eqn.(7.3) with total particle numbers ranging from 1000 to 3000 (depending on stoichiometry). For selected simulations we doubled the particle number and confirmed that finite size effects were negligible. We also performed very long simulation runs (100,000 MC steps per particle) to allow the system to equilibrate. In order to efficiently sample the configuration space, we have varied our maximum trial move so that the MC acceptance of trial moves ranges between 20% and 50%, for higher and lower concentrations respectively [58].

Note that more sophisticated MC schemes exist, for example, where both the shape and the size of the simulation box are allowed to vary during the simulation [103, 104], or where MC steps involving swapping the identity of particle pairs of different species are allowed [105]. Given the very complex and rugged energy landscapes present in binary systems, the use of such schemes would be critical in accurately determining the *crystallization* behaviour of such systems starting from the disordered state. However since we are primarily interested in the *melting* behaviour of specific MEC structures starting from the ordered state, our NVT scheme suffices for the work illustrated in this Thesis. These MC simulation techniques are discussed further in section 7.6.

7.4 Behaviour of binary colloids at $T = 0$ K

In figures 7.8 and 7.9, we show the MECs we obtain for $\xi = 2/3, 3/4, 4/5, 5/6, 6/7$ and $m_B = 0.0031 \rightarrow 0.1076$. We note that the compositions $\xi = 2/3, 4/5, 6/7$ coincide with the compositions used by Fornleitner *et al.* [90, 94] while the dipole moment ratios $m_B = 0.0031, 0.01024, 0.0624, 0.1076$ coincide with the particle size ratios z used by Fornleitner *et al.* through the relationship $m_B = z^{(n+2)/2}$ with $n = 3$; the calculations for these parameters serve as a useful check for our lattice sum method.

We first consider the MECs for $\xi = 2/3, 4/5$ and $6/7$ and how these structures evolve with increasing m_B. For $\xi = 2/3$, individual B particles reside in the interstitial sites between three large A particles. This hexagonal AB_2 structure is very stable with respect to increasing m_B, though we note that for large m_B values, the small particles start to distort the hexagonal lattice of the large A particles. The stability of the hexagonal AB_2 lattice can be readily understood by considering the potential energy landscape seen by a test B particle due to a perfect hexagonal lattice of A particle which has a minima at the interstitial sites

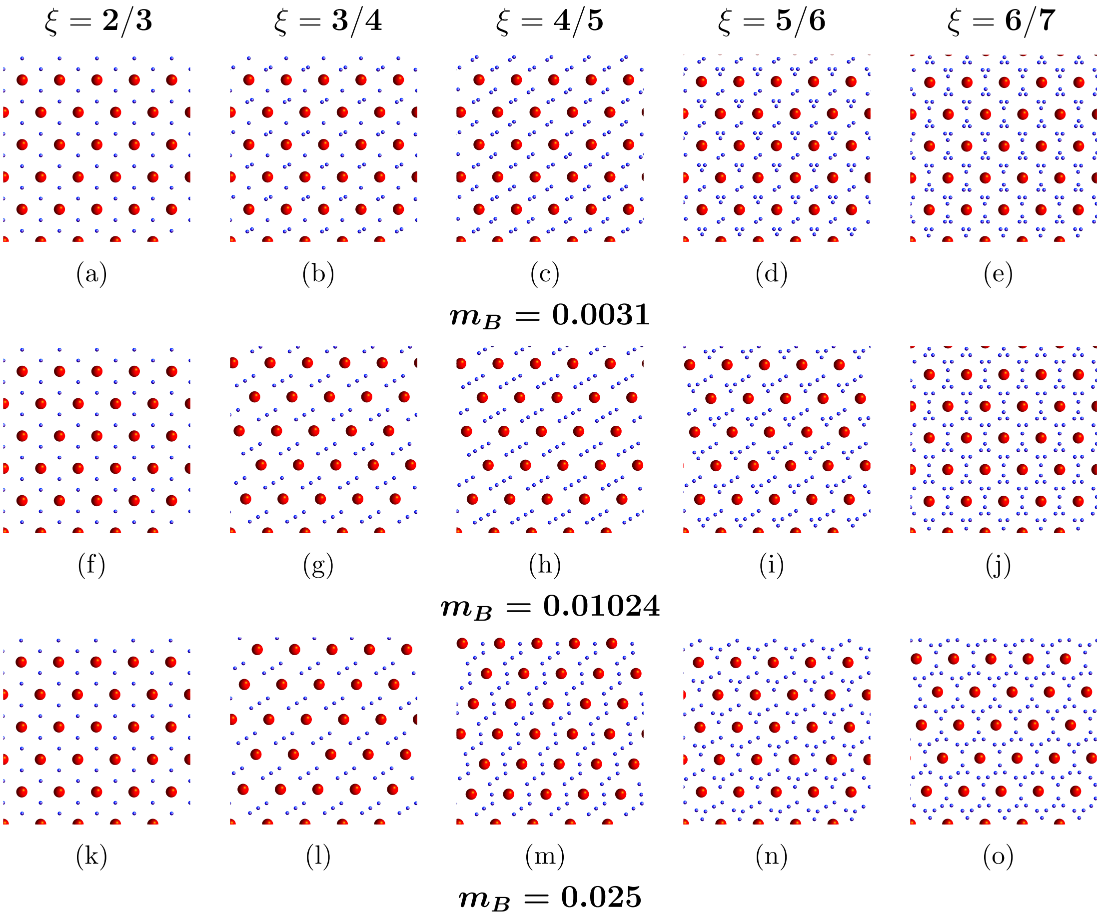

(a) (b) (c) (d) (e)

$\boldsymbol{m_B = 0.0031}$

(f) (g) (h) (i) (j)

$\boldsymbol{m_B = 0.01024}$

(k) (l) (m) (n) (o)

$\boldsymbol{m_B = 0.025}$

Figure 7.8: MECs for different ξ within the range $0.0031 \geq m_B \leq 0.025$. Note that particles are not drawn to scale.

between every three large particles (figure 7.10(a)).

For $\xi = 6/7$ and $m_B \leq 0.03703$, a hexagonal AB_6 structure is formed where clusters of three B particles reside in the interstitial sites between three large A particles. Once again this structure is relatively stable with respect to increasing m_B, though for $m_B > 0.03703$, the B particles distort the hexagonal A lattice sufficiently so that neighbouring clusters of three B particles merge into clusters of six B particles between every four A particles.

For $\xi = 4/5$, the MECs go through a much richer series of changes as we

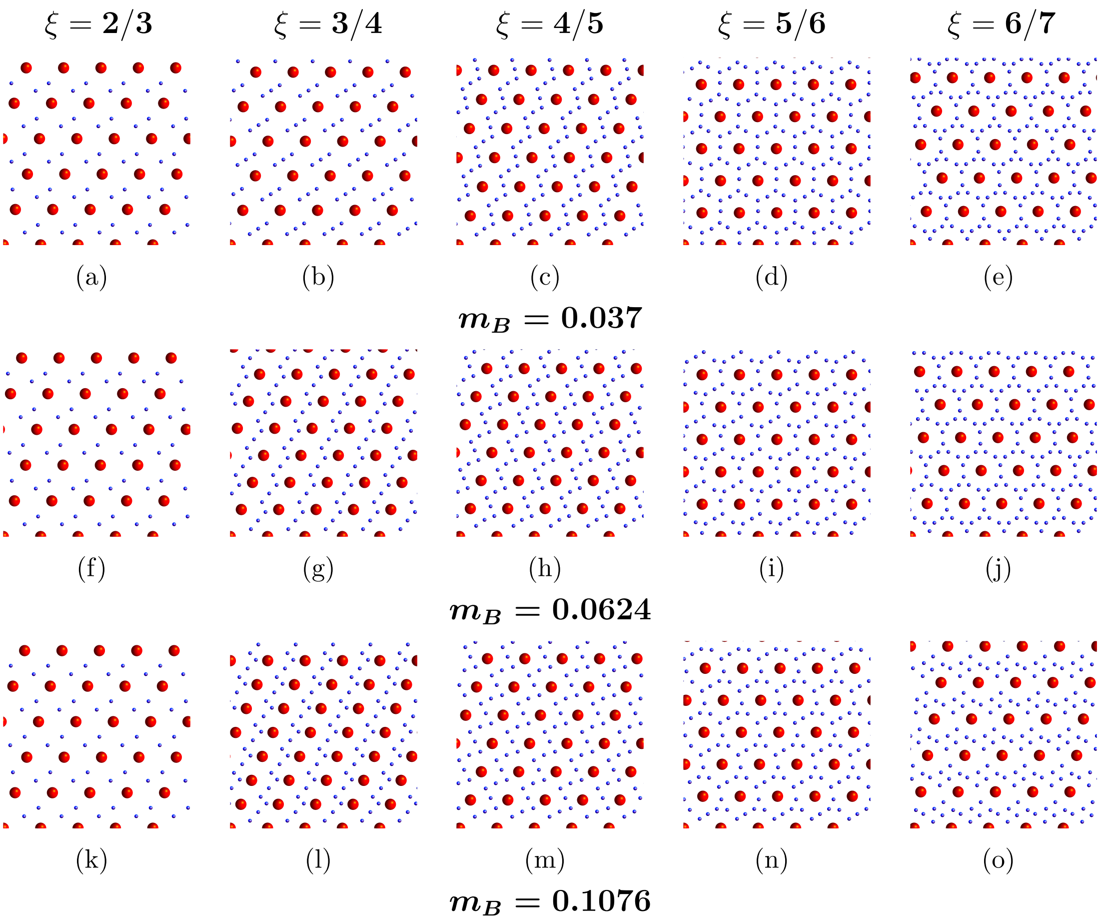

Figure 7.9: MECs for different ξ within the range $0.03703 \geq m_B \leq 0.1076$. Note that particles are not drawn to scale.

increase m_B. For $m_B = 0.0031$, the dipole repulsion between the B particles is small enough so that it is energetically favourable for clusters of two B particles to reside in the interstitial sites between three A particles. However as m_B increases to $m_B = 0.01024$, the repulsion between B particles breaks the binary clusters of B particles and cause them to merge into intriguing zigzag structures which weave through the hexagonal A lattice. As m_B increases further, the B particles start to distort the hexagonal A lattice, in the process breaking the zigzag structure into a cluster four B particles between every four A particles (figure 7.9(h)). Finally for

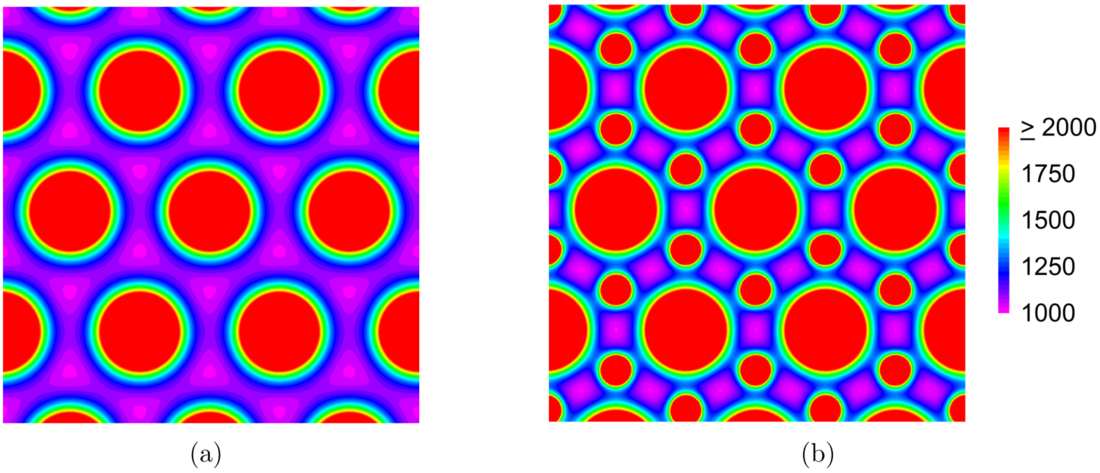

(a)

(b)

Figure 7.10: Potential energy landscape seen by a test B dipole for $m_B = 0.037$ due to (a) hexagonal A lattice and (b) hexagonal AB$_2$ lattice (arbitrary units for energy scale).

$m_B = 0.1076$, the hexagonal A lattice unexpectedly re-emerges and the interstitial sites between three A particles is now occupied in an alternating sequence by a single B particle or a cluster of three B particles. We note that the structures observed above are the same as those found by Fornleitner *et al.* [90, 94] thus validating our lattice sum calculation method. We also note that the $\xi = 2/3$ structures shown in figure 7.8 are in excellent agreement with the hexagonal AB$_2$ structures found experimentally in section 7.1 for $\xi = 2/3$. Interestingly there is a strong resemblance between the zigzag structure seen in fig.3h and the zigzag structure found experimentally in section 7.1 for $\xi \approx 3/4$. However this resemblance is almost certainly only coincidental since the two structures have significantly different m_B and ξ values: $m_B = 0.01024$, $\xi = 4/5$ in figure 7.8(h) while $m_B \approx 0.037$, $\xi \approx 3/4$ for the zigzag structure in section 7.1.

We next consider the MECs for the compositions $\xi = 3/4, 5/6$ which were not considered by Fornleitner *et al.* [90, 94] but which are specifically relevant to the experiments in section 7.1. For $\xi = 3/4$ and $m_B = 0.0031$, the dipole repulsion between the B particles is small enough so that it is energetically favourable for the interstitial sites between three A particles to be occupied in an alternating sequence by a single B and a cluster of two B particles. However as m_B increases to $m_B \geq 0.01024$, neighbouring single B particles and binary clusters of B particles merge into a cluster of three B particles lying along the long diagonal of the unit cell shown in figure 7.7. This local motif of three B particles is extremely stable and persists up to $m_B = 0.1076$. This local motif is also observed in the experimental data in section 7.1 for $\xi \approx 3/4$.

For $\xi = 5/6$, general trends for how the MECs evolve with increasing m_B are harder to make out as the MEC structures are rather complex. However for $m_B = 0.03703$, we note that the B particles arrange themselves in a highly symmetric hexagonal structure around each A particle; this structure will be considered in more detail in what follows.

Next we focus on the mid-range m_B values of $m_B = 0.025$ and $m_B = 0.03703$, which are relevant to the experiments in section 7.1 to see how the MEC structure evolves with increasing ξ. We see that for these values of m_B, the binary crystal structures obtained for the different values of ξ are essentially hexagonal. This can be seen more quantitatively in Table 7.1 where we list unit cell angles ϕ and aspect ratios γ for MECs with $m_B = 0.025$ and $\xi = 2/3, 5/6, 6/7$. In all cases, the deviation of ϕ and γ away from the hexagonal values of $\phi = 60^\circ$ and $\gamma = 1$ is very small. This is in excellent agreement with the experimental data in section 7.1 where we saw that the introduction of the small particles led to a minimal distortion of the hexagonal lattice of the large particles. The small distortions away from the hexagonal phase are a direct consequence of the small value of m_B

ξ	$2/3$	$5/6$	$6/7$
ϕ	$60.28°$	$61.30°$	$64.84°$
γ	0.9998	1.000	0.9997
T_m^*	$4.0 \pm 0.5 \times 10^{-3}$	$2.0 \pm 0.5 \times 10^{-6}$	$3.0 \pm 0.5 \times 10^{-3}$

Table 7.1: Unit cell parameters and melting temperatures for the MECs of AB_2 ($\xi = 2/3$), AB_5 ($\xi = 5/6$) and AB_6 ($\xi = 6/7$) for $m_B = 0.025$.

for our experimental system. As can be seen from figure 7.8, larger values of m_B will lead to much stronger deviations away from hexagonal symmetry.

As noted before, for $\xi = 2/3$, single B particles fully occupy all the interstitial sites between three A particles. As we increase ξ from $\xi = 2/3$ to $\xi = 5/6$, we notice that the additional B particles progressively fill the interstitial sites between *two* A particles, in excellent agreement with the experimental data in section 7.1 for $\xi > 2/3$. This behaviour can be rationalised by considering the potential energy landscape seen by a test B particle due to the A *and* B the particles in a perfect hexagonal AB_2 structure (figure 7.10(b)). We see that the presence of the B particles leads to a new potential energy minima in the interstitial sites between *two* A particles. However the simplistic analysis based on figure 7.10(b) breaks down for smaller values of m_B because it becomes energetically favourable for more than one B particle to reside in the interstitial sites between three A particles. It also breaks down for larger values of m_B since the additional B particles will significantly distort the hexagonal AB_2 structure shown in figure 7.10(b). The fact that we observe the progressive filling in of the interstitial sites between two A particles in our experiments in section 7.1 thus confirms that the experimental value of m_B is around $m_B \approx 0.03$. Finally for $\xi = 6/7$, since there are not enough interstitial sites between three and two

A particles to accommodate all the B particles, the binary crystal adopts the qualitatively different hexagonal AB_6 structure where each potential minima due to the large particles is occupied by a cluster of three B particles.

7.5 Behaviour at finite T

The previous subsection investigated the behaviour of the binary alloy at $T = 0$ K, thus neglecting any entropic effects. In this section, we study the thermodynamic and kinetic stability of the different MEC structures at finite T. This will allow us to gain a deeper understanding of the experimental structures observed in section 7.2 which were obtained at finite T. For practical reasons, we only focus on MECs with $\xi = 2/3, 3/4, 5/6, 6/7$ and $m_B = 0.025$ as these are the parameters most relevant to the experimental system in section 7.2. Note that the dipole moment ratio of $m_B = 0.025$ that we consider here is slightly lower than the value $m_B = 0.037$ considered in section 7.2.2. From figures 7.8 and 7.8, we note that the equilibrium structure of the binary colloid system is essentially the same for both m_B values. However the equilibration time of the $m_B = 0.025$ system is significantly faster computationally, we have therefore opted for the slightly lower m_B value for pragmatic reasons.

7.5.1 Stability of MEC's at finite T

While the $T = 0$ K theory above helps us explain the experimental long-range structure for $\xi = 2/3$ and local structures for $\xi = 3/4$ and $\xi = 5/6$, it is clear that the latter experimental systems do not adopt the corresponding MEC globally. One reason for the discrepancy between theory and experiment is probably due to

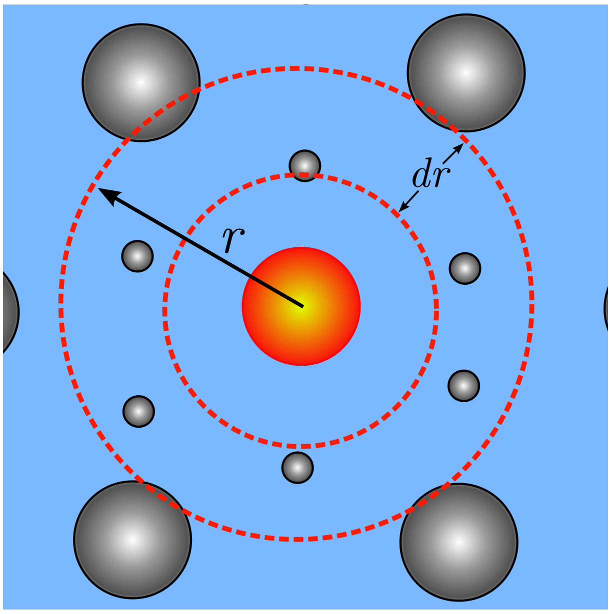

Figure 7.11: Schematic diagram illustrating the principles used in obtaining the radial distribution function between an large A and small B particle, $g_{AB(r)}$.

kinetics, namely the experimental system cannot find the MEC globally because it is stuck in local metastable states. Indeed 2D binary colloidal systems have been found theoretically to possess a very complex and rugged energy landscape [90, 92] and have also been found experimentally to be very efficient glass formers [106].

In order to study the thermodynamic stability of the different MECs at finite T, we perform MC simulations of our binary colloids using the MEC as the starting configuration. We first consider the stability of the different MEC structures at the dimensionless temperature $T^* = 1/\Gamma = 5.9 \times 10^{-4}$ (*i.e.*, $\Gamma = 1720$) which is the temperature relevant to the experiments in section 7.1. In figure 7.12, we show the final snapshots of the MC simulations for $T^* = 5.9 \times 10^{-4}$ starting from the AB_2 ($\xi = 2/3$), AB_3 ($\xi = 3/4$), AB_5 ($\xi = 5/6$) and AB_6

($\xi = 6/7$) MECs respectively. Clearly, while the AB_2 and AB_6 MECs remain stable at finite T^*, the AB_3 and AB_5 MECs are unstable. Specifically for both AB_3 and AB_5, while the A particle lattice remains stable and has long-range hexagonal order, the B particle lattice is unstable and becomes somewhat disordered, though we can discern local regions of AB_2 and AB_6 order in figures 7.12(a) and 7.12(d) respectively.

In order to characterise the final structures obtained from our MC simulations more quantitatively, in figure 7.13 , we plot the radial distribution function of B particles around any given A particle $g_{AB}(r)$ obtained from our MC simulation for $m_B = 0.025$, $T^* = 5.9 \times 10^{-9}$ and $\xi = 2/3, 3/4, 5/6, 6/7$ respectively and compare these to the corresponding results for the MEC. Here $g_{AB}(r)$ is defined as

$$g_{AB}(r) = \frac{A}{N_A N_B} \left\langle \sum_{i=1}^{N_A} \sum_{j=1}^{N_B} \delta\left(\mathbf{r} - (\mathbf{r}_i^A - \mathbf{r}_j^B)\right) \right\rangle, \tag{7.13}$$

where A is the area of the simulation box, N_A, N_B are the total number of A and B particles respectively in the simulation box and $\mathbf{r}_i^A$, $\mathbf{r}_i^B$ are the positions of the i^{th} A and B particle respectively. Clearly for both $\xi = 2/3$ and $6/7$, the $g_{AB}(r)$ peaks of the finite T structure coincide perfectly with the Bragg peaks of the MEC while the peaks for the finite T structure for $\xi = 3/4, 5/6$ do not. This confirms that the hexagonal AB_2 structure and AB_6 structure are thermodynamically stable while the hexagonal AB_3 structure and AB_5 structure are thermodynamically *unstable* at $T^* = 5.9 \times 10^{-4}$.

Interestingly, we find that the first few peaks in the finite T AB_3 and AB_5 structures follow very closely the Bragg peaks for the hexagonal AB_2 and AB_6 MECs respectively (indicated on figures 7.13(b) and 7.13(c)). One possibility

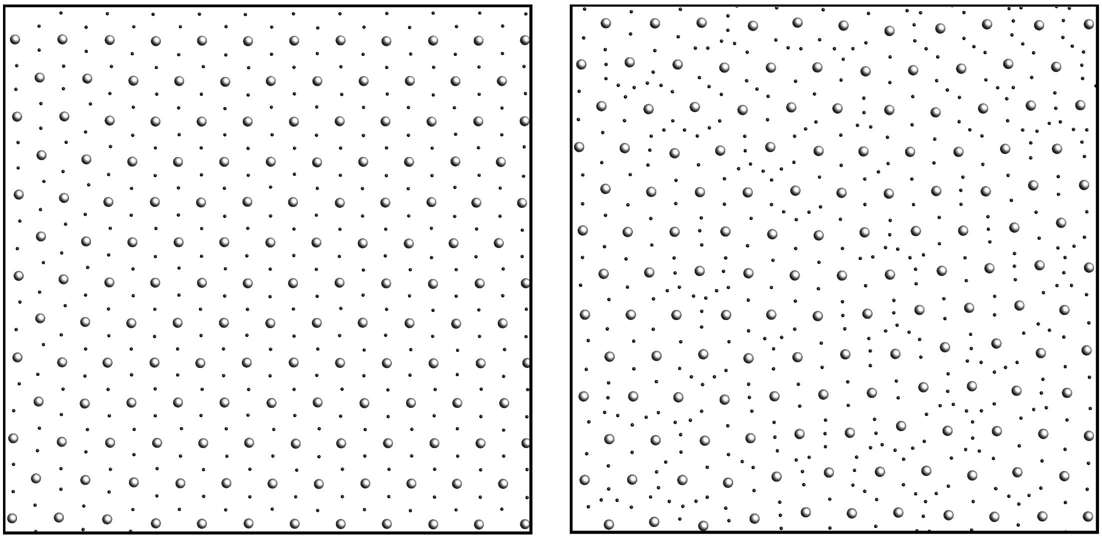

(a) AB$_2$ (b) AB$_3$

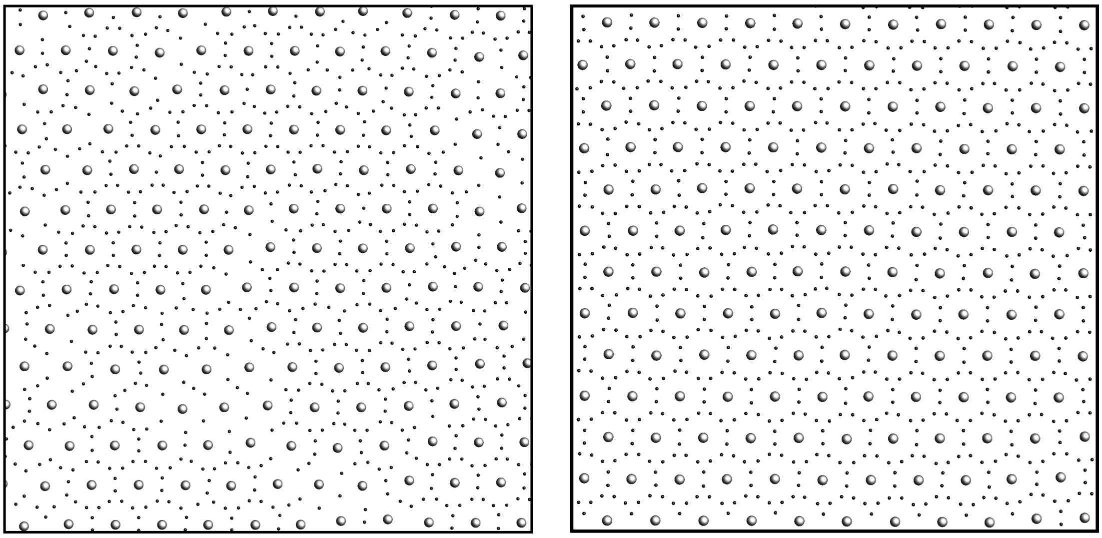

(c) AB$_5$ (d) AB$_6$

Figure 7.12: Final snapshot of MC simulations for (a) $\xi = 2/3$, (b) $\xi = 3/4$, (c) $\xi = 5/6$ and (d) $\xi = 6/7$ for $\Gamma = 1720$ and $m_B = 0.025$ when starting from their respective MECs.

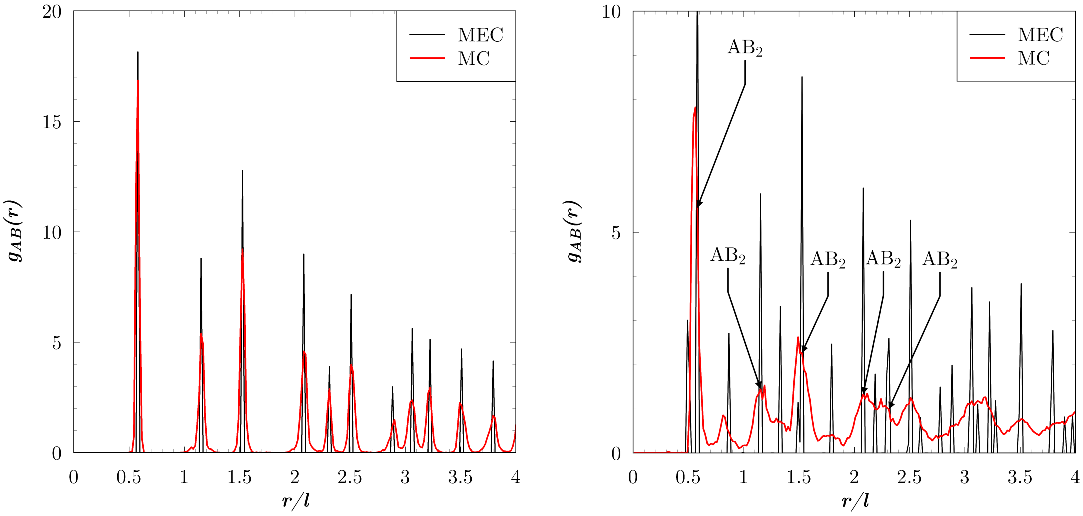

(a) AB_2 (b) AB_3

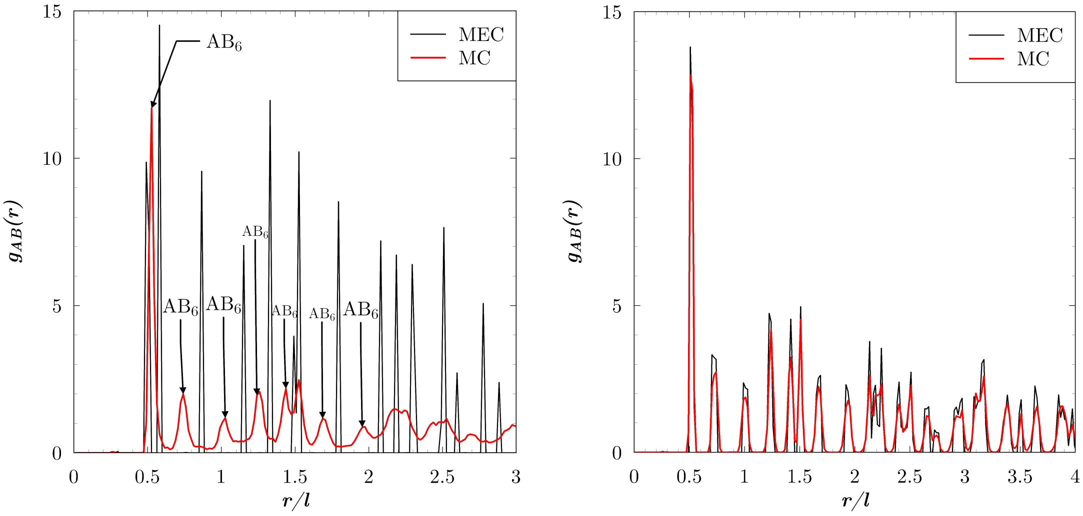

(c) AB_5 (d) AB_6

Figure 7.13: Radial distribution function $g_{AB}(r)$ plots comparing the MEC with the MC results for the (a) AB_2, (b) AB_3, (c) AB_5 and (d) AB_6 systems with the MC parameters $\Gamma = 1720$ and $m_B = 0.025$. In figures (b) and (c) we have indexed the MC peaks with those that correlate to predicted AB_2 and AB_6 positions, respectively.

for this intriguing observation is that macroscopic phase separation may have occurred in our system where one of the phases is in the AB_2 or AB_6 crystalline phase. However from the snapshots for both the AB_3 ($\xi = 3/4$) and AB_5 ($\xi = 5/6$) systems in figures 7.12(b) and 7.12(c), we could not discern any evidence for macroscopic phase separation occurring. The results in figures 7.13(b) and 7.13(c) therefore suggests that the *local* structure in the finite T AB_3 and AB_5 binary systems is closer to that of the AB_2 and AB_6 MECs respectively, in excellent agreement with our observations from the final MC snapshots in figures 7.12(b) and 7.12(c). Obviously stoichiometry dictates that there can be no *long-range* AB_2 and AB_6 order in these snapshots, as is also clear from the systems in figures 7.12(a) and 7.12(d).

7.5.2 Melting transition of MEC structures

Both the thermodynamic stability of the AB_2 and AB_6 MECs at finite T and the presence of short range AB_2 and AB_6 order in the finite T AB_3 and AB_5 structures suggest that the B sub-lattice in the AB_2 and AB_6 MECs have a significantly higher melting temperature compared to in the other MECs we have studied. This is in good agreement with the MD simulations presented by Stirner and Sun [92]. In order to confirm this observation quantitatively, in what follows we will determine the melting temperature of the B sub-lattice in the binary systems above.

For one component crystals in 2D, a number of criteria exist for determining the melting point [107] including (a localised version of) the Lindemann criterion [108], the Hansen-Verlet criterion [109] and the Löwen-Pahlberg-Simon criterion

[110] which is a dynamic criterion based on the ratio of long-time and short-time diffusion constants. In addition, the celebrated theory of Kosterlitz, Thouless, Halperin, Nelson and Young (KTHNY) [111, 112, 113, 114] predicts that a third phase, the *hexatic* phase which has short range translational order and quasi-long-range orientational order exists between the crystal and isotropic phases. The melting transition of the hexatic phase can be monitored via an orientational order parameter. Unfortunately, since we are interested in the melting transition of a sub-lattice within a *two* component crystal, it is not clear how to apply any of the above criterion to determine the melting point. We have also explored other structural descriptors, such as Voronoi cell counting, but these also failed to produce a clear indication of the melting transition. For this reason, we will determine the melting temperature using a direct method, where we calculate the radial distribution function of the binary crystal for a series of T^* values around the melting transition and determine the melting temperature of the sub-lattice from the temperature where the Bragg peaks associated with the sub-lattice disappear. Since we are primarily interested in the melting of the B sub-lattice here, the obvious radial distribution function to use for this analysis is $g_{BB}(r)$ which measures the correlations between the *small* particles only.

In figure 7.14, we plot the $g_{BB}(r)$ vs T^* data for AB$_2$, AB$_5$ and AB$_6$ respectively as contour plots and $g_{BB}(r)$ plots, where the latter illustrates $g_{BB}(r)$ for three different T^*; the lowest, the melting (T^*_m) and the highest reduced temperatures. Note that since $g_{BB}(r)$ varies relatively slowly with T^* for a given r, we only needed to calculate $g_{BB}(r)$ for a relatively small number of T^* values (approximately 12 values per system) and obtain $g_{BB}(r)$ at intermediate T^* values via interpolation. For clarity we have also indicated the Bragg peak positions

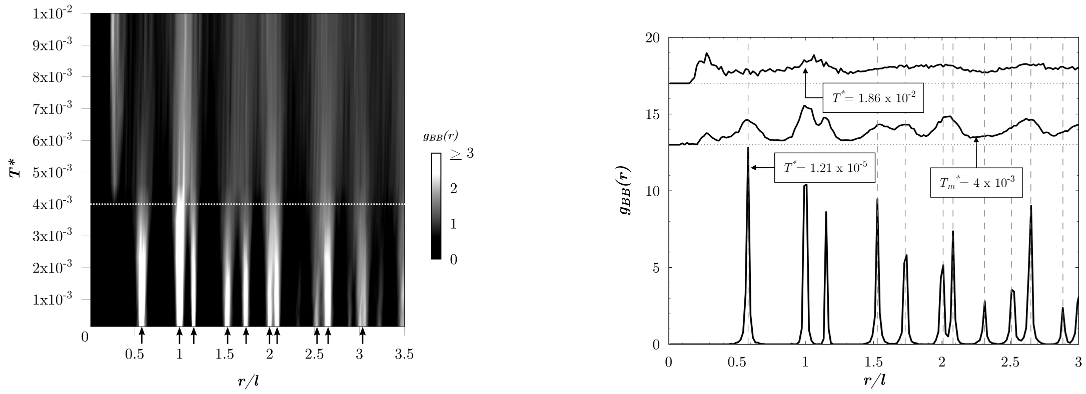

(a) AB$_2$ (b) AB$_2$

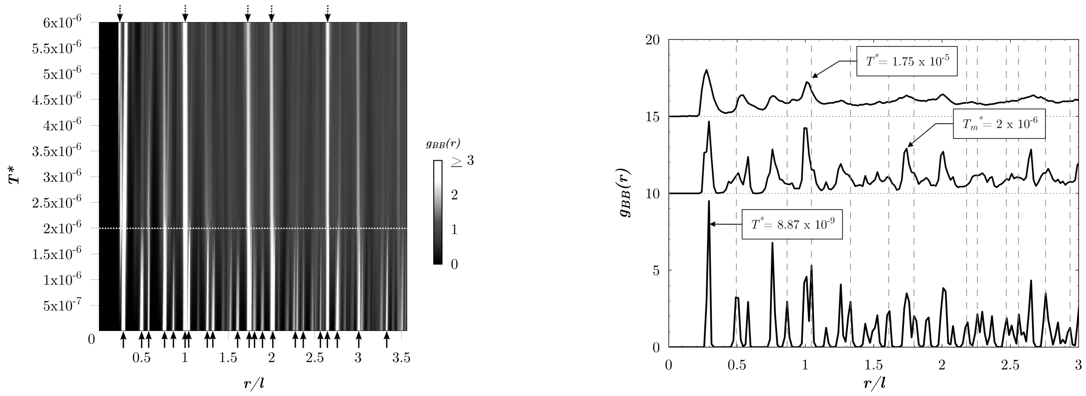

(c) AB$_5$ (d) AB$_5$

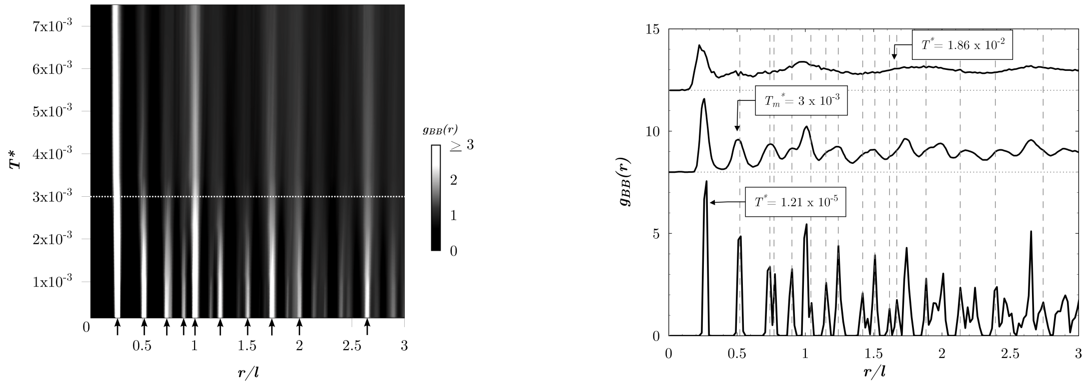

(e) AB$_6$ (f) AB$_6$

Figure 7.14: (a), (c) and (a) show contour plots of the radial distribution function $g_{BB}(r)$ vs. T^* calculated from our MC simulations for $m_B = 0.025$. The Bragg peak positions for the corresponding MECs are indicated by arrows on the x axis of each plot and the proposed melting transition is shown by the dashed line. For (c), the Bragg peaks corresponding to the AB$_6$ MEC are shown by the dashed arrows above the contour plot. Note that the T^* scale in (c) is 3 orders of magnitude smaller than those in (a) and (e). Panels (b), (d) and (f) illustrate $g_{BB}(r)$ for the AB$_2$, AB$_5$ and AB$_6$ systems at the lowest, melting (T^*_m) and highest studied T^* in MC simulations respectively, where the vertical dashed lines highlight the Bragg peaks that have become blurred or disappeared between the lowest and melting temperatures (T^*_m). The top two $g_{BB}(r)$ on (b), (d) and (f) have been shifted in the y direction for clarity.

of the corresponding MEC for each contour plot. From both the contour and $g_{BB}(r)$ plots in figure 7.14, it is clear that above a critical temperature, there is a qualitative change in the $g_{BB}(r)$ peak structure for all the binary systems. Specifically for AB_2, at around $T^* \approx 4 \times 10^{-3}$ the Bragg peaks drop in height and broaden in width. Indeed at this point, many neighbouring pairs of Bragg peaks merge into a single broad peak and a new liquid-like broad peak at around $r/l = 0.3$ emerges. These qualitative changes in $g_{BB}(r)$ allow us to unambiguously determine the melting point of the B sub-lattice for AB_2 to be $T_m^* = 4 \pm 1 \times 10^{-3}$. For AB_6, similar changes in the Bragg peaks occur at a slightly lower temperature allowing us to determine the melting temperature of the B sub-lattice to be $T_m^* = 3.0 \pm 0.5 \times 10^{-3}$ for this system. We note however that for AB_6, the height of the primary peak does not drop significantly at $T^* = 3 \times 10^{-3}$; this can be seen more clearly from the $g_{BB}(r)$ plot figure 7.14(f). This shows that the height of the primary peak is not always the most accurate measure of order in a binary system.

The change in the Bragg peak structure with increasing T^* is even richer for the AB_5 system. Specifically, at around $T^* \approx 2 \times 10^{-6}$, some of the AB_5 MEC Bragg peaks end abruptly. The disappearance of these AB_5 Bragg peaks is clearly shown by figure 7.14(c) and 7.14(d) and allows us to determine the melting temperature of the B sub-lattice to be $T_m^* = 2 \pm 0.5 \times 10^{-6}$ for this system. For $T^* > 2 \times 10^{-6}$, there is a gradual transformation of the remaining peaks into the Bragg peaks for the AB_6 MEC (also indicated on figure 7.14(c) by the dashed arrows). The melting of the AB_5 system into a phase with (local) AB_6 order seen here is consistent with our earlier results for the radial distribution function of the AB_5 system in figure 7.13(c) which were obtained at the much higher temperature of $T^* = 5.9 \times 10^{-4}$. In particular, the results of figure 7.13(c) suggest that the local AB_6 order observed in figure 7.14(c) remains stable for temperatures up to $T^* \approx 6 \times 10^{-4}$. Presumably, these local regions of AB_6 order will melt at the even higher temperature of $T^* \approx 3 \times 10^{-3}$, the melting temperature for the AB_6 MEC that we determined earlier.

We note that the melting temperatures of the B sub-lattice for AB_2 and AB_6 ($T^*_m \approx 3 \rightarrow 4 \times 10^{-3}$) are over three orders of magnitude higher than that of AB_5 ($T^*_m \approx 2 \times 10^{-6}$). This unexpectedly large difference suggests that for relatively small values of m_B which do not significantly perturb the hexagonal lattice structure of the large particles, the super-lattice structures with the highest thermal stability are those where there is single or triple occupation by the small particles at or around the potential energy minima created by the large particles (see figure 7.10(a)).

We can also estimate the melting temperature of the A sub-lattice from melting temperature for 2D one component dipolar system of A particles which was found from previous studies to be $T^* = 0.11$ [31] (defining the interaction parameter Γ and hence T^* in terms of $l = (\sqrt{3}\rho_A/2)^{-1/2}$ instead of $l = (\pi\rho_A)^{-1/2}$). Note that from ref.[31], the melting temperature of the hexagonal crystal ($T^* = 0.11$) is extremely close to the melting temperature of the hexatic phase ($T^* = 0.12$). We note that these temperatures are even higher than the melting temperature of the AB_2 and AB_6 B sub-lattice.

This hierarchy of melting temperatures suggests that the melting transition of 2D binary colloidal crystals proceeds via a multi-stage process. For example for AB_2 and AB_6, the super-lattice structure first melts into a semi-disordered phase where the A particles have long-range hexagonal order while the B particles are disordered, then into an isotropic phase where both A and B are disordered. On the other hand, for AB_5, the super-lattice structure first melts into a semi-disordered phase with local AB_6 order, then into a semi-disordered phase where the B particles are disordered, then finally into an isotropic phase where both A and B are disordered. In addition, the melting of the A sub-lattice in the above systems presumably follows KTHNY theory [111, 112, 113, 114] which involves a further two (second order) phase transitions, *i.e.*, hexagonal A → hexatic A → isotropic A. However recent studies of binary dipolar colloids in the *isotropic* phase have found that the interactions with the large particles lead to a clustering of the smaller particles [115]; it is conceivable that this clustering phenomenon will have an impact on the KTHNY melting process of the A sub-lattice. Unfortunately a detailed study of the melting transition of the A sub-lattice lies beyond the scope of this current paper but this could be a fruitful avenue for future research. Clearly the melting behaviour of 2D binary colloidal systems is richer even compared to the melting transition of 2D one component colloidal systems.

7.5.3 Metastability in binary system

As already discussed, previous theoretical studies have shown that 2D binary colloidal systems possess a very complex and rugged energy landscape [92, 90, 91, 94]. This suggests that even if an MEC is thermodynamically stable, if we start from an initial configuration that is different to from the MEC, the binary colloidal system may not be able to find the MEC state (*i.e.* the global minimum) because it is trapped in a locally metastable state en-route. This issue is of

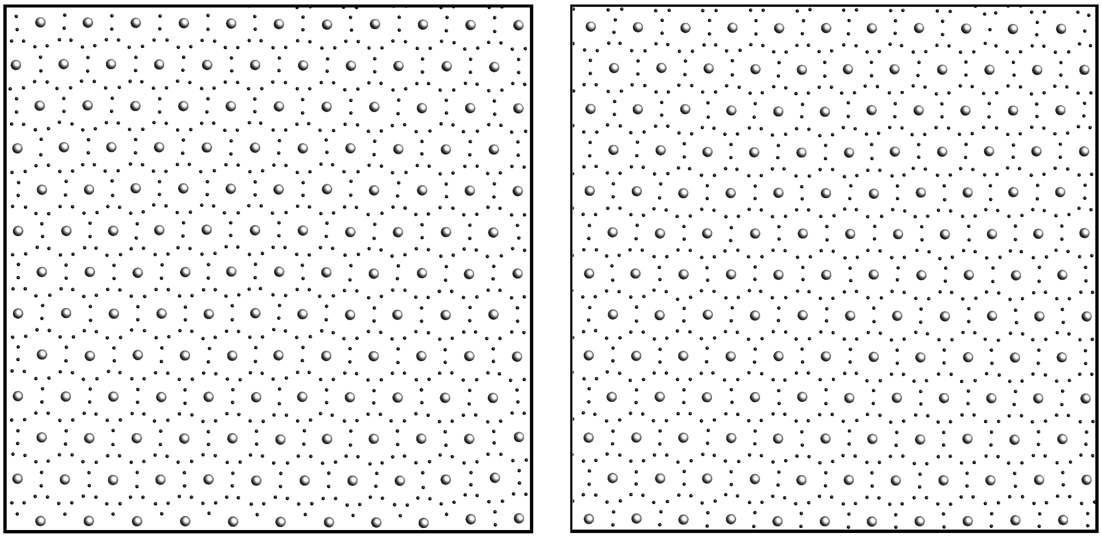

(a) Ordered

(b) Partially ordered

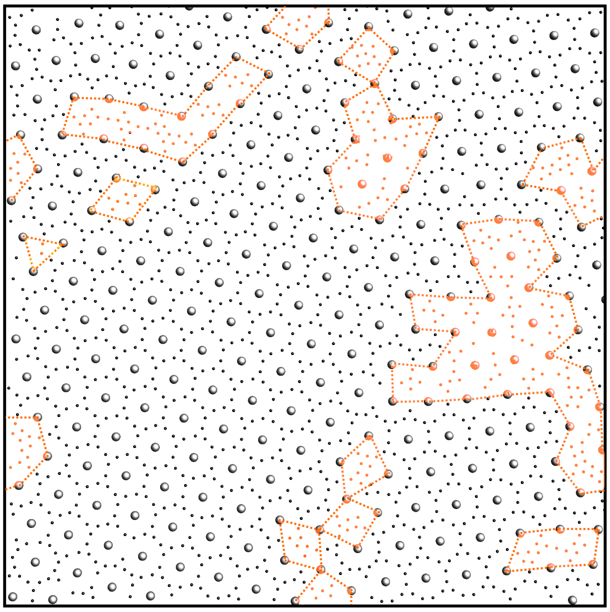

(c) Completely random

Figure 7.15: AB_6 system final snapshots, beginning from (a) ordered, (b) partially ordered and (c) random initial configurations. Glassy states are shown by the orange regions in (c).

practical importance since experimentally, the 2D binary colloidal structures were prepared from random or semi-random starting configuration. Indeed 2D binary colloidal systems have been found experimentally to be very efficient glass formers [106].

In order to study how the complex energy landscape in binary colloids affects the crystallisation of the thermodynamically stable MEC structures considered in previous subsections, we perform MC simulations starting from a partially ordered state (*i.e.* large particles ordered, small particles random); the configuration effectively mimics the experimental procedure for the preparation of the binary structures presented in section 7.2 (see appendix D). We will also conduct simulations beginning from a completely random state (*i.e.* all particles randomly placed); this is the same starting configuration used by Stirner and Sun in their MD study of binary colloids [92]. Once again, we use $m_B = 0.025$ and $\Gamma = 1720$ to allow for a direct comparison with the results presented in section 7.5.1 which were obtained using the MEC as the starting configurations.

In figure 7.15, we present the final snapshots of the $\xi = 6/7$ system starting from our three designated starting conditions. Recall that the MEC for $\xi = 6/7$, $m_B = 0.025$ is thermodynamically stable at $\Gamma = 1720$. We can see from figure 7.15(b) that starting from the partially ordered state we obtain the MEC state (cf. figure 7.15(a)). However, if all particles are completely random at the start of the simulation, it is evident from figure 7.15(c) that we no longer obtain the MEC structure. To emphasise this fact, we have highlighted in orange the defect regions in figure 7.15(c) *i.e.*, the regions that do not exhibit the characteristic AB_6 structure as seen from the MEC results.

The results shown in figure 7.15 suggest that the ordering of the large A

MC concentration (crystal)	Ordered (%)	Partially ordered (%)	Random (%)
2/3 (AB_2)	100.0 ±0	69.7 ±2.4	26.8 ±3.7
6/7 (AB_6)	100.0 ±0	100.0 ±0	30.0 ±2.1

Table 7.2: Unit cell counting summary for $\xi = 2/3$ and $6/7$ for all three designated MC starting conditions. The error measurements have been calculated from the standard deviation of three separate MC runs for each test.

particles plays a critical role in ordering the small B particles. Presumably this is because the ordering of the large particles generates the potential energy landscape shown in figure 7.10 which 'funnels' the small particles into occupying the potential energy minima. We can extend our analysis further for $\xi = 6/7$ by using a *unit cell counting* algorithm to count the percentage of unit cells within the simulation box that (in this case) contain 6 small particles within the unit cell, that is madeup of four neighbouring A particles (see figure 7.7). This provides us with a measure of *'order'* within the simulation box. In table 7.2, we present the results of the number of cells exhibiting either AB_2 or AB_6-like unit cells for $\xi = 2/3, 6/7$, respectively. We have also analysed the AB_2 structure because this system was also determined to be thermodynamically stable for $\Gamma = 1720$ (see section 7.5.2). We see that both structures exhibit a drop in the degree of order as the randomness of the initial starting configuration within the MC simulations is increased. From Table 7.2, the $\xi = 6/7$ composition has a higher degree of order compared to $\xi = 2/3$ for the partially ordered starting configuration. This is most likely due to the fact that the $\xi = 6/7$ system has less available space for the small particles to move in compared to the $\xi = 2/3$ system. However both compositions experience significant drop in the degree of order when a random starting configuration is used. It is important to note that the results listed in Table 7.2 are calculated for very long MC simulation runs, *i.e.* $\approx 300,000$ MC steps per particle, in order to maximise the opportunity for the system to equilibrate to the global minimum.

From these tests, we see that the ordering of the B particles is primarily controlled by the ordering of the large A particles. In addition, we see that the higher value of Γ used here appears to create large potential energy barriers between local minima, leading to the binary colloid system being trapped in metastable states.

7.6 Summary and future work

We have studied theoretically the structure and melting transition of experimentally realised two-dimensional (2D) binary mixtures of dipolar colloids. Using a lattice sum method, we have found that for $T = 0$ K, the system forms a rich variety of stable crystalline phases whose structure depends on the small particle number fraction ξ and dipole moment ratio m_B of the system. In particular for m_B values relevant to those used in the experiments presented in section 7.1, our lattice sum method predicts that with increasing ξ, the B particles first fill the interstitial sites between three A particles followed by the interstitial sites between *two* A particles, in excellent agreement with the experiments in section 7.1. Using Monte Carlo (MC) simulations, we also found that the melting behaviour of the different $T = 0$ K structures was unexpectedly rich. For example, using a direct analysis of radial distribution function for small particles $g_{BB}(r)$ versus temperature data, we were able to show that the melting temperature of hexagonal AB_2 and AB_6 phases is three orders of magnitude higher than that of hexagonal AB_5. These results suggest that for relatively small values of m_B which do not significantly perturb the hexagonal lattice structure of the large particles, the super-lattice structures with the highest thermal stability are those where there is single or triple occupation by the small particles at or around the potential energy minima created by the large particles. We also found that the melting transition for our binary colloidal system proceeds via at least two stages for hexagonal AB_2 and AB_6 and at least three stages for hexagonal AB_5. For example the AB_5 super-lattice first melts into a semi-disordered phase with local AB_6 order, then into a semi-disordered phase where the B particles are disordered, then finally into an isotropic phase where both A and B are disordered. The presence of the B particles may also modify the melting of the A sub-lattice. The details of this modification are however at present unknown but could be a fruitful avenue of future research. The melting behaviour of 2D binary colloidal systems is thus richer even compared to the melting transition of 2D one component colloidal systems.

Finally we have investigated how the complex energy landscape of our binary colloidal system affects the crystallisation kinetics of binary colloid systems. We find that the degree of order in the final state depends strongly on the starting configuration. In particular we find that the degree of order is significantly higher for a partially ordered starting configuration (where the large particles are ordered) compared to a random starting configuration. This suggests that the ordering of the large particles plays a critical role in ordering the small particles.

For future work, it would be beneficial to investigate the order-disorder transition further for 2D binary colloidal systems. In particular, the method outlined by Bresme *et al.* [105] of swapping particle identities could provide an insight into this. For example, an MC move is modified so that the identity of the particle is swapped (*i.e.* between species) according to the Metropolis criteria, for a particle concentrations at their crystallisation point (*i.e.* at the point where particle displacements are at a minimum). This has been successfully applied in a previous study [105] to solid phases of the restricted primitive model and has predicted a new phase indicating a new triple point for the system in question. In addition, it would be interesting to see how an increase in small particle numbers per unit cell would affect apparent stability of the triple occupation of the potential energy well and in general, the binary crystal phases as a whole.

Appendix A

Numerical Fourier transforms in two-dimensions

All inversion methods described in chapters 3, 4 and 5 require the use of correlation functions that continuously change from real r space to the frequency domain q in order to fully utilise the properties of the OZ equations (eqns.(3.9) and (3.12)). We implement our numerical Fourier and inverse Fourier transforms using the excellent approximation given by Lado [63]. For an arbitrary function F, the 2D Fourier transform (that inevitably is a Hankel transform) can be performed numerically using

$$F(q_j) = \frac{4\pi}{Q^2}\sum_{i=1}^{N-1} F(r_i)\frac{J_0\left(q_j r_i\right)}{\left[J_0'\left(Q r_i\right)\right]}, \tag{A.1}$$

with

$$\begin{aligned} r_i &= \mu_i/\mu_N, & \text{(A.2)} \\ q_j &= \mu_j/R, & \text{(A.3)} \end{aligned}$$

where R and Q are the full ranges for r and q, $J_0(x)$ is the zeroth-order Bessel function, $J_0(x)' = -J_1(x)$, with $J_1(x)$ being the Bessel function of the first kind, and μ_i are the positive roots of $J_0(x)$.

The inverse Fourier transform of a 2D function is performed by implementing the following expression

$$F(r_i) = \frac{1}{\pi R^2} \sum_{j=1}^{N-1} F(q_j) \frac{J_0\left(q_j r_i\right)}{\left[J_0'\left(q_i R\right)\right]}. \tag{A.4}$$

The above equations ensure that the orthogonality of the Fourier expansions is retained.

Appendix B

HMSA expressions

In order to avoid singularities in $u(r)$ at $r = 0$ in our numerical calculations when using the HMSA method, it is more convenient to work with $w(r) = \exp(-\beta u(r) + \beta u(r_m))$ instead of directly with the potential $\beta u(r)$ for the region $r \leq r_m$. Rewriting the relevant equations in section 4.2.2 in terms of $w(r)$ instead of $\beta u_1(r)$, eqn.(4.24) (for $r \leq r_m$) becomes

$$w(r) = \frac{\hat{g}(r)}{h(r) + 1}. \tag{B.1}$$

On the other hand, inserting eqn.(4.20) into eqn.(4.29) and using $w(r)$ instead of $\beta u_1(r)$, eqn.(4.29) becomes

$$\begin{aligned}\frac{\partial\beta P}{\partial\rho} = 1 \quad &+ \quad \pi\rho\int_0^{r_m} r^2dr\left(1+\frac{\exp\left[f(r)(\gamma(r)-\beta u(r_m))\right]-1}{f(r)}\right)\frac{dw(r)}{dr} \\ &+ \quad \pi\rho\int_{r_m}^{\infty} r^2dr\left(1+\frac{\exp\left[f(r)(\gamma(r)-\beta u(r))\right]-1}{f(r)}\right)\frac{d\beta u(r)}{dr} \\ &+ \quad \frac{\pi\rho^2}{2}\int_0^{r_m} r^2dr\exp\left[f(r)(\gamma(r)-\beta u(r_m)\right]\frac{\partial\gamma(r)}{\partial\rho}\frac{dw(r)}{dr} \\ &+ \quad \frac{\pi\rho^2}{2}\int_{r_m}^{\infty} r^2dr\exp\left[f(r)(\gamma(r)-\beta u(r)\right]\frac{\partial\gamma(r)}{\partial\rho}\frac{d\beta u(r)}{dr}.\end{aligned} \tag{B.2}$$

The inversion now proceeds as described in section 4.2.2 but using the above equations in place of their corresponding equations in chapter 4.

Appendix C

Experimental details of the system used for inversion

Here we present the experimental system we intend to invert courtesy of Dr. Pietro Cicuta and Dr. Armando Maestro of the Cavendish Laboratory, Cambridge University. The system is an oil-water interface that has been created using *n-decane* (Across Organics, 99% of purity) and Ultrapure water (Elga). All the polar components were removed from the decane by the process of adsorption onto aluminium oxide powder. Charged stabilised polystyrene particles (PS) were obtained from *Fluka* that are 2μm in diameter. The particle surface was negatively charged due to the presence of sulfate groups binding at the particle surface. The interface was prepared by the method of depositing the decane sub-phase onto the water phase. Finally the PS particles were diluted in a Methanol-water (at a ratio of 1:1) mixture to create a spreading solution, this was added directly to the interface to create the monolayer. After methanol evaporation, equilibration times of a least 30 minutes were required before the image of the interface was recorded. To study the influence of the ionic strength in the water phase on the interaction between the PS particles, different concentrations of a sodium chloride (NaCl) were systematically varied from 0mM, 0.05mM to 0.5mM in the aqueous sub phase.

A confocal microscope from *Leica* with the 10x Dry HP-PL fluotar objective with a numerical aperture of 0.30 was used to observe the motion of the interfacial particles, recording at a frame rate of 16.67 frames per second. The spatial resolution of each image is fixed at 512 × 512 pixels. Using an image analysis software, the positional co-ordinates of each particle were captured which could then be used in the calculation of the required distribution functions for the inversion methods.

Appendix D

Binary colloidal monolayers: Experimental details

Here we present details of the experimental binary system featured in chapter 7, courtesy of Dr. Tommy S. Horozov of the Department of Chemistry, University of Hull.

D.1 Particles and their hydrophobisation

Synthetic amorphous silica particles with diameters $1.00 \pm 0.05\mu m$ and $3.00 \pm 0.05\mu m$ were purchased from Tokuyama Corp., Japan. The particles were hydrophobized by silanization of their surfaces to the maximum extent following the procedure described previously [100]. The silanising agent used was dichlorodimethylsilane (DCDMS, +99.5%, Fluka AG) dissolved in dry cyclohexane (99.7%, Prolabo, for UV spectroscopy) at a concentration of 0.1 M. The modified particles were very hydrophobic since their contact angle determined at the octane-water interface by the procedure described in ref.[100] was 150 ± 3°.

One component and mixed monolayers were formed by spreading particles at the octane-water interface in the following way. A small Petri dish with diameter 2 cm and height 0.7 cm was placed in the center of larger dish with diameter 6cm and height 3cm. The smaller one was filled with deionized water obtained from a Milli-Q purification unit (Millipore) and the water surface was made at by sucking part of the water out. n-octane(99%, Lancaster) was then added in the larger Petri dish until a layer of octane with thickness 2-3mm was formed on the top of the water phase. We have found that this configuration largely suppressed the lateral drift of the particles due to convection. The spreading suspension was prepared by mixing silica particles with 70wt% aqueous solution of isopropyl alcohol (99.995%, Fisher) and subsequent sonication in a ultrasonic bath for 10min. Then a small amount of suspension $(1 - 50\mu l)$ containing about 1 - 4wt% particles was injected close to the octane-water interface. The monolayers were observed from above in transmitted light with an Optiphot 2 microscope (Nikon) fitted with a CCD camera. The images were recorded by VCR and processed with Image-Pror Plus software. Prior to the experiments the oil was passed 5 times through basic alumina (BDH, grade I for chromatographic analysis) in order to remove polar impurities. All experiments were performed at room temperature (24 ± 1°C).

D.2 Formation and observation of the monolayers

The very hydrophobic nature of the particles resulted in hexagonally ordered one component monolayers of both large and small particles at large separations (see figure 7.1). The mixed monolayers reported in section 7.1 were prepared by spreading the large particles first, thus forming a well ordered one component monolayer. Then small portions of small particles were spread over the existing monolayer, thus varying the fraction of small particles in the mixed monolayer ξ while keeping the number density of the large particles constant. However in some experiments, an alternative procedure for making the mixed monolayers in one step was used. Binary mixtures of large and small particles in 70wt% isopropanol were prepared in advance and then spread at the octane-water interface. Both procedures gave similar results, but the first one had the advantage that the composition of the mixed monolayer was easily varied. Mechanical vibrations with a frequency of 3-10 Hz applied directly to the liquid interface for several minutes after the formation of the mixed monolayer have improved its homogeneity.

References

[1] B. P. Binks and T. S. Horozov, *Colloidal Particles at Liquid Interfaces*, chapter 1, pp. 1–76, Cambridge University Press, Cambridge, 2006.

[2] F. Bresme and M. Oettel, *Journal of Physics: Condensed Matter* **19**, 413101 (2007).

[3] B. P. Binks, *Current Opinion in Colloid & Interface Science* **7**, 21 (2002).

[4] W. Ramsden, *Proceedings of the Royal Society in London* **72**, 156 (1903).

[5] S. U. Pickering, *Journal of the Chemical Society* **91**, 2001 (1907).

[6] C. N. Likos, *Physics Reports* **348**, 267 (2001).

[7] J. Israelachvili, *Intermolecular and Surface Forces*, Academic Press, London, 1992.

[8] P. Pieranski, *Physical Review Letters* **45**, 569 (1980).

[9] F. H. Stillinger, *Journal of Chemical Physics* **35**, 1584 (1961).

[10] A. J. Hurd, *Journal of Physics A: Mathematical and General* **18**, 1055 (1985).

[11] R. Larson, *The Structure and Rheology of Complex Fluids*, Oxford University Press, 1999.

[12] T. Terao and T. Nakayama, *Physical Review. E* **60**, 7157 (1999).

[13] R. Aveyard, J. H. Clint, D. Nees, and V. N. Paunov, *Langmuir* **16**, 1969 (2000).

[14] R. Aveyard, B. P. Binks, J. H. Clint, P. D. I. Fletcher, T. S. Horozov, B. Neumann, V. N. Paunov, J. Annesley, S. W. Botchway, D. Nees, A. W. Parker, A. D. Ward, and A. N. Burgess, *Physical Review Letters* **88**, 246102 (2002).

[15] J. Sun and T. Stirner, *Journal of Chemical Physics* **121**, 4292 (2004).

[16] T. S. Horozov and B. P. Binks, *Colloids and Surfaces A: Physicochemical and Engineering Aspects* **267**, 64 (2005).

[17] D. Frydel, S. Dietrich, and M. Oettel, *Physical Review Letters* **99**, 118302 (2007).

[18] K. Masschaele, B. J. Park, E. M. Furst, J. Fransaer, and J. Vermant, *Physical Review Letters* **105**, 048303 (2010).

[19] E. M. Furst, J. Vermant, and B. J. Park, *Soft Matter* **6**, 5237 (2010).

[20] P. Kralchevsky, K. Danov, and N. Denkov, *Surface and Colloid Chemistry*, chapter 11, pp. 333–494, CRC Press, New York, 1997.

[21] R. Hunter, *Foundations of Colloid Science*, Clarendon Press, Oxford, 1986.

[22] I. D. Dzyaloshinskii, E. M. Lifshitz, and L. P. Pitaevskii, *Soviet Physics Uspekh* **4**, 153 (1961).

[23] J. Fernández-Toledano, A. Moncho-Jordá, F. Martínez-López, and R. Hidalgo-Álvarez, *Theory for Interactions between Particles in Monolayers*, chapter 3, pp. 108–151 in *Colloidal Particles at Liquid Interfaces*, Binks and Horozov (eds.), Cambridge University Press, Cambridge, 2006.

[24] P. a. Kralchevsky and K. Nagayama, *Langmuir* **10**, 23 (1994).

[25] M. Oettel and S. Dietrich, *Langmuir* **24**, 1425 (2008).

[26] H. Lehle, M. Oettel, and S. Dietrich, *Europhysics Letters* **75**, 174 (2006).

[27] H. Lehle and M. Oettel, *Physical Review E* **75**, 011602 (2007).

[28] M. Brunner, C. Bechinger, W. Strepp, V. Lobaskin, and H. H. V. Grünberg, *Europhysics Letters* **58**, 926 (2002).

[29] K. Zahn, J. Méndez-Alcaraz, and G. Maret, *Physical Review Letters* **79**, 175 (1997).

[30] K. Zahn, G. Maret, C. Russ, and H. H. von Grünberg, *Physical Review Letters* **91**, 115502 (2003).

[31] K. Zahn and G. Maret, *Physical Review Letters* **85**, 3656 (2000).

[32] P. Poulin, H. Stark, T. C. Lubensky, and D. A. Weitz, *Science* **275**, 1770 (1997).

[33] P. Poulin, V. Cabuil, and D. A. Weitz, *Physical Review Letters* **79**, 4862 (1997).

[34] O. Moudain-Monval, J. C. Dedieu, T. Gulik-Krzywicki, and P. Poulin, *The European Physics Journal B* **12**, 167 (1999).

[35] M. Quesada-Pérez, A. Moncho-Jordá, F. Martínez-López, and R. Hidalgo-Álvarez, *Journal of Chemical Physics* **115**, 10897 (2001).

[36] R. Rajagopalan, *Langmuir* **8**, 2898 (1992).

[37] R. Rajagopalan and K. S. Rao, *Physical Review E* **55**, 4423 (1997).

[38] R. Henderson, *Physics Letters* **A49**, 197 (1974).

[39] P. G. Bolhuis, A. A. Louis, and J. P. Hansen, *Physical Review E* **64**, 021801 (2001).

[40] T. L. Hill, *Statistical Mechanics*, McGraw-Hill Book Company, New York, 1956.

[41] J.-P. Hansen and I. McDonald, *Theory of Simple Liquids*, Academic Press, London, 1986.

[42] D. A. McQuarrie, *Statistical Mechanics*, Harper & Row, New York, 1973.

[43] M. Allen and D. Tildesley, *Computer Simulations of Liquids*, Oxford University Press, Oxford, 1987.

[44] D. Chandler, *Introduction to Modern Statistical Mechanics*, Oxford University Press, Oxford, 1987.

[45] L. S. Ornstein and F. Zernike, *Proceedings of the Koninklijke Nederlandse Akademie van Wetenschappen* **17**, 793 (1914).

[46] K. F. Riley, M. P. Hobson, and S. J. Bence, *Mathematical Methods for Physics and Engineering*, Cambridge University Press, Cambridge, 2006.

[47] F. Lado, *Physics Letters A* **89**, 196 (1982).

[48] J. M. J. van Leeuwen, J. Groeneveld, and J. de Boer, *Physica* **25**, 792 (1959).

[49] J. L. Lebowitz and J. K. Percus, *Physical Review* **144**, 251 (1966).

[50] G. Zerah and J.-P. Hansen, *Journal of Chemical Physics* **84**, 2336 (1986).

[51] J. Baumgartl, J. Arauz-Lara, and C. Bechinger, *Soft Matter* **2**, 631 (2006).

[52] S. H. Behrens and D. G. Grier, *Physical Review E* **64**, 050401 (2001).

[53] F. J. Rogers and D. A. Young, *Physical Review A* **30**, 999 (1984).

[54] L. Reatto, D. Levesque, and J. J. Weis, *Physical Review A* **33**, 3451 (1986).

[55] K. Srinivasa Rao and R. Rajagopalan, *Physical Review E* **57**, 3227 (1998).

[56] B. Widom, *Statistical Mechanics: A concise introduction for chemists*, Cambridge University Press, Cambridge, 2002.

[57] N. Metropolis, A. W. Rosenbluth, M. N. Rosenbluth, A. H. Teller, and E. Teller, *Journal of Chemical Physics* **21**, 1087 (1953).

[58] D. Frenkel and B. Smit, *Understanding Molecular Simulation: From Algorithms to Applications*, Academic Press, London, 1996.

[59] D. Henderson and E. Grundke, *Journal Chemical Physics* **63**, 601 (1975).

[60] X. Guo and U. Riebel, *Journal of Chemical Physics* **125**, 144504 (2006).

[61] L. Verlet and J.-J. Weis, *Physical Review A* **5**, 939 (1972).

[62] A. Santos, M. L. de Haro, and S. B. Yuste, *Journal of Chemical Physics* **103**, 4622 (1995).

[63] F. Lado, *Journal of Computational Physics* **8**, 417 (1971).

[64] W. G. Hoover and J. C. Poirier, *Journal of Chemical Physics* **37**, 1041 (1962).

[65] E. Meeron and A. J. F. Siegert, *Journal of Chemical Physics* **48**, 3139 (1968).

[66] J. A. Barker and D. Henderson, *Journal of Chemical Physics* **47**, 4714 (1967).

[67] J. D. Weeks, D. Chandler, and H. C. Andersen, *Journal of Chemical Physics* **54**, 5237 (1971).

[68] M. Gillan, *Molecular Physics* **38**, 1781 (1979).

[69] H. Y. Ebril, *Surface and Colloid Chemistry*, chapter 2, pp. 5–70, CRC Press, New York, 1997.

[70] B. Derjaguin and L. Landau, *Acta Physico Chemica URSS* **14**, 633 (1941).

[71] E. J. W. Verwey and J. T. G. Overbeek, *Theory of the Stability of Lyophobic Colloids*, Elsevier, Amsterdam, 1948.

[72] F. Saija, S. Prestipino, and P. V. Giaquinta, *Journal of Chemical Physics* **113**, 2806 (2000).

[73] S. W. Koch, R. C. Desai, and F. F. Abraham, *Phys. Rev. A* **27**, 2152 (1983).

[74] G. M. Kepler and S. Fraden, *Physical Review Letters* **73**, 356 (1994).

[75] M. D. Carbajal-Tinoco, F. Castro-Román, and J. L. Arauz-Lara, *Physical Review E* **53**, 3745 (1996).

[76] J. C. Crocker and D. G. Grier, *Physical Review Letters* **73**, 352 (1994).

[77] J. C. Crocker and D. G. Grier, *Physical Review Letters* **77**, 1897 (1996).

[78] A. Moncho-Jorda, F. Martinez-Lopez, A. E. Gonzalez, and R. Hildago-Alvarez, *Langmuir* **18**, 9183 (2002).

[79] D. Frenkel, R. J. Vos, C. G. de Kruif, and a. Vrij, *Journal of Chemical Physics* **84**, 4625 (1986).

[80] C. Russ, K. Zahn, and H. H. V. Grünberg, *Journal of Physics: Condensed Matter* **15**, S3509 (2003).

[81] M. Brunner, J. Dobnikar, H. H. V. Grünberg, and C. Bechinger, *Physical Review Letters* **92**, 078301 (2003).

[82] J. Dobnikar, M. Brunner, H. H. V. Grünberg, and C. Bechinger, *Physical Review E* **69**, 031402 (2004).

[83] P. Bartlett, R. H. Ottewill, and P. N. Pusey, *Physical Review Letters* **68**, 3801 (1992).

[84] M. D. Eldridge, P. A. Madden, and D. Frenkel, *Nature* **365**, 35 (1993).

[85] E. V. Shevchenko, D. V. Talapin, N. A. Kotov, S. O'Brien, and C. B. Murray, *Nature* **439**, 55 (2006).

[86] A.-P. Hynninen, M. E. Leunissen, A. van Blaaderen, and M. Dijkstra, *Physical Review Letters* **96**, 018303 (2006).

[87] M. E. Leunissen, C. G. Christova, A.-P. Hynninen, C. P. Royall, A. I. Campbell, A. Imhof, M. Dijkstra, R. van Roij, and A. van Blaaderen, *Nature* **437**, 235 (2005).

[88] P. Bartlett and A. I. Campbell, *Physical Review Letters* **95**, 128302 (2005).

[89] C. N. Likos and C. L. Henley, *Philosophical Magazine B* **68**, 65 (1993).

[90] J. Fornleitner, F. Lo Verso, G. Kahl, and C. N. Likos, *Langmuir* **25**, 7836 (2009).

[91] L. Assoud, R. Messina, and H. Löwen, *Europhysics Letters* **80**, 48001 (2007).

[92] T. Stirner and Sun, *Langmuir* **21**, 6636 (2005).

[93] A. Chremos and C. N. Likos, *Journal of Physical Chemistry B* **113**, 12316 (2009).

[94] J. Fornleitner, G. Kahl, and C. N. Likos, *Physical Review E* **81**, 060401 (2010).

[95] T. S. Horozov, R. Aveyard, B. P. Binks, and J. H. Clint, *Langmuir* **21**, 7405 (2005).

[96] J. Sun and T. Stirner, *Langmuir* **17**, 3103 (2001).

[97] R. Aveyard, J. H. Clint, D. Nees, and V. N. Paunov, *Langmuir* **16**, 1969 (2000).

[98] D. Stamou, C. Duschl, and D. Johannsmann, *Physical Review E* **62**, 5263 (2000).

[99] P. A. Kralchevsky, N. D. Denkov, and K. D. Danov, *Langmuir* **17**, 7694 (2001).

[100] T. S. Horozov, R. Aveyard, J. H. Clint, and B. P. Binks, *Langmuir* **19**, 2822 (2003).

[101] N. Hoffmann, F. Ebert, C. N. Likos, H. Löwen, and G. Maret, *Physical Review Letters* **97**, 078301 (2006).

[102] W. H. Press, S. A. Teukolsky, W. T. Vetterling, and B. P. Flannery, *Numerical Recipes: The Art of Scientific Computing*, Cambridge University Press, Cambridge, 3rd edition, 2007.

[103] M. Parrinello and A. Rahman, *Physical Review Letters* **45**, 1196 (1980).

[104] K. W. Wojciechowskia, A. Brankab, and M. Parrinello, *Molecular Physics* **53**, 1541 (1984).

[105] F. Bresme, C. Vega, and J. L. F. Abascal, *Physical Review Letters* **85**, 3217 (2000).

[106] S. Mazoyer, F. Ebert, G. Maret, and P. Keim, *Europhysics Letters* **88**, 66004 (2009).

[107] U. Gasser, *Journal of Physics: Condensed Matter* **21**, 203101 (2009).

[108] D. J. Robinson and J. C. Earnshaw, *Langmuir* **9**, 1436 (1995).

[109] J. P. Hansen, *Physical Review A* **8**, 3096 (1973).

[110] H. Löwen, T. Palberg, and R. Simon, *Physical Review Letters* **70**, 1557 (1993).

[111] J. M. Kosterlitz and D. J. Thouless, *Journal of Physics C: Solid State Physics* **6**, 1181 (1973).

[112] D. R. Nelson and B. I. Halperin, *Physical Review B* **19**, 2457 (1979).

[113] A. P. Young, *Physical Review B* **19**, 1855 (1979).

[114] D. R. Nelson, *Defects and Geometry in Condensed Matter*, Cambridge University Press, Cambridge, 2002.

[115] N. Hoffmann, C. N. Likos, and H. Löwen, *Journal of Physics: Condensed Matter* **18**, 10193 (2006).